12-2020

Investigation Of Predicted Helicopter Rotorhub Drag and Wake Flow with Reduced Order Modeling

Tristan David Wall
University of Tennessee, Knoxville, twall4@vols.utk.edu

Recommended Citation

Wall, Tristan David, "Investigation Of Predicted Helicopter Rotorhub Drag and Wake Flow with Reduced Order Modeling. " Master's Thesis, University of Tennessee, 2020.
https://trace.tennessee.edu/utk_gradthes/6338

To the Graduate Council:

I am submitting herewith a thesis written by Tristan David Wall entitled "Investigation Of Predicted Helicopter Rotorhub Drag and Wake Flow with Reduced Order Modeling." I have examined the final electronic copy of this thesis for form and content and recommend that it be accepted in partial fulfillment of the requirements for the degree of Master of Science, with a major in Aerospace Engineering.

James G. Coder, Major Professor

We have read this thesis and recommend its acceptance:

Kivanc Ekici, Ryan S. Glasby

Accepted for the Council:
Dixie L. Thompson

Vice Provost and Dean of the Graduate School

(Original signatures are on file with official student records.)

Investigation of Predicted Helicopter Rotor Hub Drag and Wake Flow With Reduced Order Modeling

A Thesis Presented for the

Master of Science

Degree

The University of Tennessee, Knoxville

Tristan David Wall

December 2020

Acknowledgments

First and foremost, I would like to thank Dr. James Coder for affording me the opportunity to work on this project. Dr. Coder's knowledge of computational fluid dynamics and computer programming proved vital to the advancement of this work. I would also like to extended my gratitude to Dr. Glasby and Dr. Ekici for agreeing to serve on my thesis committee and for offering their critiques and insights.

I would especially like to thank my friends and fellow co-workers of the VolAIR lab, as without their knowledge and kind community this work would not have been possible. I would like to thank my family, and especially my wife for supporting me and pushing me to complete my Master's degree.

Additional thanks go to Rekesh Ali for providing one of the codes used heavily, and to Dr. Wong for his help in examining and optimizing that code.

In addition, I would like to thank Dr. Sven Schmitz, Mr. Warren Baker, and Mr. Charles Tierney from The Penn State University Applied Research Labs for providing the computational grids and experimental results used in this work.

Abstract

The rotor hub is one of the most important components of the modern helicopter. This complex collection of linkages and plates has numerous responsibilities, including the translation of pilot input to system response, anchoring the blades to the rotor mast, and sustaining the various forces transmitted by the blades. Due its intricate design and relatively small sized components the rotor hub interacts with the incoming flow to create a highly chaotic, turbulent wake which impinges on the fuselage and empennage. This assembly has also been found to be one of the primary contributors to the total vehicle parasite drag. Unfortunately studying the rotor hub and its wake more closely is made difficult by the limitation of both modern experimental and computational methods. From an experimental standpoint tests are expensive to run, difficult to gather large amounts of data from, and can require full or high scale Reynolds numbers. Computational Fluid Dynamics (CFD) predictions of hub flows are limited by high grid resolution requirements, and lengthy grid generation and simulation times. Modal decompositions provide robust options for reduced order modeling of fluid flows. Several modal decomposition methods are tested for the validity of their application to the complex flow fields that form around rotor hubs. Four variations of two rotor hub designs, a baseline and low drag, are simulated in forward flight. This selection of hubs was chose to examine the effects of both hub geometry and aerodynamic optimization on the rotor hub surface forces and wake. Flow solutions were found using the OVERFLOW2.2n overset, structured, RANS solver created and maintained by NASA. Simulations were conducted using a fully turbulent model and the grid generation and computational equations specifics are discussed in further detail. Each of the four hub variants was subjected to the same free stream conditions. Several variants of modal decomposition and other post processing techniques were used on the resultant surface force and wake data in order to characterize the hub flow field.

Table of Contents

List of Tables

List of Figures

Nomenclature

C_l = lift coefficient

c = chord length

e_0 = total energy

h_0 = total enthalpy

k = turbulent kinetic energy

N_b = number of blades

P = pressure

H = hub radius

r = radial location

Re = Reynolds number

Re_{hub} = Reynolds number based on hub diameter

Pr = Prandtl number

V_∞ = Free stream velocity

u = streamwise velocity

α = angle of attack

ω = Hub angular velocity

θ_o = rotor collective pitch

J = Advance ratio

λ = inflow ratio, Stokes' hypothesis

μ_t = eddy viscosity

ν_t = kinematic eddy viscosity

ρ = density

τ = shear stress

Ω = vorticity

ω = specific turbulence dissipation rate

Chapter 1: Introduction

The pursuit of a vehicle design capable of vertical lift off, landing, stable hover, and lateral motion is one of the longest and most storied in history. It has been tended to by some of the most progressive minds in science and saw the creation of some truly unique vehicle designs. Of these designs it is easy to say that the helicopter has reached the highest level of popularity and use over the last one hundred years of development. Serving in both civilian and military applications the helicopter is unique from of other vertical take off and landing (VTOL) capable aircraft. Other aircraft, such as autogyros and VTOL capable fighter jets, possess similar design qualities and capabilities to the conventional helicopter. However, these aircraft rely on either different types of power plant, such as jet engines, to supply their vertical flight abilities, possess design characteristics of traditional airplanes, or are not truly VTOL aircraft.

Helicopters can be generally defined as a type of aircraft which relies on the rotation of a collection of specialized wings to generate both the propulsive and control forces required for flight. The primary rotor, or rotors in the case of some helicopter designs, are rotated at high speed to generate the lifting force used by the aircraft. The pilot can then provide control inputs which tilt the entire collection of blades, collective pitch, or pitch the individual blades at different points in their rotation, cyclic pitch. These changes control the direction and speed of the aircraft's flight. Helicopters do not make use of wings or flaps in the same way traditional fixed wing aircraft do. While this consolidation of both propulsion and control forces to a single source does provide high maneuverability and VTOL capabilities it also leads to an increased level of mechanical complexity.

The rotation of the primary rotor collection causes a torquing force which must in some way be countered. Several solutions to this problem have been devised. A small rotor mounted perpendicularly to the empennage of the craft is the solution most commonly used on conjunction with single primary rotor, the widely successful example of this design is the Vought Sikorsky VS

300, shown in Fig.1.1a. Another solution to the issue of torque which has seen widespread usage is the implementation of two similarly sized counter rotating rotors mounted on the helicopter, with several variations of this system existing. These include the coaxial rotor, wherein the second rotor is mounted directly above the first rotor, tandem rotors, where two rotors of similarly size are mounted either side by side on outriggers of on the fore most and aft most section of the helicopter, and the inter-meshing rotor, where the two rotors are mounted separately right next to one another at slightly outward angles. Some of the earliest realizations of the tandem rotor and the coaxial rotor are shown in Fig. 1.1b and Fig. 1.1c respectively. While not the earliest implementations of these designs the VS 300, FL 282, and FA 223 were the first three true helicopter designs to prove successful enough to produce in any quantity of note [5]. Another, less popular solutions to the torque generation problem is the "no tail rotor" system or NOTAR. This system uses an internal fan expel air from slots on the tail, this air combines with the rotor wash to create a low pressure area on one side of the tail and a high pressure area on the other side, which counteracts the main rotor torque [6]. However, each of these carries an associated increase in mechanical complexity. The coaxial and inter meshing rotors requires a more complex mechanical system to facilitate opposing rotation and complicates the aerodynamics of the craft. The usage of a second rotor anywhere else on the craft, such as tail or tandem rotors, requires either a more complicated drive train or the use of a secondary power plant and control system.

The layout of the rotor blades is only one of many other issues inherent to helicopter design. Issue such as uneven lift distribution between the advancing and retreating sides of the rotor disk, the issue of lead lag, and blade flapping all requiring addition mechanical complexity. In tandem with the mechanical complexity, the aerodynamic complexity of rotor vehicles is considerably increased from the fixed wing aircraft. The rotation of the primary rotor Assembly create a highly vortical wake in its downwash, which the rest of the vehicle is constantly immersed in. The exact aerodynamics of the helicopter are still difficult to accurately define and predict even after decades of intense focus and research [7]. The requisite control forces to accurately maneuver such a vehicle are consequently quite high. While certain pieces of the rotor vehicle have the luxury of being designed primarily for their aerodynamic characteristics, one salient piece does not. Creating a control system articulate and robust enough to allow a pilot adequate control of the

(a) Vought-Sikorsky VS-300

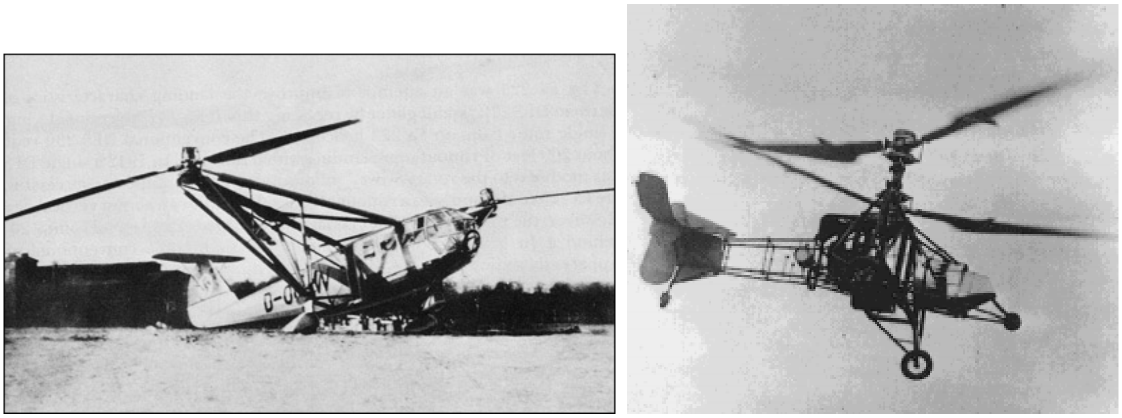

(b) Focke-Achgelis FA-223

(c) Dorand’s Gyroplane Laboratoire

Fig. 1.1 Early Rotor Collections

helicopter requires placing the primary design emphasis on structural strength and durability, not aerodynamics. It is with this mentality that the rotor hub was slowly developed.

Early rotor hubs addressed the various complexities of the helicopter using multiple hinged connections. One of the more popular designs used in the early and mid-20th century can be seen in Fig. 1.2. Used on the Sikorsky S-58 this full articulated hub used separate hinges to handle the lead-lag issue and the blade flapping problem, and bearings to allow for cyclic pitch control [5]. Contemporary configurations such as the "teetering" hub design would use few numbers of hinges and allow the inherent flexibility of the rotor blades to provide a solution for the blade flapping and lead/lag. Later designs would remove hinges in favor of hingeless designed, however each configuration carried a number of limitations with it. Some could only suppose a small number of blades, others could cause intensified ground resonance, and some were made more complex using multiple hinges, such the S-58. In the latter half of the 20th century further advancements such as the "Dynaflex", developed by Sikorsky [8], however the rotor hub remains a complex system into the modern era.

Even at its most elegant however the rotor hub is not designed for aerodynamic quality. Whether using hinges or a hingeless design the rotor hub in essence is nothing more than a collection of blunted bodies which is forced to interact with the surrounding flow environment through high speed rotational motion. This interaction creates a highly separated, complex flow that is characterized by small length scale structures and large generation of pressure drag [9]. This interaction, and the hub as a component, have been found to generate a large portion of the drag experienced by the vehicle in forward flight. This contribution is well documented, [9–13]. The reduction of this drag contribution stands to improve a number of vehicle qualities such as vehicle stability, control, fuel consumption, and component longevity. For single rotor helicopters this contribution has been found account for roughly 30% of the total drag in forward flight and is higher for compound rotor vehicles.

The problem of hub drag is difficult due to a number of factors. On one side of the issue the inherent complexities of the rotor system restrict the options for aerodynamic optimization. However, another outstanding problem is the understanding of the flow field that forms around the hub, or the lack thereof. As was noted by Reich et al. [9], a majority of the efforts on improving the hub drag phenomena have been done with a distinctly incomplete understanding of the nature

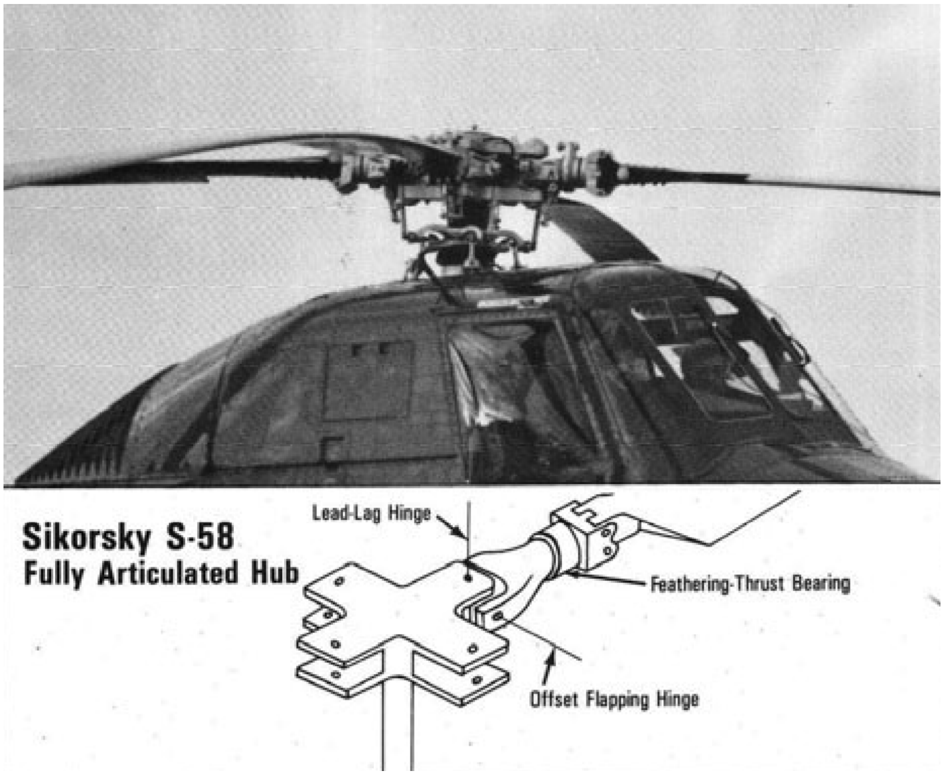

Fig. 1.2 Sikorsky S-58[5]

of these flow fields. While swept frontal area has been widely agree upon as the primary parameter which affects hub drag [13], the variety of hinges, linkages, and plates required by even relatively simple hubs can affect the flow formation in significant ways. Even the Aerospatiale StarFlex seen in Fig. 1.3, which was designed with mechanical simplicity and drag reduction in mind, were intricate enough to cause complex aerodynamic interactions.

Advances in both experimental techniques and computational technologies at over the late 20th and early 21st century now permit more detailed examinations of this issue. Even with these advances, the examination of the rotor hub flow field is not a trivial endeavor. Hub flows have been shown to be sensitive to a large number of factors such as pylon mounting, component Reynolds number, incoming flow conditions, and fairing presence. These dependencies and the cost associated with physical experimentation can make experimental data acquisition quite challenging. Computational Fluid Dynamics (CFD) traditionally provide a more cost effective and easy to manipulate means of obtaining predicted data, with Navier-Stokes equation based solvers such as OVERFLOW [14], FUN3D[15], or Ansys Fluent[16] in particular becoming increasingly popular in recent decades. Similar to experimental measurements however there are several factors that make modeling rotor hubs difficult even with modern advances in CFD. The separated nature of hub flow creates several difficulties from a computational standpoint as well. Flow separation is poorly predicted by RANS and as hub flows are dominated by rapidly changing small-scale structures they require high resolution grids and small time steps for the flow to be accurately predicted and captured. In addition, long time periods are needed if the aim of the work is to study any ergodic behaviors. These factors lead to high computational costs and prohibitively long run times. The resulting data sets can also be large, which adds computational cost to the post processing steps.

Despite these difficulties CFD predictions offers several advantages for analyzing rotor hub flow fields. The ability to quickly remove physical features from a computational model, to collect consistent data over long time horizons, and the ability to more easily change flow conditions make CFD an attractive tool for collecting large sets of rotor hub flow predictions. So the question becomes how can these large data sets be leveraged in furthering the current understanding of rotor hub flows.

Reduced Order Modeling (ROM) is set of mathematical tools that may hold the answer to this question. Fully resolving the rotor hub flow field entails recording the predictions for multiple variables over long time periods. Similar to the collection of large data sets in other fields of science, not all collected variables are required to gain insights in the underlying phenomena [17]. ROM techniques allow extraneous variables, or dimensions, to be removed from the set and a new model based on this reduced dataset to be constructed which still reflects important aspects of the original set. This obviously holds a solution to the first of the aforementioned questions, a model based on few variables is less computationally expensive. In regard to the second question ROM methods allow for the extraction of the affecting variables within the system and filter out variables that only serve as clutter. Such methods have been widely applied to not only aerospace engineering but a wide array of other fields.

One specific form of ROM, Proper Orthogonal Decomposition (POD) are of interest in its application to rotor hub flows. This method of model order reduction uses a collection of flow field solutions to form an eigenvalue problem, which is then solved to find the optimal set of bases functions to represent the flow fields with [18]. This method has seen application to other unsteady turbulent flows, but mostly in the context of airfoils or collections of airfoils. The possibilities of applying POD and derivative methods of model order reduction to rotor hub flows may offer insights into the driving mechanics of the hub flows and insights into how to construct accurate and computationally cheap models for hub flow.

1.1 Research Goals and Project Scope

The primary goal of this work is to explore the capabilities of modal decomposition based reduced order modeling in characterizing the complex flow fields around rotor hubs. While a large amount of effort has been dedicated rotor craft over the last half decade, little of that has been directed towards the rotor hub in specific. In an effort to further the current state of understanding this flow field, this study examines both the surface forces and wake formations of several rotor hub geometries. Several different post processing techniques including both POD and a variant of POD, spectral proper orthogonal decomposition (SPOD), are applied in an attempt to uncover any characteristic behavior in this flow. The primary objectives of this work are as follows,

1. Assess the installation effects via comparison of experimental data gather from the Garfield Thomas Water Tunnel (GTWT) to CFD predictions of rotor hubs in isolation and a computational recreation of a full water tunnel experimental setup
2. Quantify the effects of various components, such as the swashplate and rotor mast, as well as aerodynamic optimization on the predicted surface forces, load harmonics, and wake formations of rotor hub flows
3. Investigate the abilities of various forms of modal decomposition in identifying coherent behaviors within rotor hub flow

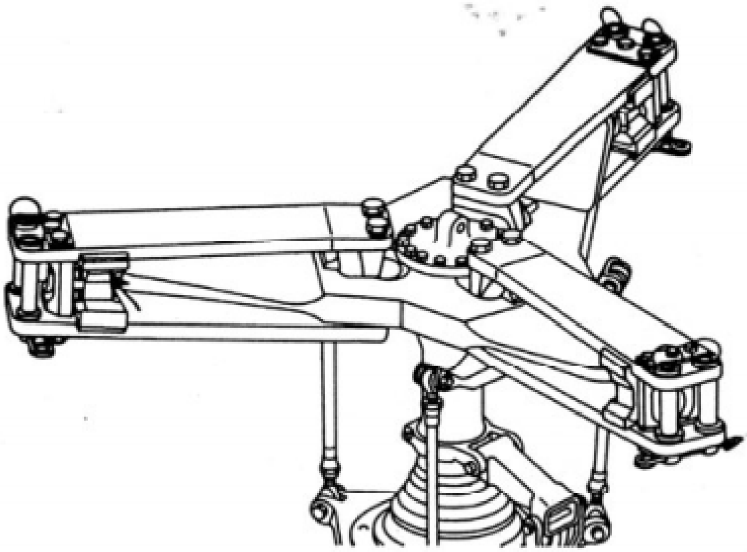

Fig. 1.3 StarFlex Rotor Head[5]

Chapter 2: Background

2.1 The Rotor Hub

2.1.1 Components and Configurations

As it is the center piece of this body of work some description and history on the rotor hub and its components will help give context to the issue at hand. The obvious characteristic trait of the modern helicopter are its distinctive blades. Unlike fixed wing aircraft where the propulsion and the control forces are separated, the rotor blades of a helicopter are responsible for both of these. The lifting and propulsive forces are generated by the rotation of the blades and the control forces by manipulating the azimuthal positions and pitches of the blades, both individually and as a collective. There are three axis a helicopter can move with respect to. Yaw refers to movement about the vertical axis, roll to movement about the horizontal axis, and pitch about the lateral axis [19]. Roll and pitch are tied changes in specific parameter of the rotor blades facilitated by the rotor hub. Lift and thrust are controlled by altering the pitch of all the rotor blades simultaneously, this is called the collective pitch control. Lateral motion of the aircraft is altered by pitching individual blades at specific azimuthal positions, and this is called the cyclic pitch [20].

The concentration of both controlling and propulsive forces into a single component leads to a large variation in mechanical stress and airspeed encountered by the rotor blades, and consequently the hub and the rest of the craft. Minimizing the effects of these variations was an important step in helicopter development, as they shortened component life spans and dramatically detracted from the vehicle's stability [7]. Over the past century the technological limitations of the times have yielded several hub designs to resolve these control and stability issues. Three broad categories of rotor hub currently exist; fully articulated, teetering, and rigid/hingeless [20]. The development and time periods of each of these are discussed further in the next section but a brief summary of their functionality is offered here.

While there are several configurations of the rotor hub the swashplate can be found in most modern rotor hubs assemblies in general. Swash plates have three primary pieces; a fixed plate, a rotating plate, and a form of pitch horns. The non-rotating portion is connected to the static potion of the rotor mast. This stationary piece is connected to the rotating portion via bearings, allowing it to rotate freely, which is attached to a rotating portion of the rotor mast. The pitch horns connect the rotating portion to the individual blades [21]. The swashplate is free to tilt about the rotor mast, the pitch linkages and horns translate this tilting to change in angle of attack in the blades. A figure of a swashplate, as a part of a helicopter control system can be seen in Fig. 2.1. While swashplates are the most common form of several other systems exist. Two notable systems are the Kaman Corporations servo-tab system and the Westland Helicopters' "Spider" system. The Kaman Corporation developed the use of servo-tabs on the trailing edge of the rotor blades which could be used to elastically twist the blades thereby changing their pitch [22]. The "Spider" system used by Westland Helicopters for pitch control removed the swash plate entirely replacing it with a single rotating ball joint attached to a control spindle. This spindle translated pilot input to changes in pitch through a system of arms which sat above the blade arms and connected to each of the blades.

Fully articulated rotor hubs were the first real solutions to the helicopter stability issue. These hubs made use of multiple hinges and bearings to allow the individual blades to lead/lag, flap up and down, and feather as was required of them [19, 20], an example of which can be seen in Fig. 2.2. While the exact number and location of hinges, and supplemental devices, like dampers, will vary between fully articulated hub designs there are generally three hinges/bearings which facilitate six degrees of freedom for the blade motions. While the fully articulated hubs provide excellent control authority over the rotor blades. However, the fully articulated hub suffer in several categories. The multitude of hinges and bearing increase the maintenance requirements and weight of the rotor hub Assembly, and can also increase the complexity of the aerodynamics of the flow field around as they induce channel flow [23].

The second type of hub, the so called "teetering hub" is only found on two bladed vehicles. The teetering hub is similar to the fully articulated hub in that it uses hinges to allow for rotor blade articulation however it does away with two both the flapping and lead/lag hinges seen in the fully

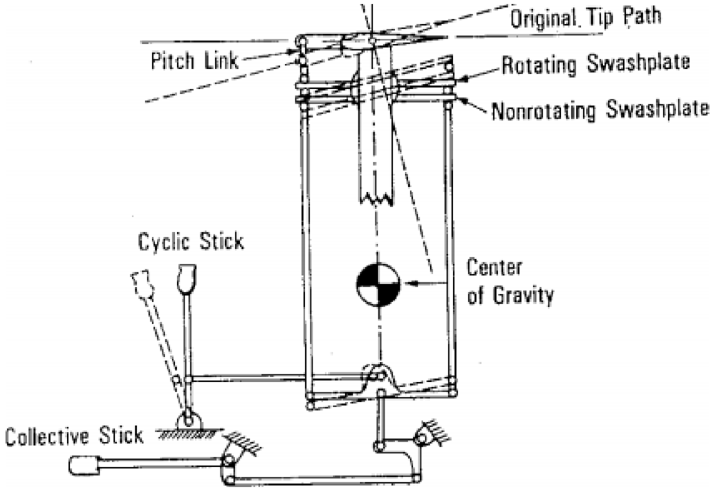

Fig. 2.1 Swash Plate Assembly[21]

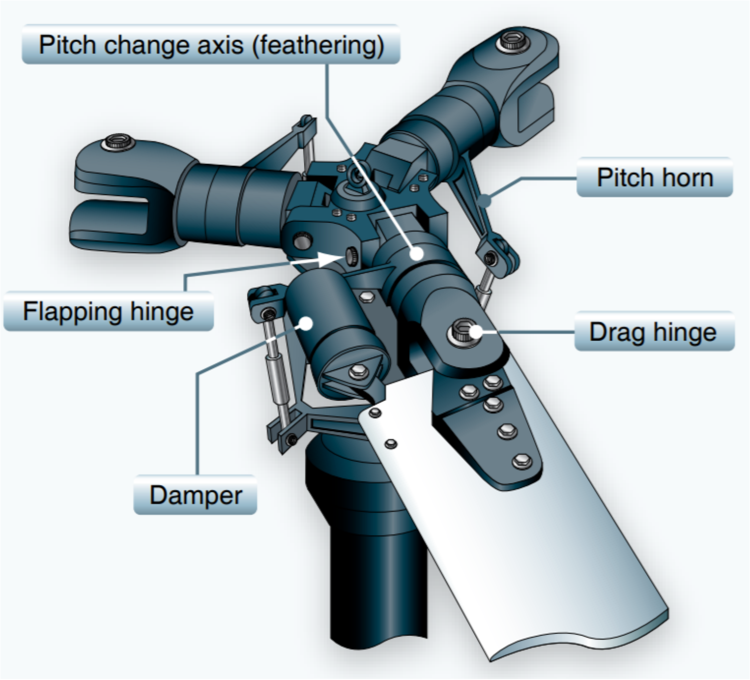

Fig. 2.2 Fully Articulated Hub [19]

articulated hub, instead replacing them with a single teetering hinge. The most popular of such designs was implements on the Bell 47 helicopter, which is shown in Fig. 2.3.

Several of the characteristics of a two bladed helicopter allow the simplification of fully articulated to the teetering hub. The lead/lag hinge in the fully articulated hub is to account for the acceleration of the individual blades cause by the blade flapping. As the blades flap up and down their center of gravity shifts inward and thus to preserve angular momentum the blades accelerate. In the teetering hubs because the blades are rigidly linked when one flaps up the other flaps down, thereby shifting the center of gravity of both blades simultaneously. This means that the accelerations of the two blades are perfectly synchronized and a lead/lag hinge is not necessary. The inverse flapping facilitated by the teetering hinge also address the lift dissymmetry that require the use of a flapping hinge is configurations with more blades [24]. The feathering bearing is still required for cyclic pitch control. Ultimately teetering hubs are simpler to maintain than full articulated hubs but can cause increased vibrations. In addition, teetering hub run the risk of mast bumping, where the hinge allows the blade arms and blades to tilt far enough to impact the rotor mast.

The third and final configuration of rotor hub is unique as it, in some senses, bookends the development of helicopters from inceptions to present. Early rotatory machines such as the Cornu helicopter or the Breguet quad-copter, both created in 1907, made use of completely rigid rotor hubs, with no hinges or bearings [26]. These rudimentary hubs were products of the technological and aerodynamically capabilities of the era, but more closely resemble modern hingeless hubs than fully articulated hubs. In its modern formation the name rigid is a bit of a misnomer, as the hub is not truly rigid but uses flexible structures to carry all the stress and forces normally addressed by hinges, and in some cases bearings. These hubs carry obvious benefits in mechanical simplicity and ease of maintenance [27]. In addition, hingeless/bearingless rotor systems include less drag than their fully articulated counterparts. The main draw-backs of such hubs are the increased vibrations they can experience and the increased structural demands of the materials used in the hub [22]. Depending on the design and materials selection used in the hub dampers may have to be used to prevent destructive ground resonance in the hub and fuselage and to reduce vibrations during operation. Two such hubs can be seen in Fig. 2.4, being developed by Sikorsky and Boeing respectively. In general, rigid hubs are constructed using a portion of material at the inboard sections of the rotor

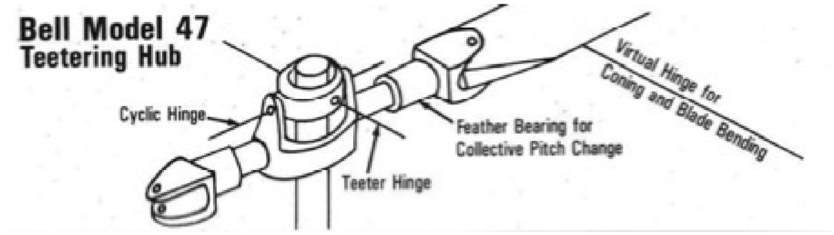

Fig. 2.3 Bell Model 47 Rotor Hub [24]

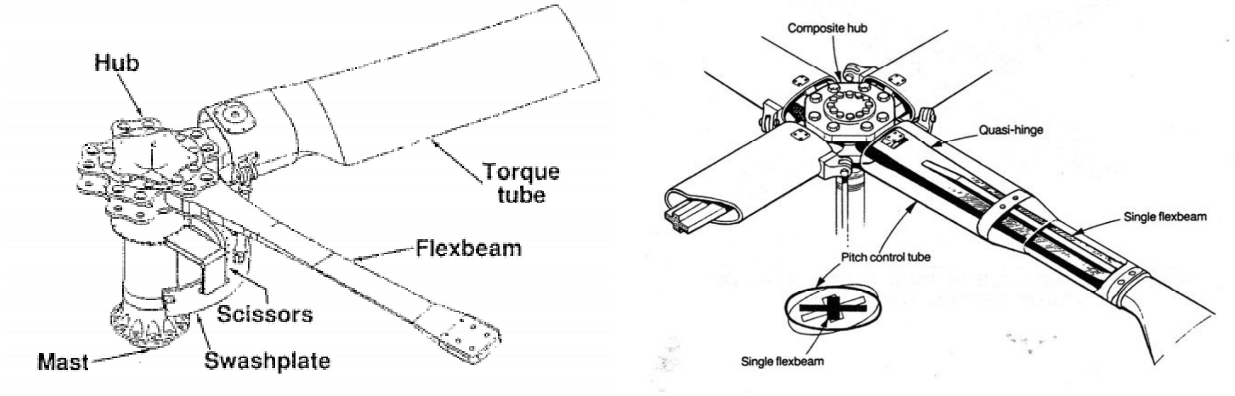

(a) RAH-66 Comanche Main Rotor System [25] **(b)** MBB/Boeing Vertol Bearingless Hub Design [24]

Fig. 2.4 Bearingless/Hingeless Rotor Hubs blades that are more flexible than the rest of the blade. The material of this section is used to account for the in-plane lead/lag and flapping motions of the blade. Torsional forces are applied to these areas to control the pitch of the blade. For instance the Boeing system show in Fig. 2.4a made use of filament-wound torque tub, which was rigidly attached to the flexible potion of the blade and attached via a pivot point to a traditional swash-plate setup [28]. It is notable that since the flexible element of the system must now account for both the lead/lag and the torsional flexion accounted for by hinges and bearings the cross-sectional form of the flexing element must be carefully chosen [28].

2.1.2 Early Development and History

While rotor vehicles as a concept have existed for centuries, in forms such as da Vinci's Aerial Screw, advancements in the creation of true, functional helicopters really began around the turn of the 20th century. Comprehensive narratives of this development can be found in Ref. [5, 7, 29, 30]. These however are broad examinations of the development of the helicopter in general, briefly touching on milestones in rotor hub. Presented here is a brief but more focused summation of the historical developments and advancements in rotor hub technologies, this section does draw heavily from the aforementioned sources as well as several others. With regards to rotor hubs the major advancements were the development of the fully articulated and teetering hubs, during the early 20th century, and the hingeless and bearingless rotor hub systems, in the later 20th century.

While it is generally agreed that first true helicopter flights took place in 1907 there are several notable advancements in the field of rotor technology that would later become common place in helicopters which occurred before this time. In 1859, a rotor system which was intended to control the ascent and descent of dirigible balloons was invented by Henry Bright. This system is notable as it is one of the earliest instances in which a multi-rotor system where counter rotating rotors were used as a means to counteract torque. Counter-rotating rotors would later become common place in helicopters like the Boeing CH-47 or the Bell-Boeing V-22 Osprey [31]. The most formative advancements of in the pre-flight era of helicopters actually came in the form of internal combustion engines. While the engines used in early and modern rotorcraft are beyond the scope of this work two are noteworthy, as the development of such engines was vital to the creation of practical rotor craft. The first, was designed by the French company Antoinette, and were used in creating the first true helicopters [30]. The second engine worth mention is the Manly-Balzer enginer. Shown in Fig. 2.5 this is a radial 5 cylinder engine it was initially designed by Stephen Balazar and then improved upon by Charles Manly. This engine is important as it held the highest lift to weight ratio for an internal combustion engine during the early 20th century, and power the first heavier than air flight of the quarter scale model of the Langley Aerodrome [32].

While the creation of engines with sufficient power to weight ratios to power helicopters was one of the major issues hindering the technology. Creating a control system with the adequate amount of authority to counteract the rotor torque reaction, the lift asymmetry in forward flight, and the vibratory loads on the rotors was another daunting task faced by the early helicopter community. One important advancement in helicopter control technology was made before the first true helicopter flights were made in Italy, in 1906. Gaetano Crocco, a renowned scientist and military office recognized that properly move and operate a helicopter would need some form of control to account for the lift asymmetry. in 1906 he patented one of the first systems of pitch control for rotor blades [33].

Similar to Crocco, Charles Renard worked on systems for increase control several years before the first successful helicopter flight. In 1904 Renard suggested the use of flapping blades to the rolling moment cause by the lift dissymmetry. While suggested in 1904 it was four years until an operational flapping system was patented and built by Louis Breguet in 1908 [34]. Crude in their early implementations both cyclic pitch control and flapping blades would come to be common in modern rotor hub systems. While the systems served their purpose the systems linkages and components that compromise modern cyclic pitch control and blade flapping are partially to blame for the high hub drag experienced in forward flight.

2.1.3 1920-1950

The two flights largely considered to be the first true helicopter flights both took place in 1907, in France. The first flight was carried out by Breguet and Richet's Gyroplane. The Gyroplane was a large cross shaped structure with rotor systems at the end of each arm and made use of counter rotation to account for torque. This craft made use of an Antoinette engine and completely rigid rotor hubs. The vehicle has absolutely no means of control or stability and had to be held physically held in place during hover. The second vehicle, designed by Paul Cornu, also used tandem, counter

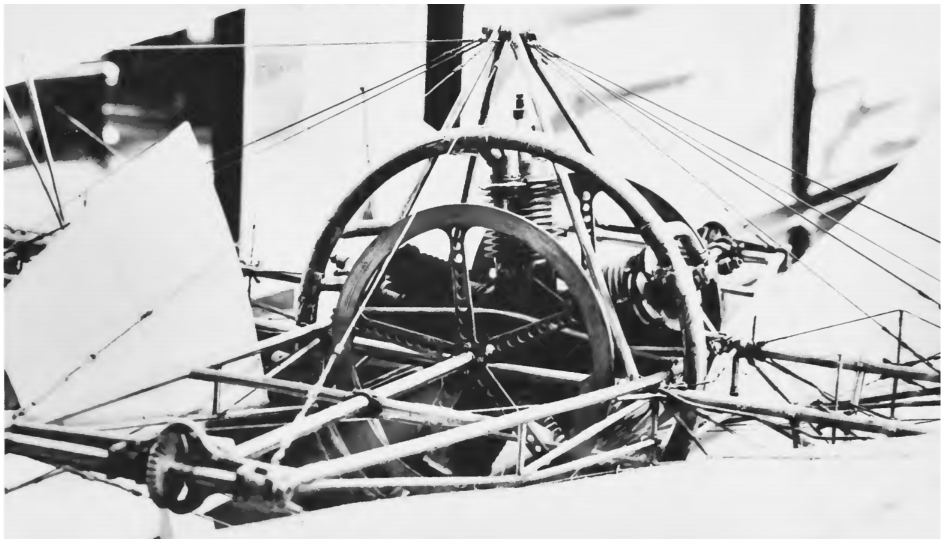

Fig. 2.5 Manly-Balzer engine mounted in Langley Aerodrome [32]

rotating rotor systems but only implemented two rotors each with two large paddle shaped blades. The most significant difference between the two is Cornu's attempt at vehicle control. Cornu's machine, shown in Fig. 2.6, featured an additional paddle below and slightly forward and behind the front and rear rotors. These were intended to allow the pilot to manipulate the downwash of the rotors but proved ineffective in exercising any form of aerodynamic authority. Both craft achieved only a few feet of vertical rise and lacked any means of recognizable control.

While others made attempts at VTOL vehicles before 1910, none were as successful as Breguet and Cornu. The most effecting in these attempts was made by Igor Sikorsky. Sikorsky attempted to create several co-axial helicopter prototypes, dubbed the S-1 and S-2. While neither of these successfully flew, they marked the first dabbling of Sikorsky who would later become one of the most formative minds in the development of helicopters.

The period between 1910 and 1920 is perhaps most important for yielding what would become the most conventional helicopter designs. Almost in parallel with Sikorsky's S-1 and S-2, Boris Yuriev began designs of a helicopter with a single main rotor and a tail rotor. Yuriev's vehicle was plagued by several problems characteristic of this time in helicopter design, being underpowered and suffering from mechanical issues such as vibration. However, similar to Crocco before, Yuriev recognized the need for delicate control in a feasible helicopter design. Yuriev's vehicle Incorporated a rudimentary for of cyclic pitch control, which was not very effective but novel in it application [7]. While the single rotor configuration would come to dominate helicopter designs of the future, it did not see much attention in that decade.

In 1914, a coaxial helicopter was design and flow by the Danish engineer Jacob C. Ellehammer. Similar to Yuriev's vehicle Ellehammer's used a rudimentary form of cyclic pitch control in an attempt to increase craft stability. Also similar to Yuriev's design however, Ellehammer was also partially successful. His craft was only able to hover for short periods of time in the air, and never made a completely controlled flight.

Coaxial vehicle designs received the most attention of any design between 1910 and 1920. After Ellehammer in 1914, an American designer by the name of Henry Berliner. Berliner's craft did not use any form of blade pitch control, instead opting for a similar method to Cornu, placing vanes in the downwash from the rotors to control the craft. Berliner iterated upon this design and in 1922 built a helicopter with counter-rotating tandem rotors. Berliner's second and later designs opted for

Fig. 2.6 Cornu Aircraft [30]

a chassis similar to the bi- and triplanes of the era. These later designs used similar control scheme the vehicle he built in 1922 used a set of multiple vanes in the wash of each rotor but added the ability to tilt the rotor shafts from more directional control [30].

The coaxial rotor system would see more developments in the hands of Raoúl Pescara during the early 1920s. Pescara's designs used large numbers of rotor sets, ranging between four and six sets of rotors over his different designs. Pescara attached the blades rigidly to the rotor hub and warping the blades to achieve pitch control of the blades. The most successful of Pescara's designs was the aircraft designated the No. 3, which he designed in 1923. This craft featured a more robust control system than other early helicopters. Cyclic pitch of the individual blades was control via the aforementioned warping technique, and the rotor hub was designed to be able to tilt giving the vehicle collective pitch as well. This craft was one of the first successful instances of the use of collective and pitch control being used to manipulate helicopters [35].

Interestingly the most significant piece of helicopter technology would be developed in the pursuit of a different form of vehicle. Autogyros are similar to helicopter in that they rely on rotating blades to generate lifting forces. However, autogyros do not power the rotation of their blades, instead using a propeller or other engine to provide propulsive energy. The rotor blades are allowed to freely move, and the forward motion produce a phenomenon called autorotation. Through autorotation the rotor blades then generate either all of the lift used by the vehicle or lift that is supplemented by other wings or lifting surfaces. The primary contribution of the autogyro to the development of helicopter is the full articulated rotor hub. Lead by Juan de la Cierva, the development of autogyros began in the 1920. Initial attempts by Cierva used co-axial counter-rotational rotors to counter act the lift dissymmetry issue. However, this proved ineffective, so Cierva switch to single main rotor systems, hence their inclusion in this section.

The major technological steps of Cierva's work are the inclusion of the flapping and lead/lag hinges in his autogyro's rotor hubs. As was previously mentioned some thought and work had been given to flapping in the early 1900s by Renard and Breguet, but Cierva create the most successful early implementations in his C line of autogyros, with the C-4, shown in Fig. 2.7 being the first to use them. The lead/lag hinge would be included on the C-7 autogyro, after a dramatic failure wherein one of the rotors on the C-6 model broke off during a landing. Cievra also implemented dampers on the lead/lag hinges to assuage ground resonance issues [30]. These additions would

Fig. 2.7 Cierva C-4 Autogyro[36]

complete one of the earliest and most successful fully articulated rotor hubs and form the basis for future develop of the notion. Cierva's work also influenced Raoul Hafner who began to being work on autogyros as well. It was during this work Hafner would develop a slightly more advanced system of control cyclic and collective pitch. Hafner's spider system, shown in Fig. 2.8, was a marked improvement as it allowed collective pitch to be controlled without tilting the entire rotor mast, as Cierva's did. The autogyro enjoyed intense amounts of attention during the early half of the 20th century but was ultimately discarded with the rise of more successful helicopter designs in the 1940s and 1950s.

While this system would come to be the most common rotor configuration in the later portions of the 20th century for several reasons, it did not see much attention or progression during the 1910-1920 time period. Several single rotor vehicles were created during this time, such as the Berliner in America and Brennan in Britain. Brennan's design is notable in that it is one of the first recorded examples of the use of servo-flaps, mounted inboard of the blades. The single rotor system would see some further development by A.G. Baumhauer and Raoul Hafner in the late 1920s and early 1930s. Hafner's aircraft, dubbed the R-2, and Baumhauer's aircraft are notable as they some of the earliest record implementations of swashplates as a means of collective pitch control. Baumhauer's craft is also notable as its blades were not rigidly attached to the hub, but allowed to rotate about a spanwise hinge, i.e. a lead/lag hinge. Baumhauer's pitch control system can be seen in Fig. 2.9 and an excellent description of it is given by Vodegel et al. in Ref. [38].

Almost a third of century's worth of development in helicopter design would culminate into several revolutionary helicopter designs in the late 1930s and early 1940s. In single rotor craft designs two vehicles from this era stand out. The VS-300, designed by Igor Sikorsky, was first developed in 1938 and was improved on until 1942. Sporting a single main rotor and accompanying tail rotor the VS-300 was not significant for any large technological advancements. The initial VS-300 designs used two smaller tail rotors mounted horizontally to affect translations but later version replaced these with a fully articulated rotor hub. The VS-300 is more important in that it won Sikorsky a contract with the army. This contract led to the creation of the R4 and R-5 helicopters which were one of the first widely produced helicopters to be adopted by the US military, seeing limited service in the second World War [35]. This line of helicopters is often credited with birthing the rotor vehicle industry.

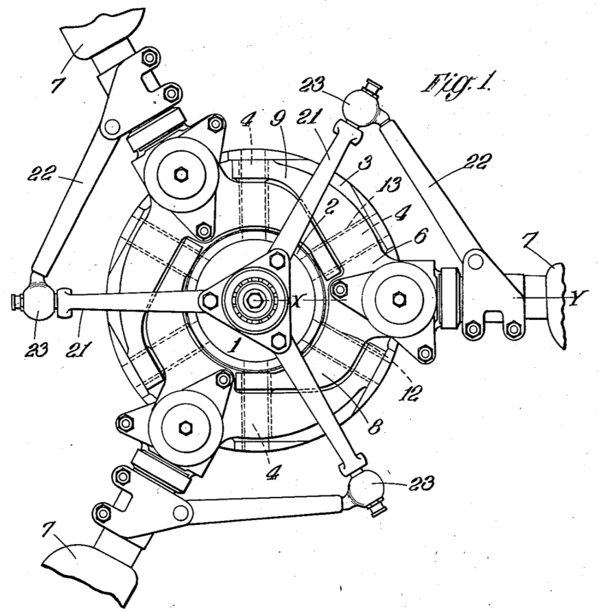

Fig. 2.8 Hafner Spider System [37]

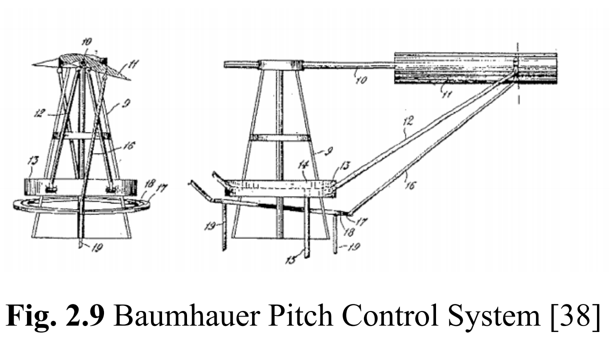

Fig. 2.9 Baumhauer Pitch Control System [38]

The second single rotor design of note was created by Arthur Young between 1940 and 1943, working with the Bell Aircraft Company for the later portions of the development. Young had created a novel teetering hub [39] design. The teetering hub was designed to be used on single rotor two blade craft. The two blades were rigidly linked and attached to the hub using a single seesaw style hinge. This design eliminated the need of conventional flapping and lead/lag hinges. Young's design also used a stabilizer bar, which rotated with the blades. The gyroscopic forces generated by this bar stabilize the rotor blades. This work would ultimately lead to the creation of the Bell Model 47, one of the most produced helicopters in history, which also was the first helicopter to receive the first certification for civil uses.

A similar idea to Young's stability bar would be created by Stanley Hiller in the form of the ”rotormatic” control system. First implemented on the Hiller model 360, also known as the UH-12. Unlike Young's system, which relied on gyroscopic force, this system featured two “paddles” or short wings, placed at the ends of a bar at a right angle to the main rotor blades. The bar was connected to the main rotor by a system of linkages. This allowed the pilot to control the cyclic pitch of the rotor blades by making changes to the pitch of the paddles. This system dramatically reduced the input forces required, making the vehicle easier to control. Unfortunately, it also increased the lag between pilot input and system response. More detailed description and evaluations of both the Young and Hiller systems can be found in Ref. [40]. The single rotor was not the only helicopter configuration to see the first instances of genuine success, or larger production scales however. Two other helicopters would see production in relatively large quantities for the era, and featured unique hub layout. Through the late 1930s and early 1940s, in Germany, Antione Flettner developed a series of unique helicopter dubbed “Synchrocopters”. These helicopters used two sets of rotor blades which were mounted on two separate hubs. The hubs were placed very close to one another and tilted slightly outward, so the blades intermeshed during flight. This craft was official adopted by the German military in 1942, being ordered in bulk but few survived the events of World War 2. Intermeshing rotor designs saw far less mainstream success after the war, in part due to the added complexity of the synchronizing system required by the blades.

The second craft of note also saw its inception in Germany during that later portion of the 1930s designs by Heinrich Focke. Focke drew inspiration from the earlier works of Cierva and the biplane designs of the era. Focke series of aircraft used tandem rotors mounted to the fuselage of

Fig. 2.10 Sikorsky R4 [5]

Fig. 2.11 Bell Model 47 [30]

a bi-plane via steel out-rigging structures. The first of Focke's vehicles, the Fw 61, made its first flight in 1936. The rotor blades were attached to the rotor head using both flapping and lead/lag hinges. Cyclic pitch control was attained by means of a swashplate assembly, collective pitch of the blades was controlled by raising and lower the swashplate vertically along the rotor mast. Focke's rotor hub assembly was unique in that it also featured a novel centrifugal controller which would automatically separate the rotor hub, and thus the blades, from the rotor shaft if the rotor speed decrease past a certain point. This allowed the vehicle to attain autorotation in the case of engine failure, which Focke considered a necessity for vehicle safety [41]. Focke would continue his work and later create the Fa-223, which utilized the Fw61 as a base and made dramatic improvements to lifting capability.

In examining the first half of the 20th century it is somewhat apparent that large portions of the efforts of early helicopter pioneers were devoted to solving the problems of power generation and control/stability. With the Sikorsky R-4 and R-5 being produced and utilized by the US military, the Flettner and Focke vehicles seeing similar treatment in Germany, and the Bell Model 47 receiving its certificate for civil application in 1947 their efforts arguably were successful. Fifty years of effort and development had crafted the helicopter into a relatively safe and operational vehicle.

2.1.4 Post-1950s

The second World War served as a large catalyst in the development of helicopters, in some senses that interest shown by different national militaries of the time jump started the helicopter industry. During the 1950-60s the number of both the number of companies focused on helicopter, and the number of helicopters being produced saw a meteoric increase. This period saw the adoption of the conventions and technologies developed by the early 20th century pioneers, such as Cierva, Hafner, and Yuriev, as common place. Fully articulated and semi-rigid hubs dominated the landscape and the various hinges and dampers that had been novel application less that twenty years before now adopted as conventional control methodologies.

Outside the field of rotor hub technologies and control mechanism the late 1940s and early 1950s produced some very unique experiments and developments. The most practical and long lived technology to come from this era was the turboshaft gas turbine engine. Derived from the advancements in jet propulsion over the 1940s, gas turbine engines were capable of producing

Fig. 2.12 Flettner FL-282 [5]

Fig. 2.13 Focke-Wulf Fw61 [41]

significantly more power than the piston engines of the time. Technically developed in the mid- to late 1940s by the 1950s turboshaft engines would see wide adoption in the helicopter industry. As powerplants are beyond the scope of this work so no further detail will be devoted to them.

Another interesting area of research in helicopter development, more closely related to craft control was the investigation of various forms of blade propulsion. For example, the Hughes XH-17 created in 1952 expelled a mixture of compressed air and fuel from the blade tips, where it was burned to propel the rotor blades. A good description as well as the results studies on the vibrational and flutter characteristics of a scaled model of the vehicle are given in Ref. [42]. The XH-17 is notable as it made use of laminated blade-retention straps to anchor the blades to the rotor head. The use of such straps in places of flapping hinges was one of the early examples technology which would later create the rigid rotor hub. While the concept of fluid expulsion from the rotor blades to drive or aid in blade propulsion would see some further attention, examples being the Hughes XV-9 which used ’hot-cycle’ propulsion and the Sud-Aviation S.O. 1221 Djinn which used a compressed air sans combustion to drive the blades, the concept would ultimately be abandoned by the mainstream helicopter design community. The primary issue found with these concepts being very high fuel consumption, complexity, and reliability.

The 1950s are mostly important as they signified the wide scale maturation of the helicopter as a fringe military technology into a mass-produced common place technology. Several helicopter designs which would spawn long lines of different helicopters were created during the 1950s. Piasecki for example, headed the design of the PV-3 Dogship in 1945, then in 1952 he iterated on it to create the H-16 and H-21 helicopters. These were the first widely successful tandem rotor craft featuring the fore and aft rotor configuration, as opposed the side-by-side designs favored by others. This configuration lead to the development of the Chinook CH-47 and was the calling card of The Piasecki Helicopter Corporation, even as it changed into the Vertol Company and eventually to a division of The Boeing Company.

However, it is arguable that the most important development of the helicopter industry during the 1950s, and most pertinent to this work, was the “rigid” rotor hub. The term rigid is a bit of a misnomer, with the hub configurations also being called hingeless and later bearingless, as they are not strictly rigid. The philosophy behind these hubs is quite simple. They use the elastic deformations of specially designed portions of the hub, or inward portions of the blades to accommodate blade motion that traditionally required hinges or bearings. Bell Textron lead this effort in 1957 when the implemented the “flexbeam”, a hingeless rotor hub that saw two and three bladed configurations. Less than a year later, Lockheed Martin’s first attempts at a rigid rotor system would see its first flight on the CL-457 [43]. While technically not a novel notion, Cierva had made attempts at rigidly rotor heads in the earlier half of the 20th century, these were the first instances that could be considered successful. Rigid hubs were of interest for several reasons. The removal of the robust hinges and bearing in the full articulated hubs meant a cleaner, slimmer hub profile. These hubs also offer faster responses to pilot inputs, and better natural damping characteristics than full articulated hubs [44].

Both the Bell Model 47 and the Lockheed Martin CL-457 saw further testing and development over the early 1960s. Each craft saw variations in number of blades and blade materials, Bell also tested their hingeless hub on several other fuselages over the decade. In general, they confirmed that in addition to the improvements on control, rigid hubs also offered better stability and a wide range of configurations for center of gravity. However, early integration of both vehicles experienced severe levels of vibrations and Bell found that the hingeless rotors produced higher rotor mast stresses [45].

Bell Textron and Lockheed Martin led the development of rigid rotors in the 1960s another company, Messerschmitt-Bolkow-Blohm (MBB) had begun to develop their own contribution to the rigid hub helicopter development. The MBB BO-105 made its first flight in 1967, and was immediately impressive for several reasons. It was first helicopter to feature twin-engines and a revolutionary Bolkow rigid rotor system. Technically speaking Bolkow, a German aviation company had begun development of the rigid rotor system used by the BO-105 in 1962 before being merged with Messerschmitt in 1968 The BO-105 used a titanium rotor hub and stripes of titanium lamination for construction and featured full cyclic and collective pitch controls via a traditional swashplate mechanism, seen in Fig. 2.15. A full description of this rotor, and the MBB BO-105 helicopter can be found in Ref. [46]. The B0-105 saw extensive usage by various military and civilian bodies after being placed in full production in 1967.

The early success of Bell, Lockheed Martin, and MBB served to reinforce the benefits of hingeless rotor hubs as a concept. While companies would continue work in the development of hingeless rotor systems, In the late 1960s several companies also began work on bearingless

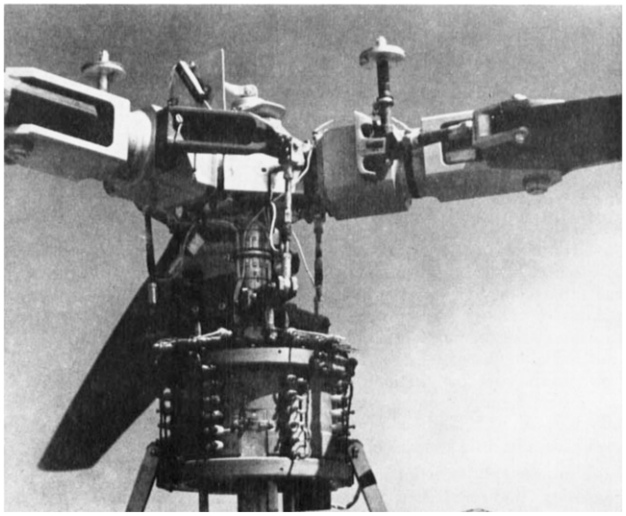

Fig. 2.14 Bell Hingeless Rotor Head [44]

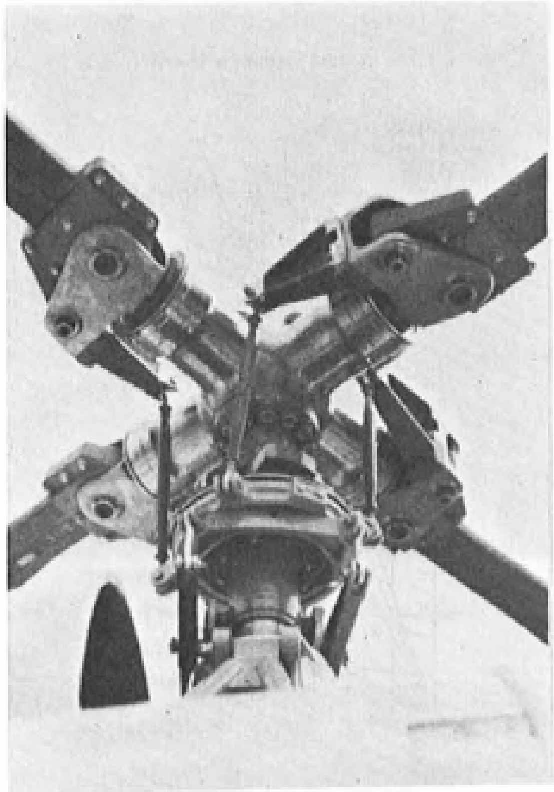

Fig. 2.15 MBB BO-105 Rotor Head [5]

main rotor system (BMR) designs as well. The hingeless hubs designed before the late 1960s still relied on bearings to facilitate the feathering motions of the blade, using the elastic deformations to replace on the feathering and lead/lag hinges. Huber [25], gives a detailed summary of the forty plus years of development invested in bearingless rotors.

Similar to the development of the hingeless hub, Lockheed Martin lead one of the earliest efforts to develop a bearingless hub. In 1966, Lockheed Martin flew a XH-51A helicopter with a bearingless hub. This hub made use of steel flexures with low in plane stiffness to allow the required levels of torsional movements. Lockheed flight tested this for several years but saw extremely high levels of both air and ground resonance developing at different rotor speed condition, ultimately concluding that the XH-51A iterations of the bearingless rotor was safe to continue flight testing [47]. Lockheed's efforts, while ultimately unsuccessful in their early iterations far preceded any efforts from other developers on bearingless. Other companies began working on their bearingless rotor hubs in the early 1970s.

Aerospatiale, a French company, began developing and testing several bearingless rotor hub systems. During the early 1970s they devoted a significant amount of attention to the ”Triflex” rotor head. This system was similar to the Lockheed Martin but used fiberglass-epoxy and elastomeric composites in place of steel. While the results of initial flight tests were positive, the Triflex would ultimately be used as a basis for the development of their later Starflex and Spheriflex bearingless rotor hubs, which were developed over the next several decades. Documentation of these hubs and results from several flight tests can be found in Ref. [48–50].

Both Bell and MBB would begin development of their own bearing after Aerospatiale. Bell began designing and testing multiple different hingeless and bearingless rotor hubs built from composite materials across the 1970s. Bell began the Model 680 program in latter half of the 1970s. Bell had several specific goals in mind for this hub, being a fifty percent reduction in number of parts, a fifteen percent reduction in hub weight, improved life cycle cost, and reduced vibration levels. The original model 680 rotor hub system was a four bladed system that featured specially designed yokes. Created from S-glass, a stiffer variant of fiber glass, the yoke extended approximately 20% of the radius out from the hub. It was then joined to the blades via a stiff cuff Assembly. The yoke was responsible for accommodating the pitching, flapping, and lead/lag movements of the blade, as well as the blade centrifugal and lifting forces. The cuff assemblies then transmitted the torsional movements from the yoke to the blades.

The Sikorsky Dynaflex system represents one of the most recent and high-profile attempts at designing a bearingless rotor hubs. starting development in the early 1980s. This system connects a bearingless rotor to the rotor mast via a gimbal joint composed of an elastomeric spherical bearing and flexible elastic restraints [8]. This system offered several benefits over other bearingless systems in that it was far more flexible. The gimbal also served to act as universal, constant speed joint which produced reduced Coriolis effects from a fully articulated hub [51]. In the modern day the fully articulated, teetering, and bearingless/hingeless hubs all see widespread use in both civilian and military applications. The prominence of craft designed during the later portion of the 20th century that are still use ensures that each of hubs has remained relevant.

2.2 Rotor Hub Aerodynamics

2.2.1 Investigations and Experimental Efforts

During the late 19th and early 20th century fledgling rotor vehicle developments were marked by a fundamental lack of understanding of rotor aerodynamics. This culminated in many designs being overpower, overweight, and aerodynamically inefficient [7]. Early efforts at understanding rotor vehicle aerodynamics were mostly focused on the blades, as generating adequate lift was a large issue for the early designers. Some of the earliest efforts were made by Theodore von Karman in the 1910s and 1920s. Karman conducted experimental tests on several early helicopters and large propellers, the results of which were published by the National Advisory Committee for Aeronautics (NACA) [52].

It was not until the 1950s that early rotor craft community turned its attentions to the characterization and reduction of hub drag. Harrington, and with the later assistance of Churchill, investigate the effects of parasite drag in 1954 [53]. Largely informed by prior work on drag reduction in fixed wing aircraft Harrington cited a plethora of contributors to the helicopter parasite drag. These included the landing gear, rotor hub, and gaps/joints in the fuselage. This first investigation gave only a cursory amount of attention to the rotor hub, indicating that the contributions of the rotor hub to the parasite drag could be reduced through the use of a fairing. At the time, the contributions and characteristics of the rotor hub flow to drag were still unknown and the use of fairings in fixed wing aircraft and this studies attention to them would go on to inform the direction of hub drag reduction for the next 50 years. A year later, Jones et al. [54] conducted several wind tunnel tests on the Sikorsky H-5 three bladed fully articulated rotor hub. They found that adding faired cuff style fairings to the blade shanks and hub, hub drag could be reduced by 12%.

In 1959, Churchill and Harrington [55] would return to the issue of parasite drag but focused exclusively on the rotor hub's contributions. Five different full-scale hub geometries were tested both with control systems and in isolation, over a range of angles of attack and at air speeds of 135-165 mph. Churchill and Harrington found that forward flight speed, hub rotational speed, and hub angle of attack all had minimal effects on the hub parasite drag. However, it was shown that increased frontal area caused increased drag coefficient across the five models.

In 1961 Moser conducted another study of helicopter drag [56]. Moser tested full-scale helicopter fuselages with four different pylon configurations and five different representative hubs. This was one of the earliest studies to vary hub lengths from the fuselages. The study made note that alterations in hub separation seemed to alter percentage of total drag accounted from by separation drag, and that hub-pylon clearance was a matter that required merited further investigation in the future.

Building on these works, Sweet et al. [57] conducted a series of wind tunnel tests on a collection of fuselage, rotor hub, and mounting pylon configurations. They suggested that improving the aerodynamic quality of the fuselage and landing skids would greatly reduce drag experienced in forward flight. They found that the rotor hub and its mounting pylon accounted for 20-30% of the drag of the experimental configurations. They also made note that their faired hubs did not perform significantly better than the unfaired hubs. Ultimately Sweet et al. concluded that any major reductions hub drag reduction could be achieved only by reducing the hubs frontal area.

The 1970s, particularly in their later half, saw a dramatic increase in the focus on rotor craft drag characteristics. Reflective of the previous decades of studies these works placed a large emphasis on investigations of fairings and hub/pylon separation. Montana [58] tested three different fairings on a model rotor hub. This study found that the effectiveness of certain fairings was tied to the effective angle of attack, the elliptical fairing proving more effective at angles of attack lower than $\alpha = -6^o$ and the reflex curvature more effective at angles of attack greater than $\alpha = -6^o$. In addition, the study found that rotor hub data could be approximated with a stopped rotor hub provided that the hub advanced ratio was greater than 10.0 or the rotor advanced ratio was greater than 0.5. Logan also noted that the lifting and pitching moments were entirely dominated by the aerodynamics of the blade shanks.

In 1976 and 1977, Sheehy et al. authored two reviews of hub drag data [13, 59]. The findings of these works were that rotor hub/fuselage separation distance is an important factor in drag reduction but must be carefully balanced so as not to negate the reduction in interference drag with the addition of excess surface area. In addition, Sheehy et al. found that as Mach number increased, hub fairings became less effective in drag reductions. In the following year a similar review would be conducted by Keys and Rosenstein, [60]. This study further confirmed that hub/pylon separation played a dramatic role in reducing interference drag. Both Sheehy et al. and Keys and Rosenstein suggested further investigations on the effects of Reynolds number as that was not well documented at the time.

During the early 1980s two experiments examined the effects of Reynolds number on hub drag measurements. Logan et al. [61], conducted an extensive series of experiments in effort to characterize the effect of scaling on differently sized experimental test models. Among their many findings were that a critical Reynolds number of 3×10^5 had to be achieved for accurate hub, pylon, and fuselage drag testing. This study also highlighted the necessity of using sealed hub fairing to maximize drag reductions. Later, in 1985, Felker [62] showed a Reynolds number effect on the drag coefficients for faired hubs between 1×10^6 and 3×10^6.

It was also during this time period that visualization techniques and technologies matured to the point where they could be effective implemented in the study of rotor hub wake shedding. Roesch et al. [63], performed one of the earliest studies of rotor hub wake in 1985. Their work outline several of the major problems cause by the rotor hub wake, including decreased pitch and yaw control due to the wake interaction with the tail rotor and vibrations caused by the hub wake impacting the tail surfaces. Visualization experiments of the hub wake were conducted using a sequence of increasingly detailed hub model mounted on a Aerospatiale SA-365 fuselage. The hub models began as a simple cylinder to model the rotor shaft, with pitch links and blade shanks sequentially added. it was assumed that rotor blades only served to affect the positions of the hub wake relative to the tail and not the wake structure.

Roesch et al.'s primary findings were the presence of a large stationary vortex directly behind the rotor shaft. This vortex would periodically shed large eddy structures which were convected downstream. Increased hub fuselage separation served to weaken and de-regularize the eddy shedding. Spectral analysis of the wake also revealed a mixture of turbulent energy characterized by a continuous spectral distribution and discrete energy concentrated as the rotor harmonics. It was also found that if exposed, the scissor arm components of rotor hubs have a noticeable effect on the flow harmonics. When exposed the scissor arms generated a strong 1Ω discrete energy, with Ω denoting the blade passage frequency. In addition it was theorized that the interaction between the scissors and the fuselage cowling generated 1Ω discrete energy further away from the rotor axis. The perturbations generated by the scissor was also found to be not purely sinusoidal, which generated a strong 2Ω energy content in the same spatial area as the 1Ω content.

In the later 1980s NASA launched the Hub Drag Reduction program, which would produce several landmark studies over the next decade. This program focused on the effects of implementing fairings around the rotor head, and later the rotor mast or pylon. In 1987, Young et al. [64] conducted experiments to examine then new hub/fairing configurations, some of which included strakes for passive flow control. The study examined three configurations, single-rotor hub and shaft fairings, single-rotor strakes, and coaxial-rotor hub and shaft fairings. The inclusion of co-axial hubs in this study is somewhat notable as co-axial rotor hub configurations had fallen out of favor at this point in history. Each of the previous configurations was tested with various shaped hub fairings and pylon fairings. The hubs were tested without rotation, as earlier works [61, 62] showed small difference in fairing drag based on rotational speed. It was found that the strakes proved largely ineffective in helping to reduce drag. It was also found that the use of fairings with flat plates for bottoms stood to substantially reduce coaxial hub drag.

This study was followed in 1989 by several more studies by NASA on helicopter hub drag [65, 66]. Both studies made use of a 1/5 scale Sikorsky XH-59A fuselage to mount a series of hub and pylon configurations upon but used different wind tunnels. Graham et al. [65] performed a series of tests to examine the interactional aerodynamics between the hub and pylon and the effects of various fairings. They found that the interactional aerodynamics between the hub fairings and the pylon caused a substantial amount of interference drag. Confirming the findings from the earlier studies it was again seen that fairings with flat lower surfaces reduced the drag the most, and smaller hub-pylon separation distances resulted in lower interference drag. They suggested that pylon fairings, aft fuselage, hub separation, and hub fairings should all be considered in design to maximize drag reductions. Sung et al. [66], recognized the issue of interference drag between the hub fairings and pylon. Similar to the previous work, Sung et al. found that hub fairings with a flat lower surface tended to result in lower interference drag. It was concluded that fairing with flat lower surfaces and circular-arc upper surface created the most favorable interactional aerodynamics with the pylon and thus resulted in largest hub drag reduction.

The early 1990s saw further interest in the abilities of fairings and interactional aerodynamics in decreasing the rotor hub's contribution to drag. The NASA hub drag reduction program continues in the early 1990s with the work of Martin et al. in 1991 [67] and 1993 [68]. These studies switch from the Sikorsky XH-59 used in the previous NASA studies to a 1/5 scale Bell Model 222 fuselage with a rotor head modeled after the bearingless Bell model 680. The model was tested without model blades, but with model blade shanks as these were found to carry significant drag penalties [65]. The study conducted in 1993 used three different pylon fairings. The first was a thicker non-tapered pylon which was based on the NACA 0034 airfoil cross section and offered increased room for control systems such as the swashplate and pitch links. The remaining two pylons were tapered, with one tapering from fuselage to rotor head based on the NACA 63 series airfoils, and the other tapering from rotor head to fuselage which used the NACA 0034 airfoil correction with varied chord. Fairings were designed based on the previous NASA studies, using the flat bottomed, circular-arc topped design found to be previously effective. The fairings also sported rounded leading edges, and expanded cut-outs to allow for blade flapping. The study also examined novel 'dual component' configurations, which featured non-rotating circular plate at the top of the pylon fairings. This plate had a circular track in which the rotating hub fairing sat and was allowed to rotate freely. The configurations were then tested using a range of Reynolds numbers, angles of attack, and rotational speeds. The primary conclusions of this work were that hub fairings alone increased the model drag, pylon fairings alone decreased model parasite drag and increased horizontal tail control effectiveness, and there exists an optimal hub fairings size for decreasing drag.

This decade would also see reinforced interest in the study of hub wake and wake interactions. Across the late 1990s and early 2000s Gorton et al. [69–71] carried out a series of experimental investigations focused on rotor wake-fuselage-empennage interactions. They conducted multiple wind tunnel tests of a 15% scale model of a Boeing-Sikorsky RAH-66 helicopter mounted with a scale model of a fully articulated 4-bladed rotor hub. While thorough these studies focused mainly on the rotor blade wake and not the hub wake. An unexpected 2/rev fluctuation in the velocity was noted and its was theorized that it may be connected to the vortices shedding noted in Ref.[63].

The same rotor head configuration was moved to a generic test system and coupled with rectangular blades for another study conducted in 1997 by Berry [72]. visualizations were taken using laser velocimetry (LV) as in previous studies. This work also identified an unexpected 2/rev fluctuation in the flow. The hub flow was characterized into two parts, one being attributed to the periodic passage of the lade and the second attributed to the aperiodic/turbulent flow. The aperiodic fluctuations in the flow were found to be significantly stronger on the retreating side of the rotor hub.

In 2013, Raghav et al. [73] conducted low speed wind tunnel tests in the John J. Harper low speed wind tunnel at the Georgia Institute of Technology. A quarter scale generic four bladed rotor hub model was used, which included structures representing blade shanks, a swashplate, pitch links, and a drive shaft/rotor mast. Tests were conducted on a hub with unplugged blade shanks, one with plugged blade shanks, and one with plugged blade shanks and a capped region between the upper and lower hub plates. This study also incorporated CFD predictions, the findings of which will be further discussed in the next section. Experiments were conducted using a azimuthal sweep with a static hub, which were followed with a rotating test conducted on the hub with plugged shanks over a range of rotational speeds. Deconstruction of the hub also allowed for the investigation of the individual pieces in the assembly to the overall drag. The study found that the hub plates and blade shanks contributed significant portions of the hub drag, and the rest of the drag was generated by separation around the drive shaft, pitch links, and the swashplate. These experiments were part of an extensive experimental/CFD effort which is further discussed in the next section of this work.

2013 also marked the beginning of early efforts in what would become a long series of experimental investigations, in conjunction with computational efforts, headed by members of the Pennsylvania State University's Applied Research Laboratory (PSU-ARL). Reich et al. [74] noted a lack of data pertaining to the long-age rotor hub wake structures, particularly in distance where they would interact with the empennage. To address this a series of experiments on rotor hub test models, based on a larger commercial hub, were conducted in both their 12” watertunnel and the 48” Garfield Thomas Water Tunnel (GTWT), covering both low and high-speed test conditions. The model did not feature pitch links but did feature scissor arms. The choice to use a water tunnel was motivated by the ability to adequately scale the Reynolds number to the experimental model without requiring full scale Mach number. CFD predictions were also carried out, as was becoming more common practice during this time. The results showed strong 2/rev, 4/rev, and 6/rev content in both the near and far wake. It was noted that while the 4/rev and 6/rev content lost strength with increase downstream distance the 2/rev content remained strong into the far wake region further confirmed by their LDV measurements. Ultimately, the tests showed that multiple per revolutions flow structures attributed to the hub and its components persist for long downstream distances.

Later, Reich et al. [75] would use another watertunnel experiment to examine the effects of advance ratio, μ, and hub Reynolds number, Re_{hub} on hub drag, with the final goal of the work being to find the minimum Re_{hub} required for accurate scale model testing. Watertunnel experiments using a scaled down version of the hub used by Reich et al. [74], which had been modified to allow for testing at various levels of hub defeaturing and to include beanie fairings. Two fairings generic fairings with ellipsoid tops and flat bottoms were used. The experiments were conducted over a range of Re_{hub}, rotation speed, and free stream velocity conditions designed to maintain specific advanced ratios. The results of these experiments showed that ultimately the unsteady rotor hub wake content is both configuration and Reynolds number dependent, which indicated the need for full scale Reynolds number testing for accurate wake measurements. It was also determined that full-scale Re_{hub} tests were needed to obtain accurate drag results for specific designs.

The contributions of PSU-ARL to the study of rotor hub wake structures and drag contribution would continue over 2010s in the form of the Rotor Hub Flow Prediction Workshop series. This series began with the intention of bringing experts in both experimental and CFD techniques to bear in a concentrated effort to investigate rotor hub wakes. Contributions included efforts from Both PSU and Georgia Tech’s Vertical Lift Research Centers of Excellence (VLRCOE), in collaboration with several other academic, government, and industry entities, including UTK. The first workshop was hosted in 2016 at Penn State and the findings of the resultant experimental findings and the comparisons to the CFD predictions are summarized by Schmitz et al. [12].

Water tunnel experiments were conducted in using the GTWT facility as in previous PSU works and were conducted in different phases, with the ultimate goal being to conduct the first full-scale Reynolds number test of a model rotor hub of a large helicopter in a water tunnel. The Phase I VLRCOE tests were carried out on a 1/4.25 scale rotor hub model, constructed using stereolithograph (SLA) materials, at PSU-ARL in 2012. These experiments were designed to characterize long-age wake at high Reynolds number, and the wake was surveyed using PIV and LDV. These experiments were followed with the Phase III VLRCOE tests conducted in 2016 after the first Rotor Hub Flow Prediction Workshop, and were designed to collect force/moment and wake data from 1/4 scale Reynolds number to full scale Reynolds number. The Phase III experiments used a modified experimental setup which allow for more accuracy in the hub forces. A similar hub to the Phase I experiments but made from aluminium as opposed to the SLA materials from Phase I. This hub was dubbed the VLRCOE Phase III Baseline Hub. These experiments also featured revised LDV measurement location layout to make comparison to eliminate the issue of potential wake misalignments when compared to the computational predictions. CFD predictions for the hub wake were conducted in conjunction with the Phase III experimental using OVERFLOW using a multiple different CFD software to build a comprehensive set of data for comparison. Wake harmonics and hub surface forces were compared between the computational predictions and experimental findings. In the context of comparing computation and experimental findings several conclusions were drawn. First phase averaging of the surface forces showed notable dependence on the number of hub revolutions included in the process. The added LDV measurement points increased the reliability of the harmonics and improved the comparisons to the computational data. In addition, both the experimental and computational findings showed a strong 6/rev content in the wake harmonics, which were regard as a harmonic of the 2/rev content and interactional aerodynamics between the 2/rev and 4/rev content.

These works were continued into the 2nd Rotor Hub Drag Prediction Workshop held at Penn State in 2018. As before this was a collaborative efforts between CFD and experimental experts. Schmitz et al. conducted a blind comparison between the experimental and computational data for the 2nd workshop [76]. Another round of experimental tests was conducted in the Garfield

Thomas Water Tunnel and used both the Phase III baseline hub geometry and a new 'Low Drag' hub. The Low Drag hub was designed to mimic a next generation high-speed helicopter hub. All the blade shanks were replaced with Sikorsky DBLN 526 airfoil, which was inverted to increase their aerodynamic quality. Experimental testing and measurement were conducted similarly to the previous work but with an airfoil situated 7 hub diameters downstream. This airfoil was as a notional horizontal stabilizer to examine the hub wake interactional aerodynamics. Force data was collected from this foil and compared to CFD predictions.

The results of this study when compared to the computational predictions showed that the CFD methods predicted average hub drag to within 5% of the Interactional Aerodynamic Experiments. The lift agreements from the downstream airfoil showed decent agreement between the experimental and CFD results, however it was shown that a large number of hub revolutions were needed for as reference for time to the phase average-time series of the stabilizer lift. This suggested that the phase averaged analysis of the foil force data might be able to serve as adequate comparisons for CFD results. Finally, efforts toward designing and optimizing a reduced order model BEM/frontal area for predicting hub drag harmonics showed good behavior for the Phase III baseline hub but some inconsistency in the harmonics for the low drag hub. It was concluded that an inflow model should be paired with the reduced order model for increased accuracy in predicting phase averaged hub drag.

2.2.2 Computational Fluid Dynamics

Similar to the history of experimental studies of rotorcraft much of the early computational work on the helicopter was focused on the rotor blades, as their aerodynamic performance directly translated to the helicopter's performance. However, later efforts focused on rotor hub would benefit as a biproduct of these early efforts in several ways. As an example, studies of rotor blade downwash with the fuselage before the turn of the century were carried out using comprehensive rotor blade codes to model the blades and their downwash, and panel-based potential methods to model the fuselage. Some examples of this can be found in Ref. [68, 77, 78]. These methods had several limitations, primarily they lacked the ability to accurately capture realistic viscous interactions between the rotor wake and the fuselage [78]. As computational hardware advanced however Reynolds Averaged Navier-Stokes (RANS) computational methods [79] were adopted more widely.

Similarly, the development of computational grid generation techniques saw much attention in studying other aspects of rotorcraft performance. As was noted by Ruffin et al. [80] in 2004, one of the largest issues facing rotor craft CFD was the complex nature of their geometry, which carries over to the rotor hub. The creation of structured computational grids for the exterior of a rotor craft could take large amounts of time and require large amounts of resolution, i.e. large numbers of grid points. Both issues are only exacerbated when attempting to model the rotor hub which is normally omitted from blade/fuselage-based studies.

One of the earliest solutions to the complexity problem was the use of structured, overset grids. Ruffin et al. [80] compared the performance of unstructured and structured solvers. CFD predictions made using two unstructured grid generation methods, a tetrahedral based and a Cartesian grid based, were compared to those made using a structured overset grid method. It was found that all three tested methods provide good agreement with the experimental values. The unstructured grids proved easier to construct but offered a lower grid efficiency than the structured methods.

In 2010, as part of an exhaustive computational study of the HART II rotor [81, 82], Lim et al. [1] studied the effects of the rotor hub on blade-vortex interactions (BVI) and rotor wake. The authors created three computational geometries, two of which included the hub modeled as a basic cylinder which are shown in Fig. 2.16. OVERLOW 2 was coupled with CAMRAD II in [83] to provide both CFD and computational structural dynamics (CSD) predictions, respectively. Lim et al. found that the presents of the hub created strong turbulence due to interaction with its surrounding components but this turbulence has little effect on the rotor airloads and trim.

Somewhat similar to the HART II campaign, the GOAHEAD project, initiated in 2005, was a multi-partner CFD/experimental data set generation and validation campaign. It was motivated by a lack of comprehensive helicopter data sets for CFD validation in the European helicopter research. The CFD and numerical portions of this project were presented by Antoniadis et al. [2], in 2012. Several different CFD solvers were implemented, including FLOWer[84], HMB [85], ENSOLV [86], ROSITA [87], and ElsA [88]. Several different techniques for modeling the relative motion between the blades and the fuselage were also used. CHIMERA, using overset meshes, and sliding

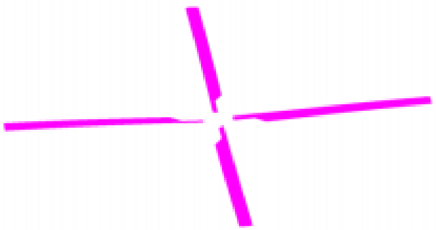

a) Isolated rotor

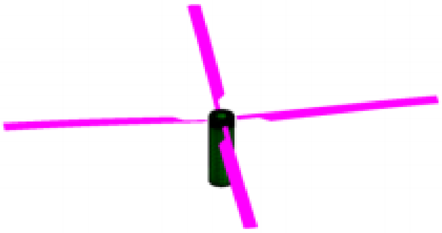

b) Rotor-hub

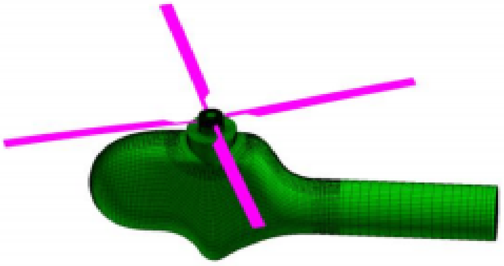

c) Rotor-fuselage

Fig. 2.16 HART II Grid Systems[1]

grids [89] and disk techniques were used with the majority of the participants using CHIMERA. A horizontal stabilizer was placed on the tail and used to gather information on the hub and fuselage wake. The main finding of work in regard to rotor hubs was that in the area down stream of the hub and fuselage back door, both the experiments and the CFD predictions captured irregular and highly unsteady flow behavior however, this region also represented the principal area of disagreement between each of the test cases. Shown in Fig. 2.17 are the flow separation visualizations for the top of the horizontal stabilizer and the tail of the test fuselage, with red indicating regions of separated flow.

In 2013, the results of one of the most comprehensive efforts in research focused on the hub drag were published by Shenoy and Smith [11]. This was a two-part experimental and computational effort focused on improving the understanding of the various contributors to hub drag and how their effects scaled with Reynolds number or other flight parameters. The goal of the computational aspects specifically were to reduce the then current amounts of uncertainty in numerical predictions through the use of experimental hub drag scaling effort. The study made use of NASA's VGRIDns software for grid generation and paired SUGAR++ with DiRTlib to produce the overset grid systems required to capture rotational movement relative to non-rotating elements. The FUN3D unstructured solver was used to produce both hybrid URANS/LES predictions for different parts of the flow. The experimentally aspects of this effort were discussed previously.

Several works were produced either while conducting this work or in affiliation with it [3, 11, 73, 90–92]. In 2011, Shenoy et al. [90] investigated the difference in CFD prediction for a 25-percent scale and full scale model hub geometry, using a representative 4-bladed hub based on a UH-60A hub. It was found that components which were bluff bodies, such as the pitch links or blade shanks, created non-linear scaling of Reynolds number and interference drag effects. It was also noted that determining interference drag for rotating components of the hub needed to include shifted estimations in the wake shedding due to the Magnus effect. One of the largest findings was that using the advanced rotation to scale the velocity rather than hub angular momentum more accurately scaled the physics of the hub flow. This study is also notable as it was one of first to use hybrid RANS and Large Eddy Simulation (LES) methodology.

In the same year Shenoy et al. [23] examined the different sources of hub drag with the aim to reduce the error in empirical predictions of hub drag for conceptual designs. The complete hub

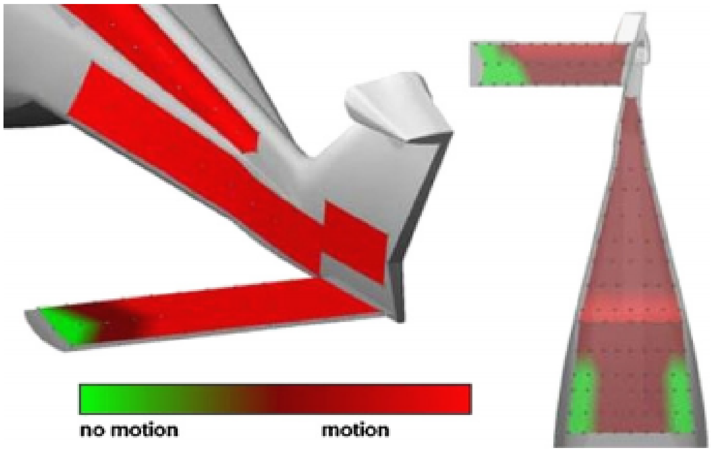

Fig. 2.17 GOAHEAD Flow Separation Regions[2]

as well as isolated individual components were tested, both statically and in rotation. It was found that the hub plates and blade shanks accounted for approximately one-third of the hub drag at the tested velocities and Reynolds numbers. What remained of the hub drag was found to be generated by flow separation about the rotor shaft, pitch links, and swashplate. Minimal differences in the predicted drag were also seen between rotating and static hub tests. An anisotropic grid adaptation tool was tested and found to enhance the computational grids ability to capture the complex physical interactions around the hub.

Raghav et al. [3], followed in 2012, with an investigation of the physics of hub drag. Using the same geometry and methodology as the previous works, this study focused specifically on the physics of the wake. The most pertinent finding of this work was that the rotating turbulent spectra showed strong, high energy 4/rev and 8/rev frequency content which were absent in the static turbulent spectra. The Power Spectrum Density (PSD) of the velocity fluctuations for the CFD predictions and experimental results, as presented by Raghav et al. are shown in Fig. 2.18, and the difference between the static and rotating hubs 4/rev and 8/rev content is clear to see.

Another work conducted by Shenoy et al. [91] built upon the earlier works and focused on the effects of Reynolds number scaling. Four test cases were used, all of which added the NASA ROBIN[93] fuselage beneath the hubs. The two static cases were conducted at the 0^o and 45^o positions and the two rotating cases conducted with μ = 0.395 and μ = 0.152, which corresponded to the wind tunnel experiments conducted in the previous works. Two Reynolds number were used, Re = 0.29×10^6 and Re = 8.14×10^6, with an additional case being was run at the lower Reynolds number without the fuselage beneath the hub. The findings for the static hubs showed that bluff body components, such as the rotor mast or pitch links caused non-linear scaling in drag due to a combination of the Reynolds scaling and changes in interference drag. The rotating cases were found to scale non-linearly and showed clear influences from the angular velocity. Increased angular velocities were sown to cause increased interference effects for the upper portion of the hub which in turn caused significant changes in the drag and Magnus effects based on the Reynolds scaling.

In 2014, Khier [4] used the findings from the previously discussed GOAHEAD project to study hub drag reduction via streamlined hubs, using the DLR-developed unstructured finite volume solver, TAU. The CENTAUR grid generation software was used, with the grids being combined

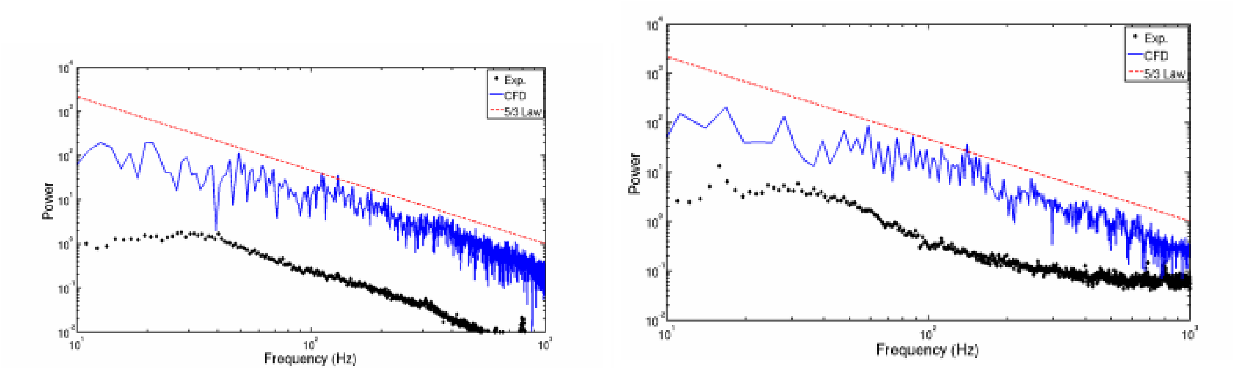

(a) Static Hub **(b)** Rotating Hub (240rpm)

Fig. 2.18 Power Spectrum Density Of Velocity Fluctuation[3] via CHIMERA. The computational model was created based on the same model used in the GOAHEAD experiments but with an altered horizontal stabilizer and the addition of sponsons, this model was designated the GRC2. A second computational model was created by blending the shaft fairing and engine cowl to study the aerodynamic interference between the hub and fuselage. These two hubs were combined with two fairings designs to create four test cases. Two cases, featuring the original and modified geometry with the same fairing, were tested over α = -15^o to 15^o, and the second two cases, being the original hub with two different fairings, were tested over α = 5^o to 5^o. All cases were conducted using a M = 0.204. A breakdown of the predicted hub drag for the three tests cases using the original configuration can be seen in Fig. 2.19. These results showed that the blade attachments and stubs contributed around 70% of the hub drag for their configurations, which amounted roughly 20% of the overall drag. It was found that streamlining bluff body parts and implementing a fairing could reduced the hub contribution to total drag by 17-19%. However, the effects of these fairings and hub configurations on the dynamics of the vehicle were not considered, so the effects on interference phenomena such as the empennage are unknown.

Similar to other long running experimental/CFD campaigns a broad test program examining the air loads on the UH-60A helicopter rotor system was initiated in 2010 [94]. This campaign produced several works, with most focused on the blade/fuselage; however, the later works in the project conducted by Potsdam et al. [95] in 2016 did take the hub into consideration. Building on a detailed set of experimental tests on a full-scale UH-60A rotor [96, 97], described in the last section of this work. Potsdam et al. were interested in validating their CFD predictions and using them to further the understanding of the high advanced ratio physics. The Helios software, developed by the DOD's High Performance Computing Modernization Office (HPCMO) and CREATE-Air Vehicles, and the US Army. Near body solutions are produced using the unstructured mesh, URANS solver NSU3D.

It was that interactions with strong groups of vortices released from the blade roots, reversed flow regions, and aft most blade caused sharp oscillations in the normal and chord force air loads at all the tested advance ratios. Based on this finding it was concluded that accurate blade root and hub modeling should be included as their interactional aerodynamics had a direct effect on the force prediction for the rotor blades in certain azimuthal positions. Turbulence modeling for rotor hubs has also recently been examined with the work of Coder et al. [98] in 2017. The authors noted that traditional RANS strategies used in modeling rotor hubs could accurately capture the surfaces forces but possessed limited accuracy with respect to wake. As RANS methods inherently treat the flow as fully turbulent it was also noted that these strategies neglected the possible effects of laminar-turbulent transition within the hub flow and wake. To investigate these effects a comparison was conducted between two CFD cases. Both cases used the same flow solver, OVERFLOW, and grids, but used two different turbulence modeling strategies. The first of these two was delayed detached eddy simulation (DDES), which switches between RANS and LES methodologies based a function of stance from surfaces. DDES uses RANS in areas where the turbulent length scale is less than the local grid resolution or in locations near surfaces, but otherwise uses the LES method. The second turbulence modeling strategy studied was HRLES. This method combines the two-equation, $k - \omega$ SST RANS model, developed by Menter, and a Smagorinsky-type LES sub-grid scale model. The HRLES methods switches between these two models is determined by including them as operators on the Navier-Stokes equations and summing then using a specified blending parameter.

Both strategies were used to model flow around a recreation of the Baseline hub geometry and the surrounding water tunnel from the experimental tests conducted by Schmitz et al. [12]. The simulated flow conditions were set to match the experimental conditions and the experimental results used for comparison. The DDES and HRLES were found to under and over predicted the average drag from the experimental results respectively. In addition examinations of their unsteady harmonic content showed the DDES to better match the 2/rev content from the experiments, with the HRLES better matching the higher frequency content. In the wake HRLES was found to be less diffusive, and even further down wake the DDES predicted strong 4/rev structures that the HRLES did not.

Coder [99] further built on this work in 2019, examine the effects of laminar-turbulent transition on CFD prediction of hub drag. Two different modeling strategies were implemented in this work. The first was made use of the Spalart-Allmaras eddy viscosity model, with several modifications, and DDES to allow for hybrid RANS/LES modeling in the wake. This strategy was used to model a fully turbulent flow with no considerations for transition. The second modeling strategy made use of the two-equation variant of the amplification factor transport (AFT), which was initially designed by Coder and Maughmer [100], and was further augmented by Coder [101] to create the version used in this study, designated AFT2017b.

In this study the both the Baseline hub and Low Drag hub geometries from the experiments conducted by Schmitz et al. [76] in 2019 used, with the Baseline hub once again being modeled inside a simulated water tunnel. The Low Drag hub however was modeled in free air. CFD predictions for both the surface forces and the wake were collected as before and compared to the experimental results. Only negligible differences were found between the fully turbulent and transitions CFD predictions for mean hub drag. The modeling techniques were found to have some effects on the unsteady wake harmonics, with the content of different frequencies being increased or decrease depending on the modeling strategy. Overall, it was concluded that the inclusion of transitional modeling had little effect on hub flow modeling and laminar flow showed little potential as a means to reduced hub drag [99].

2.3 Reduced Order Modeling

As has been discussed earlier the complex interactions between the rotor hubs and the incoming flow create a flow field which is chaotic in nature and hard to both experimentally capture and computationally simulate. The computational difficulty stems from the extremely small scale of structures within the rotor hubs wake. This means very fine computational meshes are required in the near body grids and for a larger surrounding area than in other CFD applications. In addition, small time steps are required to accurately capture the rapid changes within hub flows. These two factors contribute to the generate large solution files. The data sets collected in this course were each over 1 TB in size. Even though this set was conservatively collected it still represents a very large amount of storage space on most machines.

Post-processing of on data set of such size can prove quite difficult, especially is computational resources are limited. Reducing the amount of data is not an option, as anything less would not accurately capture the long-term evolution of a rotor hub wake. Reduced-order modeling (ROM) represents one viable solution to this issue. ROM methods are mathematical tools by which large amounts of data can be distilled down to lower order representation that still represents the most important traits of the original set. One of the most commonly used model order reduction techniques is proper orthogonal decomposition (POD).

2.3.1 Historical Development of Proper Orthogonal Decomposition

One of the earliest and most prolific forms of reduced order model is Principal Component Analysis (PCA). As with all forms of reduced order modeling the central aim of PCA is to reduce the dimensionality of a large set of interrelated variables while retaining a majority of the variation contained in the original set [102]. PCA is widely used, and also known as Singular Value Decomposition (SVD), the Empirical Orthogonal Function (EOF) method, and the Karman-Loeve or the Hotelling transform in various applications. PCA works by transforming the original data to a new set of variables called the principal components (PC). The new variables are then arranged such that the first several PCs contain the majority of the variation present in all of the original variables [17].

Singular value decomposition (SVD), which is the underlying mechanism of PCA was developed in the later portions of the 1800s by several different contributors, the works of which are summarized by Stewart [103]. However, the development of principle component analysis are largely accredited to two men, Karl Pearson in 1901 and Harold Hotelling in 1933 [17, 102, 104–106]. While the independent methodologies differ, both arrive at the basic idea of principle component analysis. Pearson's work in 1901 [107] was focused on identifying a line or plane of best fit through a set of one, two, or higher dimensional data sets. Hotelling formations of PCA focused on the identification of independent variables within large set which determined the values of the rest of the set. Hotelling's method then selected variables which maximized their contributions to the total total variance of the full variable set. Hotelling then arrived at the use of an eigenvalue problem.

Principle Component Analysis at its core is a relatively simple process. Jolliffe [102] broke the process down into several steps defined as follows. If presented with a vector x composed of p random variables whose correlations and covariances are of interest looking directly at the variables variances, correlations, or covariances. A new set of derived variables, which is much smaller than p can then be developed. These derived variables are created such that they preserve the nature of the original variances and correlations. The first step is to define the new Principle Components as the linear function $\alpha_1' x$ of the components of x.

$$\alpha_1' x = \alpha_{11}x_1 + \alpha_{12}x_2 + \cdots + \alpha_{1p}x_p = \sum_{j=1}^{p} \alpha_{1j}x_j \tag{2.1}$$

This defines the first principle component, which would contain the largest fraction of the original variance. Here α is a vector of constant that has a length p. Subsequently more PCs can be defined as $\alpha_2' x$, $\alpha_3' x \ldots \alpha_k' x$, with the criteria that each PC contain the maximum variance of the original set while being uncorrelated with the previously defined PCs. Mathematically up to p number of PCs can be derived from the original set and used to represent it; however, this defeats the purpose of the PCA process. Should the variables in the original set display strong correlation, then the first few PCs will generally capture a majority of the variation in that set.

It is generally agreed that the first instance of the application of PCA, under the guise of POD, to the study of turbulent flow was proposed by Lumely in 1967, [108]. Lumely would go on to be one of main contributors to the use of POD in application to aerodynamics and turbulence, working with several other authors to publish a series of works on the topics Ref. [109, 109–114].

2.3.2 Variants of Proper Orthogonal Decomposition

A brief discussion of the classical formulation of the POD process and several variants is given here to lend context to the history of its application to fluid flows and aerodynamics; however, in depth discussion of the underlying mechanics and algorithm for the POD process is withheld until Chapter 3. The classical formulation of POD applied to fluid flows as suggested by Lumely [108] is at its core simple. Instantaneous realizations of a stochastic process, such as turbulent flows, were captured at discrete times, and used to construct a stochastic ensemble X. This matrix is then decomposed into a set of deterministic functions ϕ and expansion coefficients a, as seen in Eq.2.2.

$$X = \Sigma a \phi \tag{2.2}$$

In it classic formulations each realization of the stochastic process is treated as an independent realizations of the process. In application to fluid flows this means every instance at which a flow field is measured is used as an entry in X. An eigenvalue decomposition is then used to decompose

X into its eigenvalues and eigenvectors as in Eq.2.3

$$Xv = \lambda v$$
$$X = V\Lambda V^{-}1 \tag{2.3}$$

Here X is a $n \times n$ data matrix, V is an $x \times n$ matrix whose columns are the eigenvectors, v, and Λ is a $n \times n$ diagonal matrix, whose entries diagonal indices are the eigenvalues λ. The eigenvalues indicate how well the eigenvectors represent the original data [115].

The main draw-back of this method is that it requires that all of the matrices be square $n \times n$. If applied to computational fluid dynamics this immediately present a problem as each instance of flow will be captured at every grid point, which will set the length of the vector representing that instance as n is equal to the number of grid points. The eigenvalue decomposition then requires the calculation of three $n \times n$ making it computational intractable for modest grid resolutions. Fortunately, there exists a generalization of the eigenvalue decomposition which allows them to be applied to rectangular matrices, the singular value decomposition. The SVD decomposition is shown in Eq.2.4

$$X = U\Sigma V^{*} \tag{2.4}$$

Here, * indicates the Hermitian transpose, X is a rectangular $m \times n$ matrix, U is a $m \times m$ unitary matrix, V is a $n \times n$ unitary matrix, and $\sum$ is a $m \times n$ diagonal matrix with non-negative entries that are provided in descending order. The columns of U and V are composed of the right and left singular vectors, respectively, and the diagonal entries of $\sum$ called the singular values. The right singular vectors are equal to the eigenvectors of the matrix XX^{*} and the left singular values the eigenvectors of the square matrices $X^{*}X$. The singular values are simply the square root of the non-zero eigenvalues of XX^{*} and $X^{*}X$. One of the most commonly used forms of POD used in the modern era was introduced by Sirovich in 1987 [116–118]. Sirovich noted that even for crude flow simulations the size of the of matrices required for classic POD would be prohibitively large. This could make the POD process too computationally expensive for the computers of the era. As a work around to this issue Sirovich suggested that using the SVD in conjunctions with a small set of 'snapshots' at discrete instances in time, with the number of snapshots being far smaller than the number of spatial degrees of freedom of the system, would greatly reduce the cost of the POD. For this method to produce optimal results it must incorporate enough snapshots to accurately resolve any important fluctuations within the flow and should capture a majority of the modal energy. Due to its reduction is computational cost this method became intensely popular in the study of high dimensional fluid flows [115].

However, this computational saving came with one major drawback. The treatment of every individual flow field solution as a independent realization of the flow mean that time was treated as a stochastic variable. Thereby the modes produced from snapshot POD are only spatially correlated. This disregards the temporal evolution of flow which means it cannot capture structures which evolve over space and time.

The form of POD originally proposed in application to fluid flows by Lumely in 1967 actually avoid the draw-back of Sirovich's snapshot method. This method was later given the name spectral proper orthogonal decomposition by Picard and Delville [119] in 2000. This method functions by building the stochastic ensemble X out of time-dependent realization of the stochastic process. For example, a flow simulation might be divided into equally sized time chunks with each chunk being treated as an entry in the stochastic matrix. This matrix is then subjected to a Fast Fourier Transform. Then the Fourier realizations are used in the singular value decomposition. This identifies POD modes that oscillate at single frequency. The modes produced via this process are both spatial and temporally coherent. When applied to fluid flows, this mean that the modes can described structures that evolve in both space and time. The early 2000s also saw the creation of a novel POD form called balanced POD by Willcox et al. [120]. Willcox et al. noted that the POD methods of the time focused heavily on information relevant to the system inputs with little regard for system outputs. Two major issues were connected to this oversight, the first being that a lack of consideration for the relation between the outputs and states of a system would lead to the creation of less efficient models. The second issue noted was that a model reduction procedure based only on system inputs would potentially be highly inaccurate based on the scaling of the state variables. To address these issues Willcox et al. proposed a novel decomposition which combined concepts explored by Moore [121], Dowell and Hall [122], and Lall et al. [123]. Lall et al. had noted a relation between the system grammians and the POD, and subsequently used a Karhunen-Loeve decompositions to obtain an approximate balanced truncation.

This could prove computational prohibitive however, so Willcox et al. instead used snapshot POD to approximate the grammians of the system. This resulted in a more efficient approximation of the grammians. However, it was noted by Rowely [124] that the method of Willcox et al. had several drawbacks. These being that the reducing the rank of the system grammians ran the risk of prematurely truncating poorly observed states and that the method becomes unusable when the number of system outputs become large. By computing the balancing transformation directly from the set of snapshots used, this removed the need for the individual reduction of each grammian and the need for a separate eigenvector. A low-cost method of calculating the grammians with few adjoint calculations even when large outputs were involved is also proposed in this work. Rowely's method is succinctly summarized in Ref. [124]. This work resulted in a more efficient methodology for model reduction using balanced truncation in conjunction with POD and served to highlight the relationship between POD and balanced truncation, showing that for a linear system balanced truncation is simply a special case of POD.

In 2008 and 2010, Schmid et al. [125, 126] proposed a novel decomposition method which was based on flow snapshots, like Sirovich's method but would still yield fluid structures which accurately encapsulated the flow motion. The flow structures produced by this method were dubbed 'dynamic modes' and the method itself 'dynamic mode decomposition' (DMD).

Similar to the snapshot method, DMD begins by collecting a sequence of snapshots from a flow field in a matrix V_1^N, with N denoting the last entry of the matrix and the ith snapshot in the matrix being designated v_i. This matrix is constructed as an ordered data sequence using a constant time step Δt between each snapshot. By assuming a linear mapping A between each snapshot the collection can be re-written as a Krylov sequence,

$$V_1^N = v_1, Av_1, A^2 v_1, ..., A^{N-1} v_1 \tag{2.5}$$

As with other methods of modal decomposition when the number of snapshots is increased the better the dominant features of the flow are captures. After a certain point adding more snapshots does not improve the vector space spanned by the vector V_1^N, so the addition of more snapshots after this point can be instead represented using a residual vector r. Using a matrix form and some fundamental concepts in series representations Eq. 2.5 can be re written as in Eq. 2.6

$$AV_1^N = V_2^N = V_1^{N-1}S + re_{N-1}^T \tag{2.6}$$

where $e_{N-1} \in \mathbb{R}^{N-}$, and S is a companion matrix with the form seen in Eq. 2.7.

$$S = \begin{pmatrix} 0 & & & & a_1 \\ 1 & 0 & & & a_2 \\ & \ddots & \ddots & & \vdots \\ & & 1 & 0 & a_{N_2} \\ & & & 1 & a_{N-1} \end{pmatrix} \tag{2.7}$$

However, attempting to use this formation of S in the decomposition can lead to problems, especially when used on experimental data. To counter this Schmid et al. used a SVD on V_q^{N-1}, and then using that decomposition in Eq. 2.6 and rearranging the results to the form seen in Eq. 2.8.

$$U^H AU = U^H V_2^N W \Sigma^{-1} \equiv \tilde{S} \tag{2.8}$$

In this form $\tilde{S}$ represents a transformed 'full' version of S and the H superscript denotes a Hessenberg matrix. In essence this process is the projection of A onto a POD basis. The dynamic modes are solved for as $\phi_i = Uy_i$, with y_i being the ith eigenvector of $\tilde{S}$ and U being the right singular values of V_1^{N-1}.

2.3.3 Other Forms of ROMS

While POD is one of the most commonly used techniques for model order reduction and high dimensionality data visualizations, a multitude of other methods exist. The development of several POD variants drew heavily from a form of reduced order modeling called Balanced Truncation and more specifically form the work of Moore [121]. Rowely [124] gives an excellent description of balanced truncation which is summarized here for later context. Balanced truncation is a method for reduced order modeling of linear input-output systems. Unlike modal decompositions which focus exclusively on the outputs of a process, balanced truncation was designed to examine both the inputs and outputs of a system before determining which states to retain when constructing the reduced-order model [120]. Balanced truncation revolved around defining two grammians, the controllability and observability grammian. For a linear stable system such as

$$\begin{aligned} \dot{x} &= Ax + Bu \\ y &= Cx \end{aligned} \tag{2.9}$$

the two grammians are defined as

$$\begin{aligned} W_c &= \int_0^\infty e^{At} B B^* e^{A^* t} dt \\ W_o &= \int_0^\infty e^{A^* t} C^* C e^{At} dt \end{aligned} \tag{2.10}$$

Here the asterisk denotes the complex conjugate transpose. The degree to which each state is excited by a specific input is captured in the controllability grammian W_c while the observability grammian, W_o measure the degree to which each state excites future outputs. If the system was more easily driven to one state than another, that state was considered more 'controllable' and if a certain state excited a larger output signal than another that state was considered more 'observable'. One of the most important aspects of the grammians is their dependence on the coordinates. Should the coordinate system be shifted, for example as, $x = Tz$ the grammians will transform as

$$\begin{aligned} W_c &\rightarrow T^{-1} W_c T^{-1} * \\ W_o &\rightarrow T^* W_o T \end{aligned} \tag{2.11}$$

a balanced truncation comes from a shift in coordinates which results in the transformed grammians being equal and diagonal.

One of Moore's primary contributions to this was the introduction of the empirical grammians, i.e. grammians found from numerical simulation data. For this method system responses to inputs are compiled into a vector $B = [b_1, .., b_p]$, thus $x_p(t) = e^{At} b_p$. For the observability grammian the impulse response to the adjoint system $\dot{z} = A^{*}z + C^{*}v$, where C^{*} is a vector with q number of entries, equal to the number of responses. This yields the form $\dot{z}_q(t) = e^{A^{*}t}c_q$. The grammians are then found as follows

$$W_c = \int_0^{\infty} (x_1(t)x_1(t)^{*} + ... + x_p(t)x_p(t)^{*})dt \tag{2.12}$$

$$W_o = \int_0^{\infty} (z_1(t)z_1(t)^{*} + ... + z_q(t)z_q(t)^{*})dt \tag{2.13}$$

$$\tag{2.14}$$

Several things should be noted about this process, the first being that it is intractable for high numbers of outputs, as each output requires a unique adjoint system and second that the forms seen in Eqn. 2.14 are very similar to the solutions for classic POD. This is because the POD modes for the impulse responses are simply the most controllable modes. This connection is one of the key factors in the development of Balanced POD.

2.3.4 Applications in Fluids Dynamics and Aerodynamics

While Lumely proposed the used of POD on experimental results in the field of fluid dynamics, this method of post processing only began to gain traction in the 1980s. In its early application to fluid flows POD, and its variants, were largely applied to the identification of coherent structures in turbulent flow. In 1987 Glauser et al. [127] used SPOD to reveal the existence of a large-scale structure in the mixing layer of jet flow. A scalar, one-dimensional version of orthogonal decomposition that used a one-dimensional cross-spectra measurement based on the Fourier transform of the streamwise velocity of the jet flow was implemented. A large structure which contained approximately 40% of the turbulent energy was identified, with another 40% being contained in second and third order structures, i.e. modes. The shot noise decomposition, another decomposition technique proposed by Lumely [108], was used to extract the shape of this structure and it was found that resembled a roller eddy similar to those found in other studies. Based on their results it was suggested that large scale features in flow could be represented used a direct decomposition of the Navier-Stokes equations, with smaller structures being modeled more traditionally. Across the late 1980s and 1990s snapshot POD and SPOD would see application to a myriad to fluid flows such as channel flow [128] and mixing layers [129].

In 2000 Hall et al. [130], similar to other works at the time, moved from their previous techniques reducing the complexity of unsteady models for aerodynamics to developing and applying POD. Previously Hall et al. [18, 131–135] had used a form eigenanalysis to create reduced order models for flows around airfoils, wings, and turbomachinery. In place of these techniques Hall et al. [130] worked to develop a frequency-domain form of POD. Using CFD predictions for airfoils vibrating at different frequencies in the frequency domain. POD was then used to extracted the basis vectors from the frequency-domain, these basis vectors were then used in a cell-centered Godunov scheme, as described in Ref. [136], to create the aerodynamic and aeroelastic ROMS. The flow model was then paired with a structural dynamic model to create a model for airfoil fluttering. The constructed ROMs showed good accuracy when applied to two dimensional models of a single transonic airfoil and an airfoil cascade. It was also noted that, as in the case of this work, the largest computational cost was accrued during the initial CFD prediction for the unsteady airfoil flow.

Beginning in 2002, Johansson et al. [137] began applying SPOD in the study of axisymmetric turbulent wake behind a disk. SPOD was used on three fixed, downstream, cross-sections of the wake. Johansson et al. [138] followed this work with another in 2006. In these works, the application of SPOD revealed a that energetic structure of the axisymmetric wake could be efficiently described in terms of only a few of the SPOD modes. The first mode was found to contain approximately 56% of the modal energy. Tutkun et al. [139] used SPOD to study the axisymmetric turbulent far wake of a disk. The main objective of the study was to investigate the effects of varying numbers of components used to compose the two-point correlation tensor used in the modal decomposition process. One component scalar and two- and three- component vector velocities were used to build the cross-correlation tensors which were then used in a SPOD process. It was found that, at least in the case of axisymmetric wake, as long as the streamwise velocity was included in decomposition very little variation was seen between the one, two, or three-component implementations of SPOD. Mula et al. [140, 141] used SPOD to study the characteristics of a vortex filament emanating from a single-bladed rotor. Gathering experimental data from single bladed rotor the author’s main objective was to better understand the structure of tip vortices from a rotor in hover. Two POD methodologies were applied. The first was the SPOD methodology, similar to that implemented by Glauser et al. [142]. The vortex was first decomposed in azimuth via a Fourier transform, followed by a radial decomposition using POD. This generated POD modes with associated Fourier modes. In this work the first three Fourier modes were dubbed the axisymmetric, helical and double helical and illustrated center aspects of the flow. For example, the first Fourier of the first POD mode, the axisymmetric mode, described the radial profiles of axial vorticity and circulation in the vortex filament. Snapshot POD was the second method applied and it was found that the first snapshot POD mode captured 75% of the resolved energy from the turbulent motions of the flow at all the studied vortex ages.

Also focusing on rotor blades series of works was published from 2017-2019 by Ramasamy et al. [143, 144] and Sanayei et al. [145]. This set of studies set out to help investigate dynamic stall on pitching airfoils representing helicopter rotor blades. The first of these studies [143] used POD on a set of experimentally gathered, phase-locked velocity field measurements around pitching airfoils. The application of POD showed that the first few POD modes were capable of capturing cycle-to-cycle variations very efficiently. The authors suggested the use of POD modes in conjunction with traditional phase averaging as a means of CFD validation. A distinctive bifurcation of flow statistics between pitching cycles was found, and it was shown that the traditional phase averaging and lift/moment coefficients methods of post processing failed to accurately capture both the bifurcated nature and a majority of the cycle-to-cycle variation [145]. Using a novel clustering process the cycle data was gathered into groups which displayed similar behaviors in certain characteristics, POD was then used on the clustered data to find the average behaviors. This method proved more accurate in capturing the flow variations and physical mechanisms of the flow but also yield substantially different maximum lift/moment coefficient values [144]. This serves to highlight how POD's inherent abilities to identify mean behaviors can be used for improved post processing of data.

The previously discussed work by Coder [99] implemented SPOD to study the wake of one of the rotor hub geometries using the same code as utilized in this research. The SPOD modes showed a high energy 1st mode with subsequently less energetic modes. It was found that the 2/rev frequency contained the highest energy despite a lack of any 2/rev geometric forcing. While no real spatial coherence was seen in the shapes of the 2/rev or 4/rev modes, distinct coherence was seen in the 8/rev content.

POD based investigations of the dynamic stall phenomena on rotor blades was also investigated by Wen and Gross [146] in 2019. The authors gathered CFD prediction for an airfoil section in isolation and then used a ensemble empirical mode decomposition (EEMD), a variation of the empirical mode decomposition (EMD) first introduced by [147]. This method works by extracting the local maxima and minima from a time-dependent signal, $x(t)$, interpolating between these points to find upper and lower bounds for the data, and then subtracting the mean of the upper and lower bound from signal. This is repeated until the result of the subtraction is minimal different, with result begin considered converged and saved as a mode. This mode is then subtract from the original signal and the process repeated. The results obtained from that method were then compared to those obtained from applying a traditional POD to the same flow. It was concluded that while POD was capable of identifying anomalous vortex shedding associated with dynamic stall, the EEMD method was more efficient and the modes generated via this method easier to interpret than POD modes.

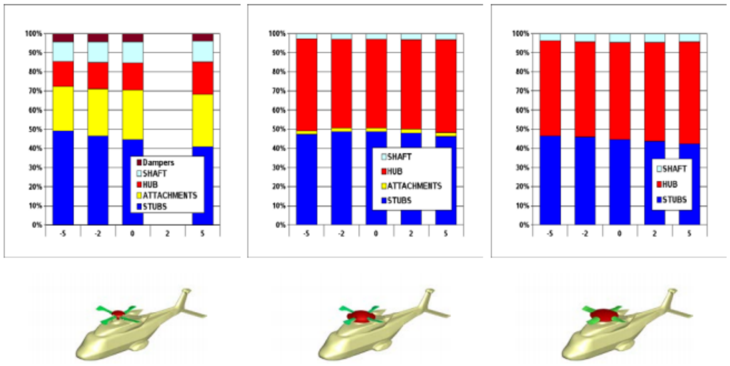

Fig. 2.19 Hub Drag Breakdown for GRC2 Model Variations[4]

Chapter 3: Computational Methodology

3.1 Computational Solver and Governing Equations

All CFD prediction in this study were made using OVERFLOW2.2n[148]. Created and maintained by NASA, OVERFLOW time-marching implicit solver for the Navier Stokes equations. OVERFLOW uses structured overset grids and has six degree-of-freedom capabilities which allow for the simulation of dynamic grid motion in multiple dimensions. OVERFLOW makes use of a curvilinear transformation of the generalized Navier-Stokes Equations. The transformed Navier-Stokes equations can be written in non-dimensional, conservation law form,

$$\partial_\tau \hat{q} + \partial_\xi (\hat{E} - \hat{E}_\nu) + \partial_\eta (\hat{F} - \hat{F}_\nu) + \partial_\zeta (\hat{G} - \hat{G}_\nu) = 0 \tag{3.1}$$

$$\hat{q} = J^{-1} \begin{bmatrix} \rho \\ \rho u \\ \rho v \\ \rho w \\ e \end{bmatrix}, \quad e_0 = C_v T + \frac{1}{2}(u^2 + v^2 + w^2), \tag{3.2}$$

$$\hat{E} = J^{-1} \begin{bmatrix} \rho U \\ \rho u U + \xi_x p \\ \rho v U + \xi_y p \\ \rho w U + \xi_z p \\ (e+p)U - \xi_t p \end{bmatrix}, \hat{F} = J^{-1} \begin{bmatrix} \rho V \\ \rho u V + \eta_x p \\ \rho v V + \eta_y p \\ \rho w V + \eta_z p \\ (e+p)V - \eta_t p \end{bmatrix}, \hat{G} = J^{-1} \begin{bmatrix} \rho W \\ \rho u W + \zeta_x p \\ \rho v W + \zeta_y p \\ \rho w W + \zeta_z p \\ (e+p)W - \zeta_t p \end{bmatrix} \tag{3.3}$$

In this form, $\hat{q}$ represents the vector of conserved variables, within which u, v, and w are the Cartesian velocities variables and e_0 is the total energy, which is given by Eq. 3.2. $\hat{E}$,$\hat{F}$, and $\hat{G}$ are the inviscid fluxes. The viscous terms denoted by the subscript v are defined as follows.

$$\hat{E}_v = J^{-1}\begin{bmatrix} 0 \\ \xi_x\tau_{xx} + \xi_y\tau_{xy} + \xi_z\tau_{xz} \\ \xi_x\tau_{yx} + \xi_y\tau_{yy} + \xi_z\tau_{yz} \\ \xi_x\tau_{zx} + \xi_y\tau_{zy} + \xi_z\tau_{zz} \\ \xi_x\beta_x + \xi_y\beta_y + \xi_z\beta_z \end{bmatrix}, \quad \hat{F}_v = J^{-1}\begin{bmatrix} 0 \\ \nu_x\tau_{xx} + \nu_y\tau_{xy} + \nu_z\tau_{xz} \\ \nu_x\tau_{yx} + \nu_y\tau_{yy} + \nu_z\tau_{yz} \\ \nu_x\tau_{zx} + \nu_y\tau_{zy} + \nu_z\tau_{zz} \\ \nu_x\beta_x + \nu_y\beta_y + \nu_z\beta_z \end{bmatrix}, \tag{3.4}$$

$$\hat{G}_v = J^{-1}\begin{bmatrix} 0 \\ \zeta_x\tau_{xx} + \zeta_y\tau_{xy} + \zeta_z\tau_{xz} \\ \zeta_x\tau_{yx} + \zeta_y\tau_{yy} + \zeta_z\tau_{yz} \\ \zeta_x\tau_{zx} + \zeta_y\tau_{zy} + \zeta_z\tau_{zz} \\ \zeta_x\beta_x + \zeta_y\beta_y + \zeta_z\beta_z \end{bmatrix}, \tag{3.5}$$

The quantities U, V, and W seen in Eq. 3.3, are the contravariant velocities and are defined as,

$$\begin{aligned} U &= \xi_t + \xi_x u + \xi_y v + \xi_z w \\ V &= \eta_t + \eta_x u + \eta_y v + \eta_z w \\ W &= \zeta_t + \zeta_x u + \zeta_y v + \zeta_z w \end{aligned} \tag{3.6}$$

The viscous terms of the preceding equations are defined as follows,

$$\begin{aligned} \tau_{xx} &= \lambda(u_x + v_y + w_z) + 2\mu u_x \\ \tau_{xy} &= \tau_{yx} = \mu(u_y + v_x) \\ \tau_{xz} &= \tau_{zx} = \mu(u_z + w_x) \\ \tau_{yy} &= \lambda(u_x + v_y + w_z) + 2\mu v_y \\ \tau_{yz} &= \tau_{zy} = \mu(v_z + w_y) \\ \tau_{zz} &= \lambda(u_x + v_y + w_z) + 2\mu x_z \end{aligned} \qquad \begin{aligned} \beta_x &= \gamma_k \tfrac{1}{Pr}\partial_x e_I + u\tau_{xx} + v\tau_{xy} + w\tau_{xz} \\ \beta_y &= \gamma_k \tfrac{1}{Pr}\partial_y e_I + u\tau_{yx} + v\tau_{yy} + w\tau_{yz} \\ \beta_z &= \gamma_k \tfrac{1}{Pr}\partial_z e_I + u\tau_{zz} + v\tau_{zy} + w\tau_{zz} \\ e_I &= e\rho^{-1} - 0.5(u^2 + v^2 + w^2) \\ P &= (\gamma - 1)[e - 0.5p(u^2 + v^2 + w^2)] \end{aligned} \tag{3.7}$$

Pressure is defined using the ideal gas law, where γ is the ratio of specific heats, k is the coefficient of thermal conductivity, μ is the dynamic viscosity, and λ is take from the Stokes' hypothesis, defined as $-\frac{2}{3}\mu$. The Jacobian, J, is defined as,

$$J^{-1} = x_\xi y_\eta z_\zeta + x_\zeta y_\xi z_\eta + x_\eta y_\zeta z_\xi - x_\xi y_\zeta z_\eta - x_\eta y_\xi z_\zeta - x_\zeta y_\eta z_\xi \tag{3.8}$$

The transformed derivatives are then obtained by solving those expansions for the ξ, ν, and ζ components. These terms are defined as

$$\begin{aligned}
\xi_x &= J(y_\eta z_\zeta - y_\zeta z_\eta) & \eta_x &= J(z_\xi y_\zeta - y_\xi z_\zeta) \\
\xi_y &= J(z_\eta x_\zeta - x_\eta z_\zeta) & \eta_y &= J(x_\xi z_\zeta - x_\zeta z_\xi) \\
\xi_z &= J(x_\eta y_\zeta - y_\eta x_\eta) & \eta_z &= J(y_\xi x_\zeta - x_\xi y_\zeta) \\
\zeta_x &= J(y_\xi z_\eta - z_\xi y_\eta) & \xi_t &= -x_\tau \xi_x - y_\tau \xi_y - z_t \xi_z \\
\zeta_y &= J(x_\eta z_\xi - x_\xi z_\eta) & \eta_t &= -x_\tau \eta_x - t_\tau \eta_y - z_\tau \eta_z \\
\zeta_z &= J(x_\xi y_\eta - y_\xi x_\eta) & \zeta_t &= -x_\tau \zeta_x - y_\tau \zeta_y - z_\tau \zeta_z
\end{aligned} \tag{3.9}$$

3.1.1 Implicit Form and Time Discretization

Eq. 3.1 can be written in a linearized, implicit form given by [149]

$$\begin{aligned}
&[I + \frac{\Delta t}{(1+\theta)\Delta\tau} + \frac{\Delta t}{(1+\theta)}(\partial_\xi A + \partial_\eta B + \partial_\zeta C)]\Delta q^{n+1,m+1} = \\
&-[(q^{n+1,m} - q^n) - \frac{\theta}{(1+\theta)}\Delta q^n + \frac{\Delta t}{(1+\theta)} RHS^{n+1,m}]
\end{aligned} \tag{3.10}$$

Here $\Delta\tau$ represents pseudo-time, which can be changed locally in the field using local time steps. This form also contains an artificial time term, $\frac{\Delta t}{(1+\theta)\Delta\tau}$, which contains the pseudo time and must converge at each physical time step. This ensures time accuracy. The θ is set to zero for first order time differencing and $\theta = \frac{1}{2}$ for second order time differencing. The viscous and inviscid flux terms seen in Eq. 3.1 are contained withing the RHS term which is defined as follows

$$RHS = \frac{\partial \vec{E}}{\partial \xi} + \frac{\partial \vec{F}}{\partial \eta} + \frac{\partial \vec{G}}{\partial \zeta} \tag{3.11}$$

Eq.3.10 may also be written in the general form $Ax = b$, where A contains the bracketed term on the left-hand side of Eq. 3.10, and bracketed term on the right side is contained in the vector b. The change in the solution vector in the most recent time step is contained in the $\Delta q^{n+1,m+1}$ term where $(n + 1)$ and $(m + 1)$ define the time step and the subiteration respectively and where applicable. Depending on the usage of subiterations and pseudo time, Eq. 3.10 represents either a Newton subiteration or a dual-time stepping algorithm. In either scenario every individual grid is solved implicitly, and the overset boundary conditions are explicitly updated after each subiteration completes. The use of subiteration allows information to be communicated on a global level at each time step which can improve the global convergence [149].

OVERFLOW solves the problem presented in Eq. 3.10 by treating the left- and right-hand sides on an individual basis. The left-hand side solution is detailed here and the right hand side in the next section. The left-hand side can be inverted via a number of procedures. In this study the D3ADI scheme [150] is used to approximately factor the left hand side in space. Exact spatial factorization of the left-hand side of Eq. 3.10 is computationally expensive, the D3ADI scheme reduces this cost by ignoring the factorization error, making it an approximate factorization. Based on work by Pulliam and Chaussee [151], the inviscid flux Jacobians A, B, and C are factored into their eigenvalue representations as

$$\begin{aligned} A &= X_A \Lambda_A X_A^{-1} \\ B &= X_B \Lambda_B X_B^{-1} \\ C &= X_C \Lambda_C X_C^{-1} \end{aligned} \tag{3.12}$$

The left hand side of Eq. 3.10 is then expanded and the eigenvector matrices extracted from the individual terms leaving the following equation.

$$\begin{aligned} X_A[I + \frac{\Delta t}{1+\theta}\partial_\xi \Lambda_A]X_A^{-1} X_B[I + \frac{\Delta t}{1+\theta}\partial_\eta \Lambda_B]X_B^{-1} X_C[I + \frac{\Delta t}{1+\theta}\partial_\zeta \Lambda_C]X_C^{-1} \Delta q^{n+1,m+1} = \\ -[(q^{n+1,m} - q^n) - \frac{\theta}{(1+\theta)}\Delta q^n + \frac{\Delta t}{(1+\theta)} RHS^{n+1,m}] \end{aligned} \tag{3.13}$$

This gives the Diagonal Alternating Direction Implicit scheme [151]. The Diagonalized Diagonal Dominant Alternating Direction Implicit (D3ADI) scheme can then be obtained by diagonalizing the flux Jacobians and factoring Eq. 3.13, and is given as follows

$$
\begin{aligned}
&X_A[I + \frac{\Delta t}{1+\theta}\partial_\xi^u \Lambda_A + X_A^{-1}(D_\eta + D_\zeta)X_A]X_A^{-1}D^{-1} \\
&X_B[I + \frac{\Delta t}{1+\theta}\partial_\eta^u \Lambda_B + X_B^{-1}(D_\xi + D_\zeta)X_B]X_B^{-1}D^{-1} \\
&X_C[I + \frac{\Delta t}{1+\theta}\partial_\zeta^u \Lambda_C + X_C^{-1}(D_\xi + D_\eta)X_A]X_C^{-1}\Delta q^{n+1,m+1} \\
&= -[(q^{n+1,m} - q^n) - \frac{\theta}{(1+\theta)}\Delta q^n + \frac{\Delta t}{(1+\theta)} RHS^{n+1,m}] \qquad (3.14)
\end{aligned}
$$

Here D is a matrix which holds all the diagonal terms from the Eq. 3.13, and ∂^u is a upwind forward/backward differencing operator, the nature of which is determined by the sign of the inviscid eigenvalues Λ.

3.1.2 Flux Calculations

In order to solve the viscous and inviscid flux terms held in the RHS term from the D3ADI scheme, and ultimately the Navier-Stokes equation, OVERFLOW can use one of several approximate Riemann solvers. These solvers are used to communicate the fluxes in the flow field across the various cell interfaces which compose the computational domain. For this work, the Roe flux-differencing scheme [152] was used in conjunction with the WENO5M reconstruction scheme [153]. Data are communicated through the computational domain by the propagation of left and right running waves moving through the computational domain. Localized Riemann problems are solved at each cell interface. The curvilinear Navier-Stokes equation, seen in Eq. 3.1, can be reduced to a single dimension, ξ, and can be written in the form of a hyperbolic conservation law.

$$\partial_t q + \hat{A}\partial_\xi q = 0 \qquad (3.15)$$

In this form $\hat{A}$ is a matrix held constant between two adjacent cells. In the context of the Roe flux differencing scheme specifically this matrix is defined as the Jacobian of the inter-cell fluxes of the conserved variables q. This definition means that $\hat{A}$ represents the local conditions of the individual cell interfaces. The matrix must also satisfy several conditions to ensure it is generates a valid solution to the hyperbolic problem. It must be diagonalizable with real eigenvalues, consistent with the exact flux Jacobian (since this is an approximate solution method), and it must conserve change in the flow field variables across cell interfaces.

$$\hat{A} = Q\Lambda_A Q^{-1} \tag{3.16}$$

These conditions allow $\hat{A}$ to be defined from an eigenvalue problem perspective as seen in Eq. 3.16. In this formation Λ_A is a diagonal matrix composed of the wave speeds of the left and right running waves withing the domain. Q and Q^{-1} are calculated by using special weighted averages of the states to the left and right of the cell interface. The formulae for these weighted averages are shown below.

$$\rho_{RL} = (\rho_R \rho_L)^{1/2} \qquad u_{RL} = \frac{\rho_L^{\frac{1}{2}} u_L + \rho_R^{\frac{1}{2}} u_R}{\rho_L^{\frac{1}{2}} + \rho_R^{\frac{1}{2}}} \qquad h_{0,RL} = \frac{\rho_L^{\frac{1}{2}} h_{0,L} + \rho_R^{\frac{1}{2}} h_{0,R}}{\rho_L^{\frac{1}{2}} + \rho_R^{\frac{1}{2}}} \tag{3.17}$$

The subscripts 'L' and 'R' denote the states just to the left and right sides of a cell interface respectively, and the subscript 'RL' denotes the roe averaged quantity. From these averages the other conserved variables can be calculated using traditional state relations.

$$f_{RL} = \frac{1}{2}[f_R + f_L] - \frac{1}{2}|\tilde{A}|[\hat{q}_R - \hat{q}_L] \tag{3.18}$$

The $\hat{A}$ calculated from the Roe averaged quantities are used conjunction with the left and right states in Eq. 3.18, which is the formal definition of the Roe flux differencing scheme. The final component of the scheme are the fluxes just to the left and right of the cell interface.

The flux reconstruction scheme is a major factor in the accuracy of the predicted solution. The Weighted Essentially Nonoscillatory (WENO) scheme used in this study is of the form discussed by Nichols et al. [153], but applies it to the cell fluxes based on the work by Jiang and Shu [154]. The scheme uses a 5th-order approximation built by combining 3rd order approximations with weighting terms as,

$$f_{j+\frac{1}{2}} = w_0 f^0_{j+\frac{1}{2}} + w_1 f^1_{j+\frac{1}{2}} + w_2 f^2_{j+\frac{1}{2}} \tag{3.19}$$

This calculation is done for both interfaces of each node, with the interfaces being denotes by the subscript $j + \frac{1}{2}$. The third order approximations at the interface are defined as

$$
\begin{aligned}
f^{L0}_{j+\frac{1}{2}} &= \tfrac{1}{3}f_{j-2} - \tfrac{7}{6}f_{j-1} + \tfrac{11}{6}f_i & \qquad f^{R0}_{j+\frac{1}{2}} &= \tfrac{1}{3}f_{j+3} - \tfrac{7}{6}f_{j+2} + \tfrac{11}{6}f_{i+1} \\
f^{L1}_{j+\frac{1}{2}} &= -\tfrac{1}{6}f_{j-1} - \tfrac{5}{6}f_j + \tfrac{1}{3}f_{i+1} & \qquad f^{R1}_{j+\frac{1}{2}} &= -\tfrac{1}{6}f_{j+2} - \tfrac{5}{6}f_{j+1} + \tfrac{1}{3}f_j \\
f^{L2}_{j+\frac{1}{2}} &= \tfrac{1}{3}f_j - \tfrac{5}{6}f_{j+1} - \tfrac{1}{6}f_{i+2} & \qquad f^{R2}_{j+\frac{1}{2}} &= \tfrac{1}{3}f_{j+1} - \tfrac{5}{6}f_j - \tfrac{1}{6}f_{j-1}
\end{aligned}
\tag{3.20}
$$

With the superscript denoting left or right side. The weights of each approximation are determined by first calculating a ’smoothness indicator’ for the flow region in question. These indicators are as follows for the left and right sides respectively

$$
\begin{aligned}
\beta^L_0 &= \tfrac{13}{12}(f_{j-2} - 2f_{j-1} + f_j)^2 + \tfrac{1}{4}(f_{j-2} - 4f_{j-1} + 3f_j)^2 \\
\beta^L_1 &= \tfrac{13}{12}(f_{j-1} - 2f_j + f_{j+1})^2 + \tfrac{1}{4}(f_{i-1} - f_{i+1})^2 \\
\beta^L_2 &= \tfrac{13}{12}(q_j - 2q_{j+1} + q_{j+2})^2 + \tfrac{1}{4}(3q_j - 4q_{j+1} + f_{j+2})^2 \\
\beta^R_0 &= \tfrac{13}{12}(f_{j+3} - 2f_{j-+2} + f_{j+1})^2 + \tfrac{1}{4}(f_{j+3} - 4f_{j+2} + 3f_{j+1})^2 \\
\beta^R_1 &= \tfrac{13}{12}(f_{j+2} - 2f_{j+1} + f_j)^2 + \tfrac{1}{4}(f_{i+2} - f_i)^2 \\
\beta^R_2 &= \tfrac{13}{12}(f_{j+1} - 2f_j + f_{j-1})^2 + \tfrac{1}{4}(3q_{j+!} - 4q_j + f_{j-1})^2
\end{aligned}
\tag{3.21}
$$

The smoothness indicator is designed in such a way that if any of the third order approximation produce large or spurious variation in the predicted flow, the contributions from that approximation are minimized. The smoothness indicators are then Incorporated into a modified weight, calculated shown in Eq. 3.22.

$$
\tilde{w}_k = \frac{\gamma_k}{(\epsilon + \beta_k)^2} \tag{3.22}
$$

In the Eq. 3.22, γ_k is the optimal weight value. These values are 0.1, 0.6, and 0.3 for γ_0, γ_1, and γ_2 respectively. They are the weights associated with a true fifth order approximation and in regions of relatively smooth flow the modified weight will approach the optimal weight [153]. The modified weight is then normalized to create the weighting used in the WENO scheme.

$$
w_k = \frac{\tilde{w}_k}{\sum_{j=0}^{2} \tilde{w}_j} \tag{3.23}
$$

The right and left fluxes from two adjacent cells are then used as the f_L and f_R terms in Eq. 3.18. The Roe averaged flux is then used to update the next cell along the direction of flow, and the process is then repeated in all dimensions across the computational domain.

3.1.3 Turbulence Modeling

Turbulence modeling for this study was handled using a variant of the Spalart-Allmaras eddy viscosity model [155], the SA-neg model [156]. If given positive initial conditions and boundary conditions the original formulation of the SA model permits only positive solutions. However, in cases of large changes in turbulent content over relatively short regions, discrete solutions can sometimes produce negative undershoots. The SA-neg model allows these negative values by setting the eddy viscosity ν_t to zero whenever a negative solution is predicted and using an unaltered SA model on the positive predictions. Both the SA and SA-neg models use of the Boussinesq approximation for eddy viscosity

$$\nu_t = \tilde{\nu} f_{v1}, \quad f_{v1} = \frac{\chi^3}{\chi^3 + c_{v1}^3}, \quad \chi \equiv \frac{\tilde{\nu}}{\nu} \tag{3.24}$$

Here ν is the kinematic viscosity, χ is the turbulent Reynolds number, and $\tilde{\nu}$ is the working variable of the SA model which is solved for using the following transport equation.

$$\frac{D\tilde{\nu}}{Dt} = c_{b1}(1 - f_{t2})\tilde{S}\tilde{\nu} - (c_{w1} f_w - \frac{c_{b1}}{\kappa^2} f_{t2}) \left(\frac{\tilde{\nu}}{d}\right)^2 + \frac{1}{\sigma}[\nabla \cdot ((\nu + \tilde{\nu})\nabla\tilde{\nu}) + c_{b2}(\nabla\tilde{\nu})^2] \tag{3.25}$$

Here the first two terms of the right-hand side are the turbulence production and destruction terms, respectively. $\tilde{S}$ is the modified vorticity

$$\tilde{S} \equiv S + \frac{\nu}{\kappa^2 d^2} f_{\nu 2}, \quad f_{\nu 2} = 1 - \frac{\chi}{1 + \chi f_{\nu 1}} \tag{3.26}$$

S is vorticity magnitude, d the distance from the closest wall, and f_w defined as the function

$$f_w = g\left(\frac{1 + c_{w3}^6}{g^6 + c_{w3}^6}\right)^{\frac{1}{6}}, \quad g = r + c_{w2}(r^6 - r), \quad r = min\left(\frac{\tilde{\nu}}{\tilde{S}\kappa^2 d^2}, r_{lim}\right) \tag{3.27}$$

The f_{t2} function controls the laminarization of the boundary layer, and can be used to specify exact transitions locations,

$$f_{t2} = c_{t3}\text{exp}(-c_{t4}\chi^2) \tag{3.28}$$

The remaining undefined terms are constants and terms from the transport equation are defined as follows,

$$\begin{aligned}
c_{b1} &= 0.1355 & \sigma &= \tfrac{2}{3} \\
c_{b2} &= 0.622 & \kappa &= 0.41 \\
c_{w1} &= \tfrac{c_{b1}}{\kappa^2} + \tfrac{(1+c_{b2})}{\sigma} & c_{w2} &= 0.3 \\
c_{w3} &= 2 & c_{v1} &= 7.1 \\
c_{t3} &= 1.2 & c_{t4} &= 0.5 \\
r_{lim} &= 10
\end{aligned} \tag{3.29}$$

The fact that the SA model is a linear eddy viscosity model means it does not accurately predict the effects of system rotation on the shear turbulent flow. To correct this issue the rotation curvature (RC) correction devised by Spalart and Shur [157] was also applied in this work. This correction uses an empirical approach to track the principle axes of the strain tensor, which is both Galilean invariant and relatively simple. The application of this correction to the SA-neg model necessitates only one change. The turbulence production term from the original SA model is multiplied by a rotation function given as

$$f_{r1}(r^*, \tilde{r}) = (1 + c_{r1})\frac{2r^*}{1 + r^*}[1 - c_{r3}\tan^{-1}(c_{r2}\tilde{r})] - c_{r1} \tag{3.30}$$

where

$$r^* = \frac{S}{\omega} \tag{3.31}$$

$$\tilde{r} = \frac{2\omega_{ik}S_{jk}}{D^4}\left(\frac{DS_{ij}}{Dt} + (\varepsilon_{imn}S_{jn} + \varepsilon_{jmn}S_{in})\Omega_m\right) \tag{3.32}$$

The tensors and calibration coefficients used here are defined as

$$S_{ij} = \frac{1}{2}\left(\frac{\partial u_i}{\partial x_j} + \frac{\partial u_j}{\partial x_i}\right), \quad \omega_{ij} = \frac{1}{2}\left(\left(\frac{\partial u_i}{\partial x_j} - \frac{\partial u_j}{\partial x_i}\right) + 2\varepsilon_{mji}\Omega_m\right) \tag{3.33}$$

$$S^2 = 2S_{ij}S_{ij}, \quad \omega^2 = 2\omega_{ij}\omega_{ij}, \quad D^2 = \frac{1}{2}(S^2 + \omega^2) \tag{3.34}$$

$$c_{r1} = 1.0, \quad c_{r2} = 12, \quad c_{r3} = 1.0 \tag{3.35}$$

3.1.4 Delayed Detached Eddy Simulation

The dominance of relatively small length scales in rotor hub flow fields required the use of the Delayed Detached Eddy Simulation framework to solve the Navier-Stokes equation. A hybrid RANS/LES system, DDES preserves the RANS solution behavior in attached boundary-layer regions and switches to LES like treatment in regions of separated flow. The switch between treatment model branches is determined by a modified distance function.

$$\tilde{d} \equiv d - f_d max(0, d - C_{DES}\Delta) \tag{3.36}$$

$$f_d \equiv 1 - \tanh([8r_d]^3) \tag{3.37}$$

$$r_d \equiv \frac{\nu_t + \nu}{\sqrt{U_{i,j}U_{i.j}\kappa^2 d^2}} \tag{3.38}$$

Here d is the length scale that appears in the unaltered SA model, $C_{DES} = 0.65$ and Δ is the length of the longest dimension of a specific grid cell. f_d is a special function designed in such a way that $f_d = 1$ in LES regions and r_d is the ratio of the turbulence model length scale to the wall distance. This is altered from the quantity r in the original SA model. ν_t is the eddy viscosity, ν the kinematic viscosity, $U_{i,j}$ are velocity gradients, and κ the Karman constant.

3.2 Hub Geometries and Computational Grids

In this study four unique computational geometries were used. These included a computational model of the full GTWT experimental setup and three free air rotor hub geometries each with varying geometric complexity. All of the geometries used in this study are either recreating or derived from the VLRCOE Phase III Hub, and its surrounding tunnel environment [12, 76]. The Phase III hub is itself based on a reduced scale defeatured model of an industry standard hub originally provided to the VLRCOE efforts by the Sikorsky Aircraft Corporation [74], and is shown in Fig. 3.1 the GTWT experimental installation. Simplifications from a realistic hub were made to the Phase III hub to allow for the experiments to serve as a more canonical test case. The hub model includes swash plate, drive shaft, scissor arms, upper and lower spider plates, and blade shanks. The omitted components of the most significant at this level of geometric simplicity are the pitching links. These components were found to significantly increased the 4/rev harmonic content without affecting the other harmonic content. Additionally their removal was not found to significantly affect the drag effects on the surrounding hub components [11, 74].

As was previously noted this hub geometry has been the subject of multiple experimental and computational studies as part of VLRCOE's Rotor Hub Workshop series. Experimental data collected during this series by Schmitz et al. [76] are used in later parts of this work as validation for the CFD predictions. The original experimental parameters are listed in Table 3.1.

The surface fitted grids and the near body grid systems used in this work were generated and provide by PSU-ARL. These grids were then used to generate surrounding off body grid systems, with several layers of overlap between the two grids systems. Predefined XRAY hole cutters [158] and native OVERFLOW routines were used to facilitate the overset domain connectivity between the near and off body grids in all grid systems. In the overlapping layers the near and off body grids systems have relatively similar resolutions to reduce the overset grid interpolation errors. Modifications to the provided grid systems were made using the Chimera Grid Tools software package [14]. These modifications were limited to deleting certain features from the surface grids and regenerating accompanying off body grids. No features were added to the provided surface grids.

3.2.1 Hub Grid Systems

The first CFD test case used in this work recreated the GTWT setup and featured the tunnel walls, mounting pylon, and full Phase III Baseline hub geometry. This case was used primarily for validation against the experimental results. Unlike the proceeding geometries and simulations the simulation within the modeled tunnel is not a free air simulation but rather and internal flow simulation. There are several inherent traits of OVERFLOW, as a compressible flow solver, that complicate internal flow simulations which will be further addressed in the next chapter. Shown in

Fig. 3.1 Phase III VLRCOE Hub (Taken from [12])

Table 3.1 Phase III VLROCE hub Experimental Parameters

Hub Diameter	0.3408m
Reference Frontal Area	0.0039m^2
Hub Rotational Speed	152 rpm
Flow Velocity	6.5 m/s
Diameter-Based Reynolds number	4.6x10^6
Advanced Ratio	0.2

Fig. 3.2a and Fig. 3.2b are is an x-axis view of the tunnel and hub surface grids and a y-axis view of the internal off body grids, respectively.

The tunnel simulation used a nozzle inlet condition, in which the total conditions and flow direction were specified, and a constant pressure outlet. These conditions were selected to most approximate the experimental conditions as closely as possible. All of the solid surfaces were specified as viscous, no slip walls with the tunnel walls and pylon carrying an additional wall function condition as their near body grid spacing was coarser. The full tunnel geometry contained 142 volume grids and $61\text{x}10^6$ vertices.

The full tunnel geometry was subjected to a defeaturing process. By removing and/or altering certain features and aspects of the geometries their contributions harmonics and aerodynamic characteristics of the hub system can be examined. The first free air hub, hereafter referred to as the Baseline hub, was created by removing the tunnel walls, and mounting pylon. The Baseline hub featured the swash plate, scissor arms, drive shaft, upper and lower spider plates, and blade shanks. None of the geometries were created to feature control systems such as pitch links. The surface grids and off-body grid systems for the Baseline is shown in Fig. 3.3.

The next hub, called the Defeatured Baseline Hub, was created by removing the swashplate, scissor arms, and drive shaft. The removal of the spider arms will be the subject of investigation later on, they represent the only 2-fold rotational symmetry on the hub and thereby carry heavy influence on the harmonic content of both the surface forces and wake. The surface grids for the Defeatured Baseline Hub are shown in Fig. 3.4.

The Low Drag Hub is the final free air hub geometry used in this study. It represent a dramatically different geometry than the previous two hub and was created to represent a next generation, high-speed vehicle rotor hub. The Low Drag Hub features only a lower spider plate, with the upper surface of the hub being altered to resemble a smoothed, faired design. The blade shanks were replaced with the Sikorsky DBLN 526, reverse flow, airfoil, and the shank chord was increased to maintain the same frontal area as the Defeatured Baseline Hub. Given the 5deg angle angle of attack of the DBLN 526 airfoils were inverted so that the advancing blade shanks were at a positive Angle of attack with the incoming flow. A more detailed discussion of this design and the motivation behind it is given by Schmitz et al. [76]. The surface grids from the Low Drag Hub can be seen in Fig. 3.5

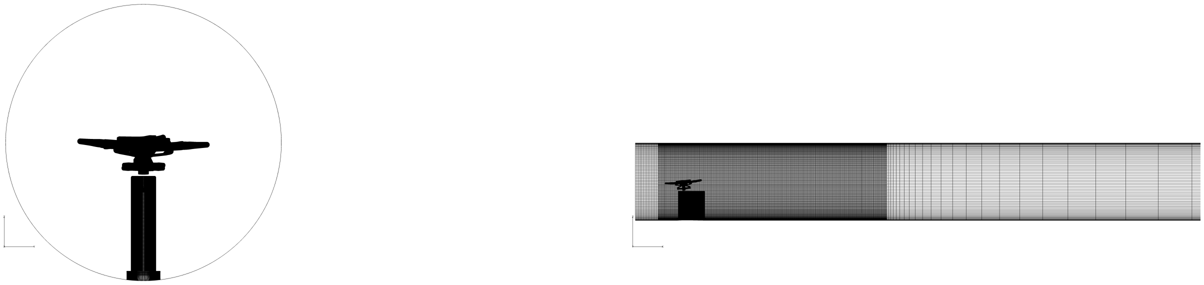
(a) x-axis view Surface Grids **(b)** y-axis view Off-body Grids

Fig. 3.2 Full Tunnel Grids

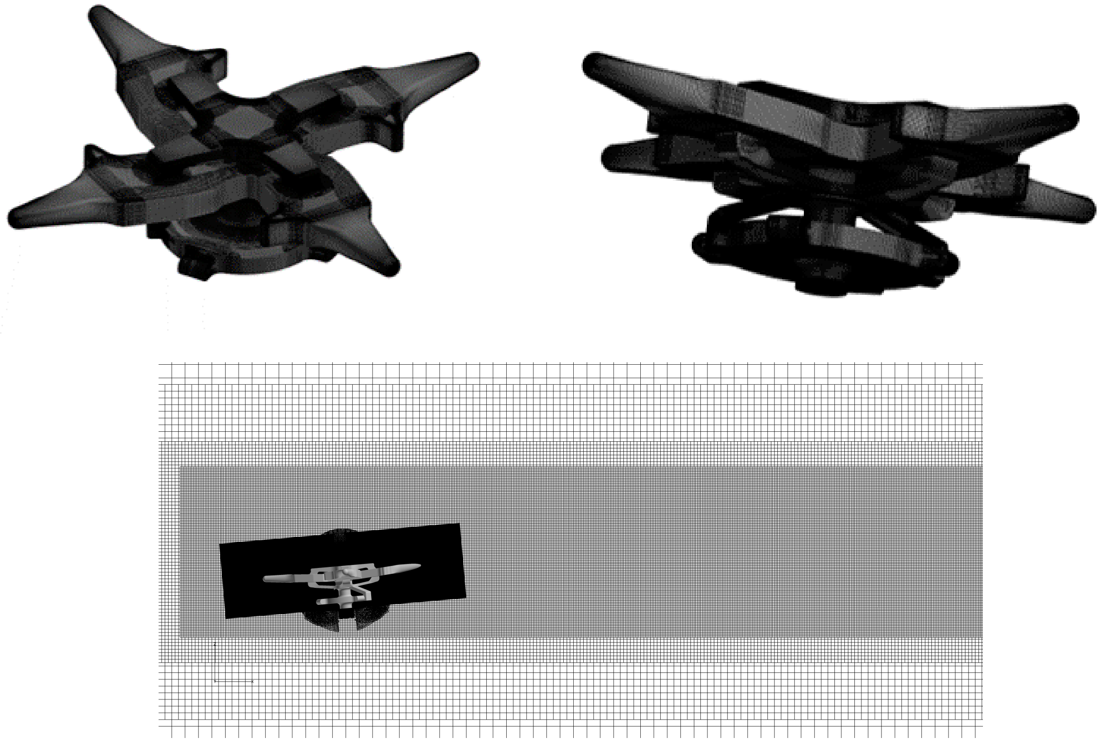
Fig. 3.3 Baseline Hub Grids

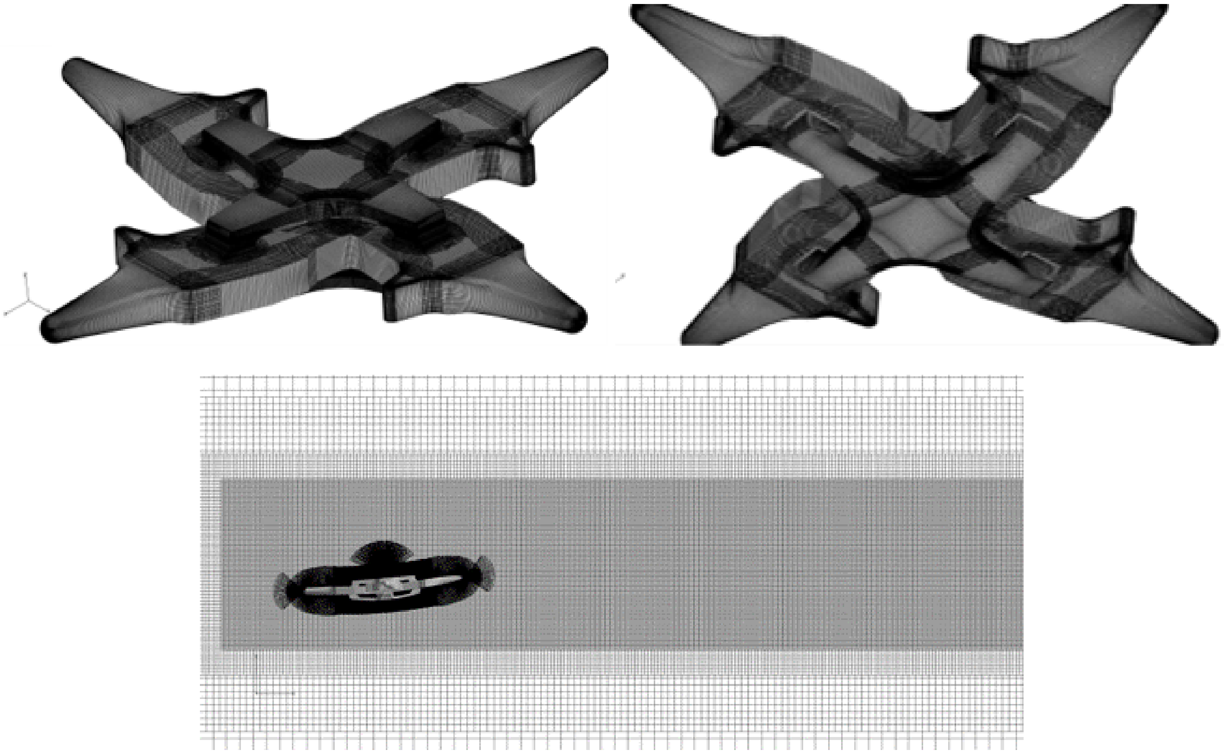

Fig. 3.4 Defeatured Baseline Hub Grids

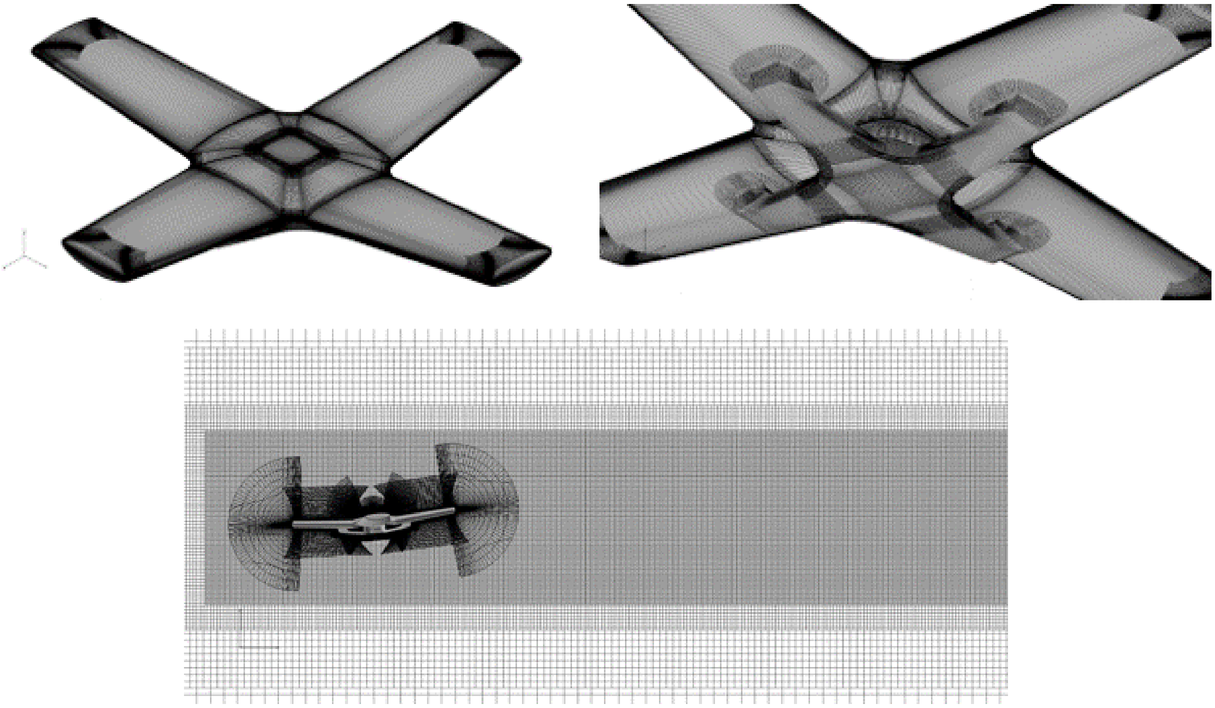

Fig. 3.5 Low Drag Hub Grids

While the surface geometries, and therefore grids, widely vary for each of the three free air hubs the off-body grid generation process was kept the same for each geometry to ensure consistency. For all the hub the nearest off-body grid uses a grid resolution of 0.25” and extends approximately six hub diameters down stream. The number of vertices and total number of volume grids in each hub grid system are compiled in Table 3.2

3.3 Modal Decomposition Methods

Two forms of modal decomposition are implemented in this work using a code base developed at the University of Tennessee in Knoxville by previous members of the Revolutionary Aerodynamics Innovations and Research (VolAIR) group. This was designed to run in parallel and works in three stages. In the first stage individual Plot3d format solution files produced by OVERFLOW are converted and concatenated into a single Hierarchical Data Format version 5 (HDF5) file. The second stage of the code uses this file to carry out the POD or SPOD process, as specified by the user. The user may also specify the numbers of modes, and frequencies if using the SPOD function, which are written into a single HDF5 format output file. The final portion of the code converts this output file into a single Plot3d files if the POD implementation was used. If the SPOD implementation is used, then the output HDF5 file is converted into multiple Plot3d files equal to the number of frequencies specified in the prior step, with each file contained the modes at that frequency. The POD and SPOD functionalities of this code are described in the following section.

3.3.1 Classical POD

All of the methods used in this paper are derived from the classical formulation of POD, which is summarized here based on Taira et al. [115]. The first step of POD in any application is too collect series of instances from some process. In fluid dynamics this is traditionally a vector field, $q(\xi, t)$. Here ξ is any collection of one-, two-, or three- dimensional discrete spatial points, and t the instance in time they were captured at. The ensemble average, $\bar{q}(\xi)$, of this field is then calculated and subtracted, creating a matrix of fluctuating components. This matrix can be decomposed in as shown in Eq.3.39

$$x(t) = q(\xi, t) - \bar{q}(\xi) = \sum_{j} a_j(t)\phi_j(\xi) \tag{3.39}$$

Table 3.2 Flat Plate Lift and Drag Area

Hub	Volume Grids	Total Number of Grid Points
Full Tunnel Simulation	142	$60.1\text{x}10^6$
Baseline Hub	178	$53.7\text{x}10^6$
Defeatured Baseline Hub	137	$35.7\text{x}10^6$
Low Drag Hub	89	$28.5\text{x}10^6$

In this formation, ϕ is a set of orthogonal modes and $a_j(t)$ the corresponding temporal coefficients.

The objective of the POD is to then find the vector set $\phi_j(\xi)$ that best represent $q(\xi)$ in as few modes as possible. This can be accomplished by first defining R as the covariance matrix of $x(t)$ which is defined as,

$$R = \sum_{i=1}^{m} x(t_i)x^T(t_i) = XX^T \in \mathbb{R}^{n\times n} \tag{3.40}$$

Here X is the m number of realization collected into a $n \times m$ matrix. The modes can then be solved for by using an eigenvalue problem of the form

$$R\phi_j = \lambda_j \phi_j \tag{3.41}$$

This will produce a set of eigenvectors $\phi_j(\xi)$ and their associated eigenvalues, λ_j. The eigenvectors correspond to the modes, and their associated eigenvalues indicate how well that mode represents the original data.

The major draw back of this approach however it that R is tied to the number of degrees of spatial freedom in the original data, n. The number of degrees of freedom is equal to the number of grid points multiplied by the number of variables stored at each point, so for all but the coarsest of CFD grids this number is large. This can make the calculation of R computationally expensive for many fluids applications.

3.3.2 Snapshot POD algorithm

In this work the terminology of snapshot POD and POD are used inter-changeably. The algorithm used to calculate the POD modes used here is based on Sirovich's method of snapshots and has been described in other works such as Ref.[159], with the following being drawn from Taira et al. [115]. As was previously noted Sirovich had pointed out that in application to fluid flows the number of spatial grid points, n, was traditional quite large. Sirovich instead proposed the use of the temporal correlation matrix instead of the spatial, as it would yield the same spatially dominant modes but provide a much smaller eigenvalue problem. Sirovich's method, [116] collects a series of snapshots from discrete time levels $t_i = 1, ..., m$ where m is much smaller than the number of grid points n. This method then solves the much smaller eigenvalue problem shown in Eq.3.42

$$X^T X \psi_j = \lambda_j \psi_j, \quad \psi_j \in \mathbb{R}^m, \tag{3.42}$$

Here, $X^T X$ is an $m \times m$ matrix instead of a $n \times n$ matrix, greatly reducing the size of the eigenvalue problem. This reduction in size of the eigenvalue problem is the main draw of the snapshot method. It should be noted that solving the eigenvalue decomposition for XX^T and $X^T X$ produces eigenvectors which are the same as the singular vectors produced by singular value decomposition (SVD), and the eigenvalues produced in this manner are the squares of the singular values. Thus the singular vectors and values can be extracted from snapshot POD and taken as the modes and their associated modal energies, which once again indicate how well the mode matches the original data.

3.3.3 SPOD algorithm

The SPOD algorithm used in this work follows the description of Towne et al. [160]. The first step is to construct a data set Q. This matrix is composed of M vectors representing the instantaneous states of a flow field $q(x, t)$ at equally spaced time internals t_k. These vectors are of length N which is equal to the number of grids points times the number of stored variables. The data matrix is then partitioned into a set of smaller, possibly overlapping blocks as shown in Eq.3.43.

$$Q^{(n)} = [q_1^{(n)}, q_2^{(n)}, ..., q_{N_f}^{(n)}] \in \mathbf{R}^{N \times N_f} \tag{3.43}$$

$$q_k^{(n)} = q_{k+(n-1)(N_f - N_o)} \tag{3.44}$$

In this form the kth entry in the nth block is Eq.3.44, where N_f is the number of snapshots in each of the separated blocks, N_o is the number of overlapping snapshots between blocks, and N_b is the total number of blocks the data set was separated into. Next the Discrete Fourier Transform (DFT) of each block in the data set, $\hat{Q}^{(n)} = [\hat{q}_1^{(n)}, \hat{q}_2^{(n)}, ..., \hat{q}_{N_j}^{(n)}]$ is computed as shown in Eq.3.48

$$\hat{q}_k^{(n)} = \frac{1}{\sqrt{N_f}} \sum_{j=1}^{N_f} w_j q_j^{(n)} e^{-i2\pi(k-1)[(j-1)/N_f]} \tag{3.45}$$

Where k = 1,....,N_f and n = 1,...,N_b. w_j are the modal values of the window function which is used to minimize the spectral leakage caused by the non-periodicity within the data. Here, $\hat{q}_k^{(n)}$ is the Fourier component at the frequency f_k in the nth block and the resolved frequencies are defined by Eq.3.46

$$f_k = \left\{ \begin{array}{l} \frac{k-1}{N_f \Delta t}, \text{for } k \leq N_j/2 \\ \frac{k-1-N_f}{N_f \Delta t}, \text{for } K > N_f/2 \end{array} \right\} \tag{3.46}$$

The cross spectral density tensor $S(x, x', f)$ can then be estimated at f_k by the using Eq.3.47

$$\begin{gathered} S_{fk} = \frac{\Delta t}{sN_b} \sum_{n=1}^{N_b} \hat{q}^{(n)} (\hat{q}_k^{(n)})^* \\ s = \sum_{j=1}^{N_f} w_j^2 \end{gathered} \tag{3.47}$$

A new, more compacted data matrix can then be constructed by rearranging the Fourier coefficients at frequency f_k as shown in Eq.3.48.

$$\hat{Q}_{f_k} = \sqrt{k}[\hat{q}_k^1, \hat{q}_k^2, ..., \hat{q}_k^{(N_b)}] \in \mathbf{R}^{\times N_b} \tag{3.48}$$

This representation allows the cross-spectral density tensor at frequency f_k to be written as in Eq.3.49

$$S_{f_k} = \hat{Q}_{f_k} \hat{Q}^*_{f_k} \tag{3.49}$$

In applications the number of blocks, N_b is generally smaller than the discretized problem, the eigenvalue problem maybe written using Eq.3.49, which results in the form shown in Eq.3.50

$$\begin{gathered} \hat{Q}^*_{f_k} W \hat{Q}_{f_k} \Theta = \frac{\Delta t}{sN_b} \sum_{n=1}^{N_b} \hat{q}^{(n)} (\hat{q}_k^{(n)})^* \\ s = \sum_{j=1}^{N_f} w_j^2 \end{gathered} \tag{3.50}$$

$$\bar{\Psi}_{f_k} = \hat{Q}_{f_k}\Sigma\bar{\Lambda}_{f_k}^{-1/2} \tag{3.51}$$

The eigenvectors associated with non-zero eigenvalues can be recovered using equation Eq.3.51.

In application to the rotor hub flows the chosen ’time intervals’ corresponded to one full revolutions, which included 24 flow fields solutions. A square windowing functions was used in conjunction with an equal weighting coefficient. A 50% overlap was set between each of the data block, which equated to 12 flow field snapshots. As a final note the SPOD code here was implemented in a scalar fashion, i.e. only one variable from the flow filed is considered in the decomposition. Accordingly, streamwise momentum was selected for the decomposition it is a leading indicator of drag and still factors in the streamwise velocity which has been shown to be a key factor in generating accurate modal decomposition results [139].

3.3.4 Space Time POD

The third form of POD applied in this work is called Space-Time POD and is a novel form of POD developed at the University of Tennessee in Knoxville. It is novel in its approach to generating modes that, similar to SPOD are both spatial and temporally coherent, but does not rely on a transformation to Fourier space, and therefor does not assume spectral. As in the other two forms of POD the first step of the process is to gather a ensemble of data from a stochastic process. Like SPOD, Space-Time POD bins the collected data into temporal chunks, in this case full revolutions were used as in SPOD. These data are used to compose a stochastic ensemble Q. As in the SPOD method the ensemble average of Q is calculated and subtract from each entry to create mean-subtracted matrix x, as in Eq.3.39. As in the previous methods this matrix is then subject to a SVD to produce the singular modes and values.

Since vectors of values are stored at each grid points the calculation of the covariance matrix can then result in non-physical units for certain indices. To combat this the matrix X must be pre-conditions with a weighted normalization. The code makes use of a entropy normalization of the form shown in Eq.3.52.

$$S_{ww} = \left[\frac{R}{\rho}, \frac{\rho}{T}, \frac{\rho}{T}, \frac{\rho}{T}, \frac{\rho C_v}{T^2}\right] \tag{3.52}$$

This normalization is a novel one recently developed at the University of Tennessee in Knoxville, but in instances of small temperature fluctuations, such as this case, it is functionally no different than the commonly implemented Chu normalization [161]. After this normalization is applied the decomposition continues in the same manner as the snapshot POD.

Chapter 4: Results

4.1 Results

Each hub case began four revolutions of non-time accurate simulation to advect the start up transients. Then an additional five revolutions of time accurate simulation were conducted to allow convergence, a physical time step corresponding to .25° of hub rotation was selected. Data sampling for all cases began with the tenth revolution. 15 full revolutions were collects for the Full Tunnel case, 20 full revolutions were collected for the Baseline and Defeatured Baseline hubs, and 27 full revolutions were collected for the Low Drag hub. As such all of the free air simulations were run for at least 30 full revolutions of hub flow, with the Low Drag hub run for 37 full revolutions. The surface forces predictions were saved ever 2.5° of azimuthal location and the full flow field solutions every 15° azimuth. The Low Drag hub serves as a good example of the prohibitive size of these hub data sets. Even though it was the least computationally expensive grid the Low Drag hub case, when sampled as described above, yielded a data set over 1 TB in size.

4.1.1 Surface Forces

Due to the manner in which OVERFLOW calculates force coefficients for internal flows, directly comparing the Full Tunnel CFD predictions and the associated experimental results is not directly meaningful. As documented by several works [12, 76, 98] the experimental results make use of measured changes in pressure and flow area to calculate quantities such as streamwise velocity and mass flow rate. These quantities are in turn used to non-dimensionalize the drag coefficient. OVERFLOW relies on the use of nominal free stream conditions specified at the simulated flow inlet to non-dimensionalize the predicted drag coefficients. Since OVERFLOW is a compressible flow solver, the blockage created by the hub and mounting pylon create deviations in the flow from the nominal flow conditions used in the non-dimensionalization. To correct this error, the predicted mass flow rate was used to calculate the effective velocity and dynamic pressure of the simulation, which were then used to correct the predicted drag. This issue, as well as the correction and inlet/outlet conditions used in this work were originally detailed by Coder et al. [98]. The correction results in approximately a 12% increase in the D/q values. This correction need not be applied to any of the free-air results.

The results of the ensemble averaging for each hub, and the experimental results from Schmitz et al. [76] are plotted against azimuthal positions in Fig. 4.1. All the CFD cases, as well as the experimental results showed maximums at the approximately the $0°$, $90°$, $180°$, $270°$, and $360°$ azimuthal positions with some variation between hubs. This is consistent with expectations as these azimuthal positions would present to the larges frontal area to the incoming flow. The full tunnel CFD predictions however showed a 2/rev fluctuation in the magnitude of the predicted drag. At the first and second drag maxima, corresponding roughly to the $90°$ and $270°$ azimuths predicted $D/q \approx$ 64 in^2, while predicting $D/q \approx$ 58 in^2 at the maxima near the $180°$ and $360°$ azimuths. While the scissor arms provide a 2/rev physical feature, this fluctuation was not seen in the free air simulation of the Baseline hub, which also featured the scissor arms. Based on this it sees likely that the 2/rev fluctuation in the full tunnel simulation's predicted drag was caused by some interactional aerodynamics between the scissor arms, providing the 2/rev forcing, and the tunnel walls and/or the mounting pylon. All the other CFD cases, showed self-similar drag maximums at the and minimums with only small difference between each point.

The CFD predictions for the full tunnel show inconsistent agreement with the experimental results. The full tunnel predictions can be seen in initial agreement with the experimental results over the first approximately $30°$ of rotation. The full tunnel ensemble average can then be seen overpredicting the experimental results from approximately $30°$ azimuth to the $150°$ azimuth. At that points the CFD experimental results show agreement again, until approximately the $240°$ azimuth. The CFD predictions then return to overpredicting the experiments for the rest of the rotation. The full tunnel CFD prediction of D/q were on average 9% higher than the experimental results. The amplitude of the fluctuations in D/q can also clearly be seen decreasing across the ensemble averages of the various hubs. The amplitudes of the fluctuations in D/q of the Low Drag

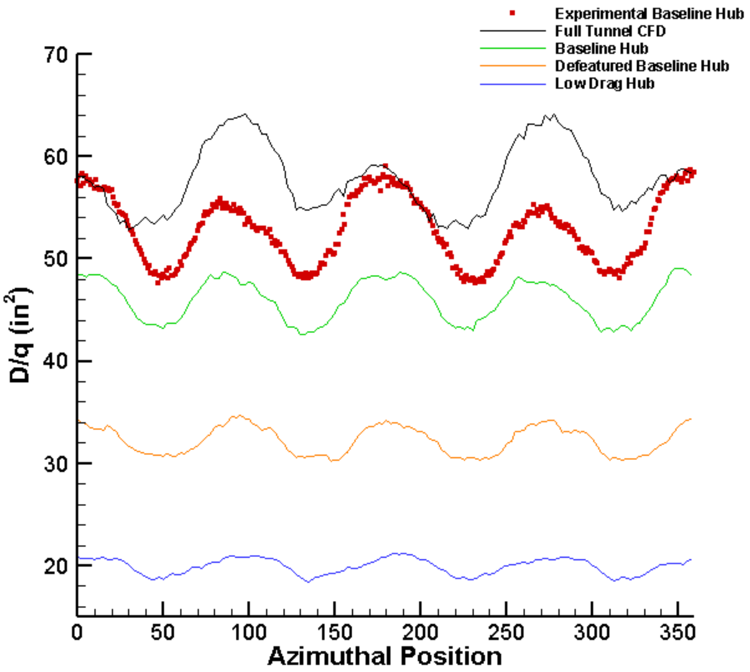

Fig. 4.1 Flat Plate Drag Area Comparison

Hub were approximately 60% of those in the Defeatured Baseline Hub results and 37% of those in the Baseline Hub results.

The change in drag caused by the removal of the tunnel walls and the various geometric components is also of interest. The time averaged D/q and L/q values for each hub variant and the average experimental D/q are given in Table 4.1, and were used to calculate the percent difference in mean D/q between for each hub. An ensemble average of the D/q was calculated for each hub and plotted against azimuthal positions, along with experimental results, shown in Fig. 4.1. The removal of the mounting pylon and tunnel walls for the Baseline Hub CFD predictions resulted in a decrease of 13.85% mean D/q from the experimental results and a 21% decrease from the full tunnel CFD predictions. While this is a relatively small reduction the flow around the mounting pylon would only have interacted with the lower portions of the rotor mast, scissor arms, and swash plate. The Defeatured Baseline and Low Drag hubs show 48.24% and 91.05% reductions in mean D/q from the experimental results, respectively. The drag reduction caused by the removal of the swashplate, rotor mast, and scissor arms was approximately equal to the reduction caused by the streamlining of the blade arm and the removal of the upper spider plate. The Low Drag Hub approximately 60% of the D/q of the Defeatured Baseline Hub, which provides the most similar geometry.

Interestingly, While the Defeatured Baseline hub and Low Drag hub had matching frontal areas the reduction in drag seen between these two hubs is also identical to the difference seen between the Baseline and Defeatured Baseline hub. The removal of the swashplate, rotor mast, and scissor arms caused a reduction of approximately 13.67 in^2 to the flat plate drag area. With these components removed the frontal surface area of the hub system is reduced which is expected to cause a drag reduction given the previous statement. The streamlining and use of the DBLN airfoils caused a reduction of approximately 12.51 in^2. So even while the frontal area was unchanged a non-negligible drag reduction was seen. This indicates that while frontal area has been identified as the leading parameter in hub drag, it is not the only parameter which can be used to reduce hub drag in noticeable quantities.

As a final note, later portion of this work will separate, bin, data based on degrees of azimuthal rotation. This separation can have some bearing on the results of processes such as FFTs or modal decompositions. However, it has little effect ensemble averages. Shown in Fig. 4.2 are the

Table 4.1 Time Averaged Flat Plate Lift and Drag Area

Hub	D/q (in^2)	L/q (in^2)
Experimental Phase III Hub	52.7960	-
Full Tunnel Hub	57.7255	-17.972
Baseline Hub	45.9607	-3.5742
Defeautred Baseline Hub	32.2536	-22.8525
Low Drag Hub	19.9473	-27.4823

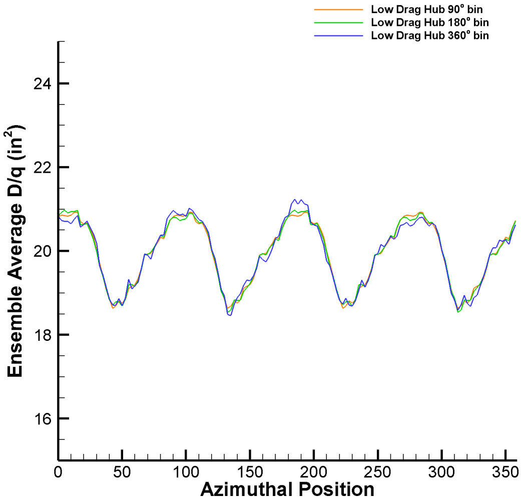

Fig. 4.2 Low Drag Hub D/q Binned Data Comparison

ensemble averages of the flat plate drag area as predicted for the Low Drag Hub. The data were separated into $90°$, $180°$, and $360°$ bins before the averaging. The binning process does alter the number of outcomes, i.e. by using a $90°$ bin the data is separate into chunks each of which only covers $90°$. As the Low Drag Hub is symmetric every $90°$ and $180°$ of rotation the results of those averages are simply copied and concatenated to themselves here so they may be compared to the $360°$ binned data. The D/q measurements presented in Fig. 4.1 were calculated using the $360°$ bins.

4.1.2 Surface Force Harmonics

The harmonics of the CFD predicted surface forces of each hub were found conducting an FFT on time histories of the flat plate areas for the lift and drag. The results of these can be seen in Fig. 4.3a and Fig. 4.3b. At least twenty full revolutions of data were used for each hub, with each individual revolution providing a window for the FFT. All of the hub flows are clearly dominated by 4/rev content. Both the Defeatured Baseline Hub and Low Drag Hub have 4-fold rotational symmetry so a dominant 4/rev frequency in their surface forces is expected. In the case of the Baseline, the scissor arms have a 2-fold rotational symmetry; however both the collection of upper components and the swash plate are still 4-fold symmetric, and compose a large portion of the surface area of that geometry. Given this mixture of symmetries the still dominant 4/rev content is not surprising, and the increased 2/rev content in the Baseline Hub surface forces was expected. The Low Drag hub also exhibited high 8/rev and 12/rev frequency content in the flat plate lift area statistics.

The results of the FFT of the Baseline Hub surface forces are similar in magnitude and behavior to results obtained by Coder [99]. However, in that study the Baseline Hub was modeled so as to include the mounting pylon. In that study it was theorized that either dynamical instabilities arising at one half of the dominant flow frequency or the presence of the scissor arms as a 2/rev geometric symmetry was the cause of the increase in the 2/rev content. As all of these hubs show the 4/rev to be the clearly dominant frequency, it seems unlikely that dynamical instabilities could explain this phenomenon. Any instabilities based on the dominant frequency which could have caused the Baseline Hub's high 2/rev content should also have manifested in the other hub's harmonics.

Based on that the scissor arms seem a more probable cause of the 2/rev content. While the scissor arms account for a relatively small amount of the Baseline Hub's surface area, they were

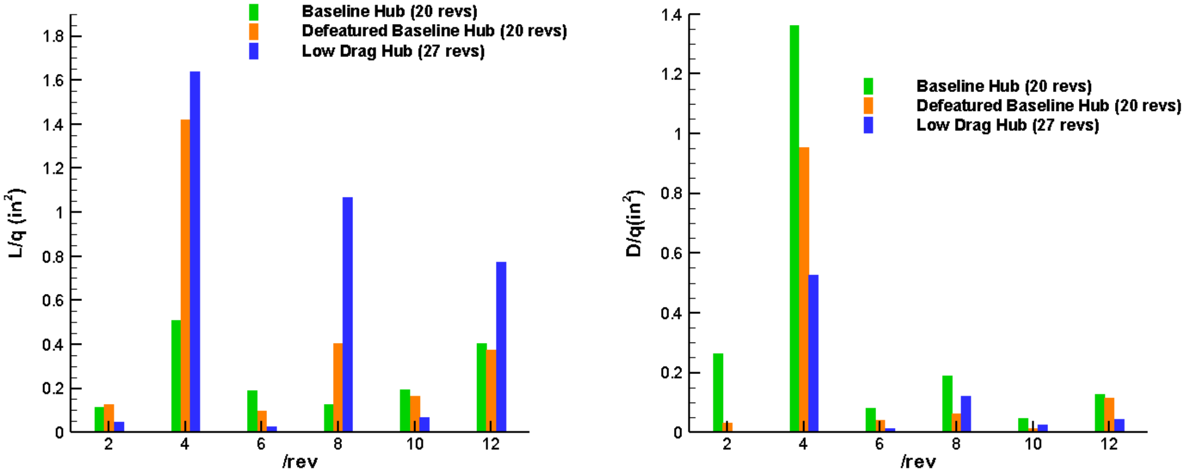

(a) Flat Plate Lift Area **(b)** Flat Plate Drag Area

Fig. 4.3 FFT of Hub Flat Plate Areas found to create strong aerodynamic interactions with the lower spider plate and blades arms. Shown in Fig. 4.4 are Q-criterion isosurfaces colored vorticity magnitude around the advancing scissor arm at the point where it is moving directly into the incoming flow. The wake from the advancing scissor arm, lower spider plate, and blade arms merge, creating a region of high vorticity in direct contact with a sizeable area of the rotor hub. This interaction would peak in intensity twice a revolution when the scissor arms reach their most forward-facing position and could be strong enough to cause the increase in 2/rev content. Considering the presences of this strong interaction between the flows around each of the hub components it seems reasonable to conclude that scissor arms are the culprit for the increase harmonic content.

It must be noted, however, that the strength of the 2/rev content was seen to decrease with increased simulation time. This decrease was first noted when FFT results using the first 15 revolutions of data from the Baseline hub were compared to the results of an FFT incorporating the full 20 revs. Shown in Fig. 4.5 are the results of FFTs of the lift and drag harmonics using 15 full revolutions and 20 full revolutions. The FFT including 15 revolutions shows a 2/rev content that is least half of the 4/rev content in both lift and drag. When 20 revolutions are included the 2/rev content in both lift and drag drops to closer to a quarter of the 4/rev harmonics.

In examining the higher frequencies varying effects are seen. The lifting harmonics show a greatly reduced 6/rev content between the two FFTs. The 8/rev, 10/rev, and 12/rev frequencies also see reductions but are small when compared to the 2/rev and 6/rev reductions. In the drag results, both the 6/rev and 10/rev frequencies experienced significant reduction between the 15 and 20 revolution FFTs. The 8/rev frequency saw a slight decrease, while the 12/rev content actually saw a slight increase.

To further investigate this decrease FFTs were conducted using 8, 10, 12, 15, 17, and 20 full revolutions. Plotted in Fig. 4.6 are the 2/rev frequency contents for each set of revolutions for both lift and drag. In examining the drag harmonics, a small decrease can as the number of included revolutions is increase from 8 to 12. As the number of included revolutions is increased from 12 to 20, the 2/rev content's magnitude decrease more dramatically. The slope from 17 to 20 included revolutions is slightly increased from the slope between 12 and 17 revolutions. Examining the lift results the same dramatic decrease can be seen as the number of revolutions included is increased from 12 to 20, with the same increase in slope from 17 to 20. However, the lift harmonics actually

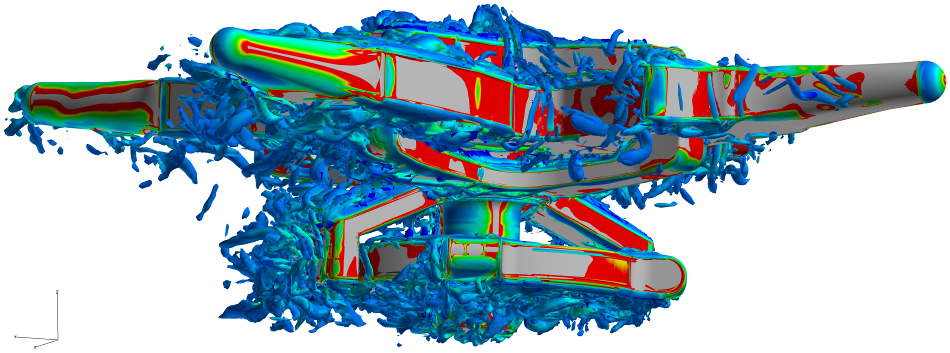

Fig. 4.4 Scissor Arm Interactional Aerodynamics

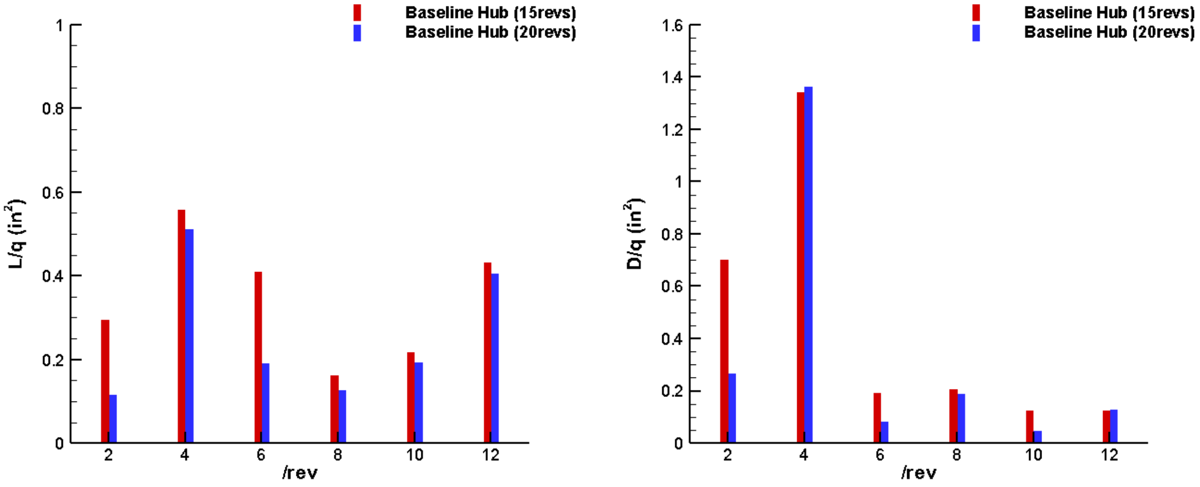

(a) Lift FFT

(b) Drag FFT

Fig. 4.5 Baseline Hub Wake FFT Comparisons

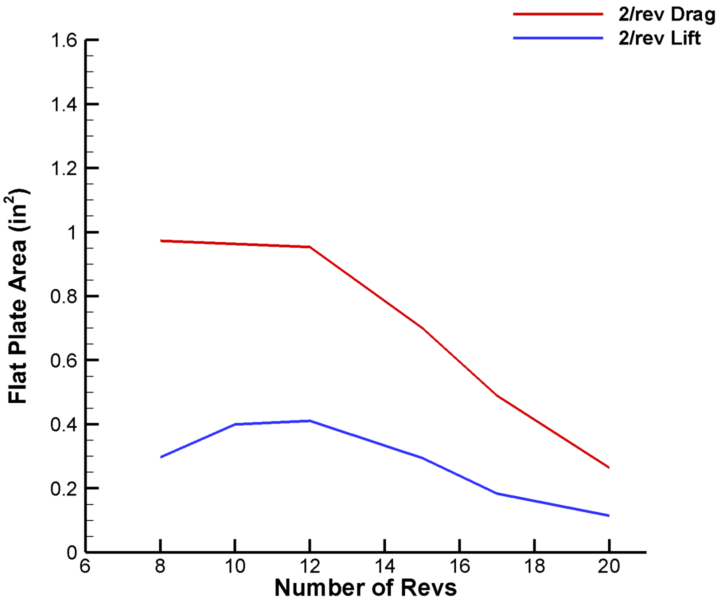

Fig. 4.6 Magnitude of Baseline Hub 2/rev Content

show an increased 2/rev content when the number of included revolutions is increased from 8 to 12.

This decreased 2/rev content can also be seen in the ensemble average of the flat plate drag areas as the number of revolutions included in the ensemble process. Shown in Fig. 4.7 are the ensemble averages using the same number of revolutions as the previous FFT comparisons. At approximately the 0° and 180° azimuths, which correspond to the 2/rev frequency, average decreases as the number of included revolutions is increased. This behavior is not seen in the peeks at the approximate 90° and 270° azimuth locations.

The Baseline hub data set is composed 20 full revolutions, the sampling of which began with the 10th simulated revolutions. At 29 revolutions these CFD predictions are more extensive than is traditionally considered in the case of rotor hubs. The decreasing 2/rev harmonics and the inconsistent high frequency harmonics would seem to indicate that even at this extensive simulation time the harmonics have not converged. The slight difference seen between the use of lower numbers of revolutions in the drag harmonics may have served to obscure this non-convergence in previous studies where smaller sets of revolutions were considered. For example, Hill et al [162] and Potsdam et al. [163] simulated only three hub revolutions for statistical convergence and studies such as Ref. [23, 98, 99] considered only two or three full revolutions in post processing analysis. The ensemble average reflected this however the magnitude of the predicted draft saw small changes based on the included revolutions. This indicates that studies considering the wake harmonics may need to consider data sets collected after 30 or more full revolutions, with lower numbers of revolutions still suitable for force predictions.

4.1.3 Surface Force POD

While reduced order models for hub drag measurements already exist, such as the BEM/frontal area model [76], POD was also applied to the collected hub surface forces. The motivation of this application is not in creating a reduced order model for the surface forces but to investigate if any coherent behavior exists in the perturbations about mean forces as predicted by CFD. To that end mean subtracted POD was applied to the lift and drag force histories for the hubs.

The data for the Defeatured Baseline Hub and Low Drag Hub were placed into 90°, 180°, and 360° bins to examine if the noted harmonics effects the decomposition. The data for the Baseline

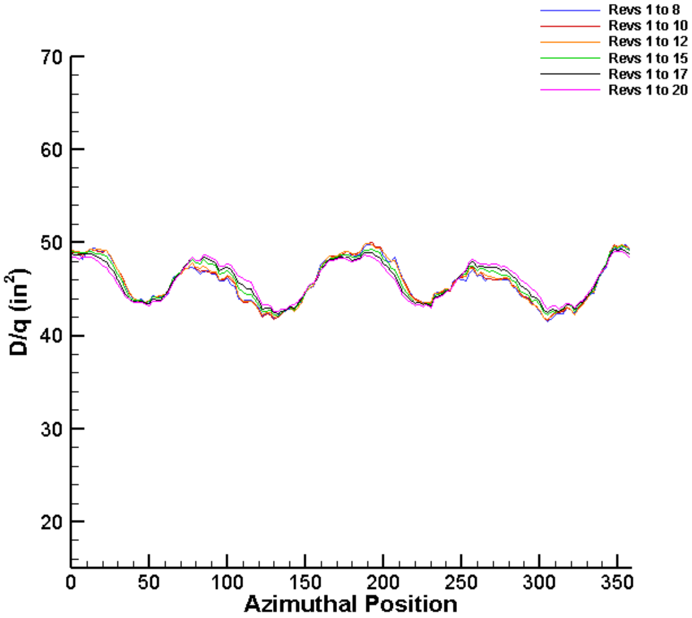

Fig. 4.7 Baseline Hub Ensemble Average Comparison

Hub however were only placed into 180 and 360 degree bins, since the scissor arms prevent it from having 4-fold rotational symmetry. Mean-subtracted POD was then carried out across the bins of each set in order to isolate and analyze any mean behavior.

The percent of modal energy contained in each mode was extracted from the binned drag data and is shown in Fig. 4.8, for the three hubs. All the hubs show a relatively even decay in modal energy as mode number increases. The different sized bins also seem to have a clear effect on the distributions of modal energy, with the $360°$ bins displaying higher amounts of modal energy at all mode numbers than the $180°$ or $90°$ bins. The Baseline Hub displays the highest first mode percent energy of the three, followed by the Defeatured Baseline Hub, with the Low Drag Hub showing the lowest first mode energy and the most even distributions of modal energy.

Even though all the hubs displayed 1st modes with a higher energy than the subsequent modes the distribution is still comparatively even. The mode shapes for the first mode of each hub was also examined to reveal if there were strong mean behaviors in the perturbations of the surface forces. All of the mode shapes for each hub were erratic and showed little repetition or periodic behavior. While this erratic behavior could be caused by poor convergence is the data that seems unlikely. As a comparison non-mean-subtracted POD was conducted on the surface forces. The 1st mode energies of the non-mean-subtract POD are shown compared to the 1st mode energies of the mean-subtracted POD for the Low Drag Hub in Fig. 4.9a. The Low Drag hub first mode shapes for the mean subtracted and non-mean subtracted POD of the flat plate drag area are shown in Fig. 4.9b. As the surface forces did show a strong average behavior, which is captured by the ensemble averaging, the non-mean subtracted POD can identify that behavior results in a higher energy 1st mode followed by relatively low energy successive modes. This clearly contrasts the modal energy distributions seen in the mean subtracted POD of the same quantity. The 1st mode shape of the non-mean subtracted POD displays low frequency consistent shape resembling a reduced magnitude version of the fluctuations in surface forces seen in the ensemble average. By contrast the shape of the first mode from the mean subtracted POD shows a high frequency, erratically fluctuating behavior. In light of their gradual modal energy distributions and lack of discernible coherence in the mode shapes it can be concluded that there are simply no identifiable mean behaviors in the perturbations about the mean surface forces as predicted by OVERFLOW.

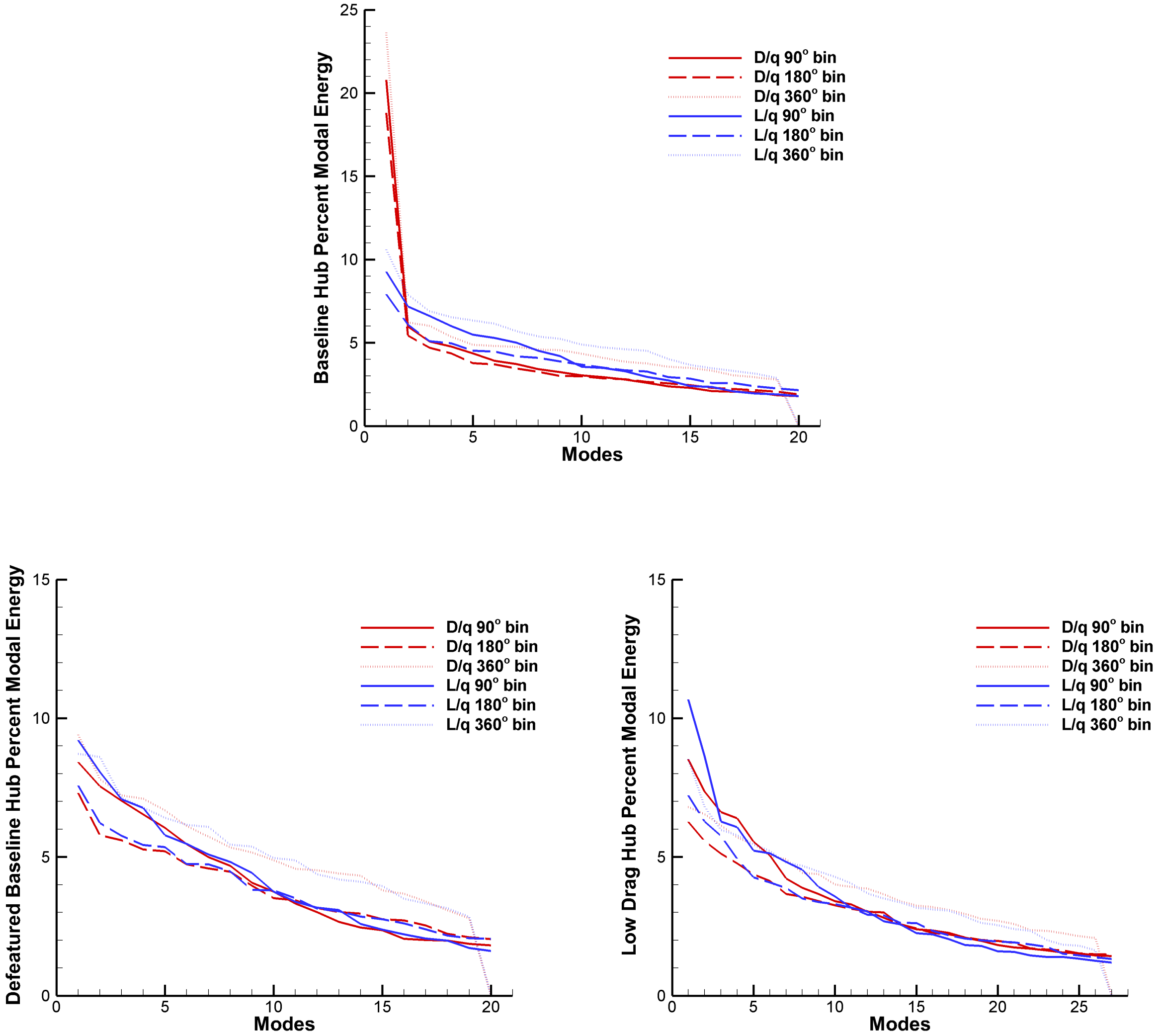

Fig. 4.8 Modal Energy Distribution for the Flat Plate Drag Area of each Hub

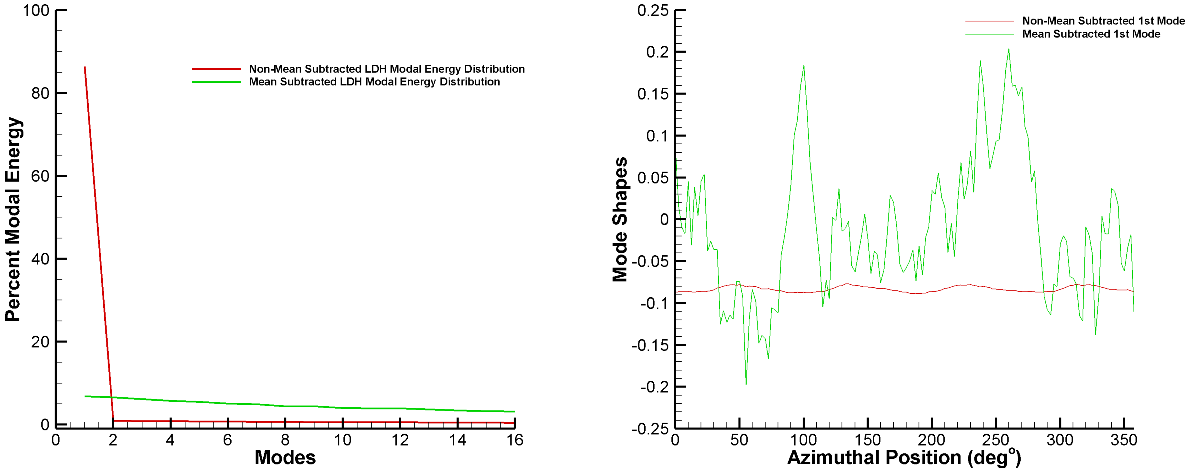

(a) Modal Energy Distribution

(b) 1st Mode Shape

Fig. 4.9 Non-Mean Subtracted POD vs Mean Subtracted POD

4.1.4 Flow Fields and Ensemble Averages

The hub flow wake formations which illustrated by the isosurfaces of vorticity magnitude colored by velocity can be seen along with the ensemble average of the streamwise momentum for the Baseline, Defeatured Baseline, and Low Drag Hubs Fig. 4.10-4.12, respectively. All of the hubs are shown here in the zero degrees azimuthal position, with the z-plane and y-plane views of the ensemble average shown at the $Y = 0$ and $Z = 0$ planes respectively. With regards to the ensemble averaging process it should be noted that each azimuth was weighted equally and streamwise momentum was selected as it is one of the primary indicators of drag. While only the ensemble averages for the zero degree azimuth are presented here, ensemble averages were calculated for each of the unique azimuths of each hub.

In examining the z-plane and y-plane views of the wake of the Baseline hub, shown in Fig. 4.10a and 4.10b, the vortical, separated nature of this flow is clear to see. A periodic shedding can be seen in the wake behind the retreating blade arm and remains coherent for the approximately four hub diameters of captured distance. At approximately the same downstream locations, 1 hub diameter, slight deformation in the wake profile along the upper edge of the wake can be seen as well. Similar fluctuations in the y-plane ensemble average can be seen in the same location. These eddies appear to be released at the frequency of the blade passage and then migrate downstream. However, aside from that shedding very little is visually discernible in these wakes.

The Defeatured Baseline hub wake, shown in Fig. 4.11a & 4.11b, the z-plane profile actually appears quite similar to that of the Baseline Hub. This makes physical sense as the Defeatured Baseline hub is simply the upper portion of the Baseline Hub. The same periodic shedding off of the retreating arm can be seen but are diminished in size. The vortical content of the wake can also be seen to begin thinning two to three hub diameters into the wake, which was not the case for the Baseline Hub.

Dissimilar to the previous two hubs, the Low Drag hub wake, seen in Fig. 4.12a & 4.12b, shows visibly more coherent behavior. Tip vortices can be seen forming and shedding off of both the advancing and retreating blade arms. The same periodic vortex shedding off the retreating arms in the other two hubs is present in the Low Drag hub as well be even more well defined. As another note, a coherent column of vortical content can be seen just above the centerline of the z-plane, at

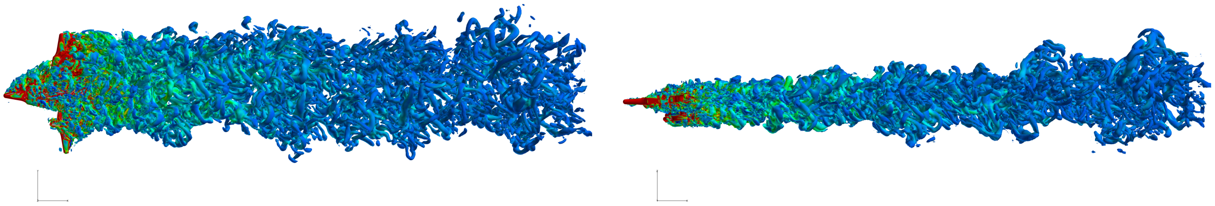

(a) Baseline Hub Wake Top **(b)** Baseline Hub Ensemble Average

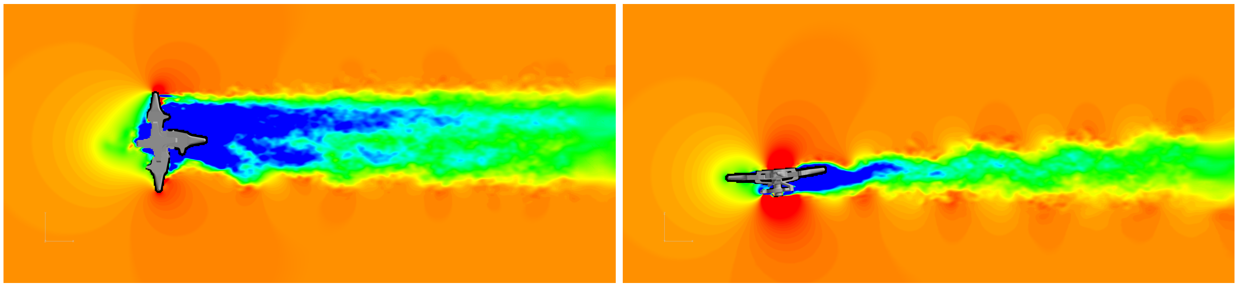

(c) Baseline Hub Wake Side **(d)** Baseline Hub Ensemble Average

Fig. 4.10 Baseline Hub Wake and Ensemble Average of Streamwise Momentum

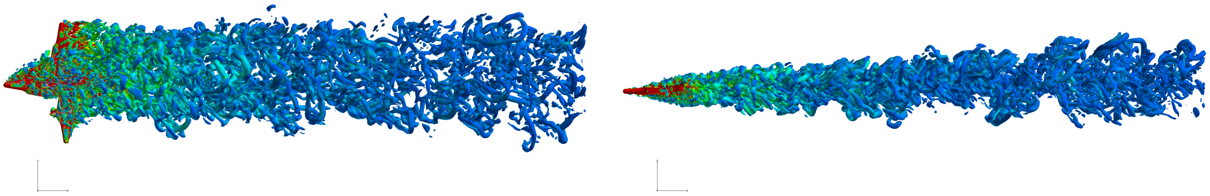

(a) Defeatured Baseline Hub Wake **(b)** Defeatured Baseline Hub Wake

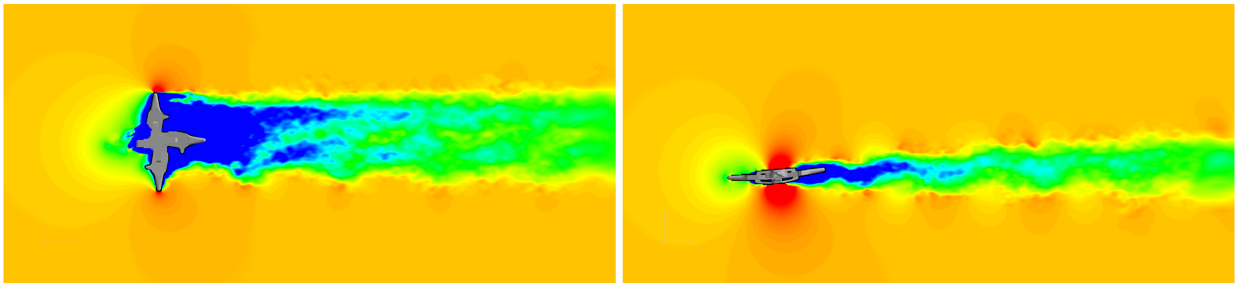

(c) Defeatured Baseline Hub Wake Ensemble Average **(d)** Defeatured Baseline Hub Ensemble Average

Fig. 4.11 Defeatured Baseline Hub Wake and Ensemble Average of Streamwise Momentum

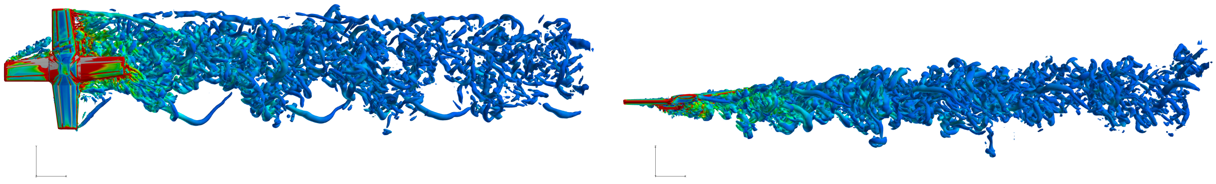

(a) Low Drag Hub Wake Top **(b)** Low Drag Hub Ensemble Average

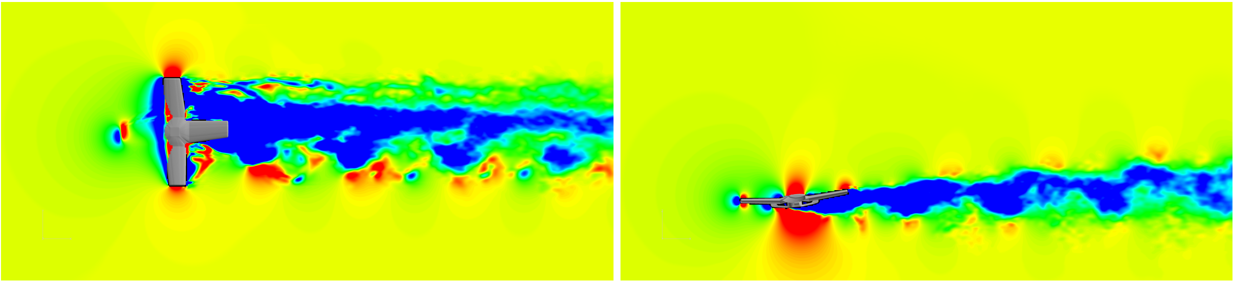

(c) Low Drag Hub Wake Side **(d)** Low Drag Hub Ensemble Average

Fig. 4.12 Low Drag Hub Wake and Ensemble Average of Streamwise Momentum the root of the advancing arm. This structure seems unperturbed by the tip vortices or the blade shank vortex shedding, and was seen in at all observed azimuthal positions for the Low Drag hub. In looking at the y-plane the upper edge of the wake is much flatter than in the prior two cases which can be attributed to the removal of the upper spider plate and hub streamlining. Similar to the Defeatured Baseline hub, visual inspection of lower edge of wake yields little in the way of coherent structures, but the Low Drag hub demonstrates a stronger downwash, creating large vertical eddies in its wake. The more coherent structures and stronger downwash present this wake can no doubt be attributed to the aerodynamic optimization of the hub itself. This more coherent wake should serve to further reinforce the findings of the surface force comparisons. Demonstrating that while frontal area has been shown to be a leading parameter in hub drag it is not the only one with the ability to strongly effect both hub drag and the structure of the hub wake.

The ensemble averages of the streamwise momentum presented in Fig. 4.10 - 4.12 serve to reveal some of the underlying features of these wakes. For this process the ensemble average of each unique azimuthal position for the three hubs was calculated with each azimuth weighted equally. Using 15° steps to collect wake data means that the Defeatured Baseline and Low Drag hub have six unique azimuths, and the Baseline hub has twelves unique azimuths. In examining the ensemble averages of streamwise momentum for the Baseline Hub several large momentum deficits are noticeable. In the top-down view of the ensemble average shown in Fig. 4.10c, regions of large momentum deficits can be seen in the same location as the structures being shed off of the retreating blade are. In addition, a small deficit in streamwise momentum can be seen at the tip if the advancing blade arm. The largest momentum deficit can clearly be seen forming behind the root and first half of the advancing arm, which the wake visuals showed to be areas dominated by highly vortical separated content.

Shown in Fig. 4.11c is the z-plane view of the ensemble average of streamwise momentum for the Defeatured Baseline hub. As in the wake visualization the Defeatured Baseline hub showed very similar behavior to the Baseline hubs. Momentum deficits can be seen in the wake of the retreating arms, a small deficit can again be seen at the top of the advancing arm, and another large deficit is seen in the wake of the advancing arm.

The ensemble average of streamwise momentum for the Low Drag hub is shown in Fig. 4.12c & 4.12d. As was the case for the other two hubs large momentum deficits can be seen in the same spatial locations are the areas of high vortical content in the wake visuals. However, the large deficit behind the root of the advancing blade arm was shifted closer to the center of the hub. This hub also showed more substantial fluctuations in the Y-axis momentum deficits, with the y-plane view of the ensemble average of streamwise momentum for the Low Drag hub being show in Fig. 4.12d.

4.2 Orthogonal Decompositions

Three distinct forms of modal decompositions were applied to the CFD predictions for each of the hubs, POD, mean-subtracted Space Time POD, and mean-subtracted SPOD. The main goal of this application was to investigate the abilities of these decompositions for uncovering underlying coherent or average behaviors which the wave visualizations and ensemble averages fail to discover. The modal energy distributions are examined for one or few high percent modal energies as these serve as one indicator of an strong average behavior captured in the decomposition. The spatial shapes of the highest energy modes were then examined as well. The ensemble averages streamwise momentum was used in the decomposition. As the most traditional form of the model decomposition in the context of fluid dynamic the snapshot POD will be discussed first.

4.2.1 snapshot Proper Orthogonal Decomposition

The percent modal energies for each of the three hubs can be seen in Fig. 4.13. As each instance of captured data was treated as one of the stochastic realizations for the POD the number of modes corresponds to the number of instances, i.e. the 20-revolution set were composed of 480 files so the decompositions of those sets produced 480 modes. Since more revolutions of data were captured for the Low Drag hub, it possesses more modes than the other two hubs. As only the first 8 or so modes captured more than a 1% of the modal energy, the later modes are not shown in the figures to reduce visual clutter. For each hub, the first mode is more energetic than the subsequent modes, but not by a significant portion. In the case of the Baseline hub's energy distribution the first mode contains approximately 15.9% of the total modal energy with the next two most energetic modes containing 2.9% and 2.8% respectively. The Defeatured Baseline hub's first mode captured 17.2% of the modal energy, with the second and third modes both capturing approximately 2.8%. In the

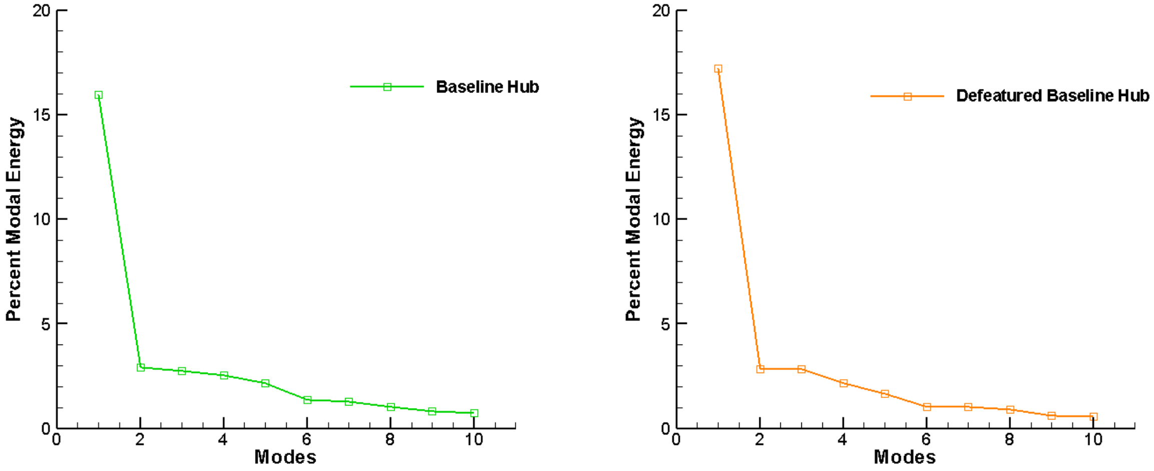

(a) Baseline Hub **(b)** Defeatured Baseline Hub

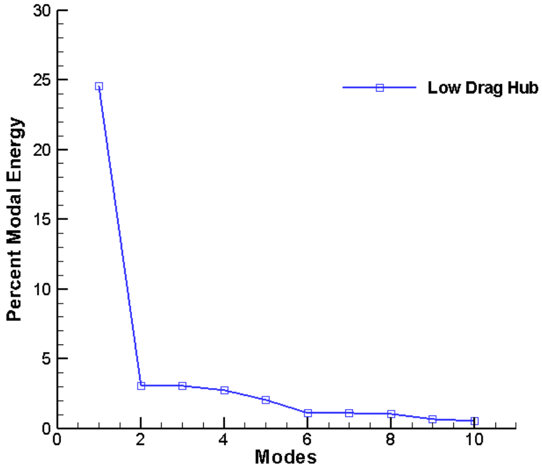

(c) Low Drag Hub

Fig. 4.13 Space-Only Percent Modal Energy Distribution context of creating a reduced order model from these results, approximately 80% of the modes would need to be incorporated to capture 90% of the total modal energy.

The energy distribution from the Low Drag hub is shown in Fig. 4.13c. The Low Drag hub showed 25% modal energy in the most energetic mode, but then shows a relatively similar distribution of energy in the subsequent modes with the second and third containing approximately 3% apiece. For the Low Drag Hub, approximately 75% of the modes would be needed to capture 90% of the modal energy.

To further examine the results of the decompositions the spatial shapes of the highest energy snapshot POD mode for each hub can be seen in Fig. 4.14. In the case of the Baseline and Defeatured Baseline hubs two distinctive structures can be seen forming in the wake of the hub. These structures are spatial collocated with the large deficits in streamwise momentum observed in the wake of the earlier ensemble average the same quantity. Similarly three distinctive structures were seen in the wake of the Low Drag hub, which were again collocated with the large deficits in streamwise momentum. This collocation with the ensemble average indicates that the 1st snapshot POD mode is expected as the 1st mode of a non-mean subtracted snapshot POD is driven towards the most average behavior of the data set.

The second most energetic snapshot POD mode for each hub shown in Fig. 4.15. This mode would represent the next most average behavior of streamwise momentum in the hub wake flows. As it can clearly be seen these modes do not possess any sort of coherence or pattern withing them. This simply indicates that the ensemble average of the wake is the best representation of its mean behavior with no other spatial coherent or repetitious behaviors being present.

4.2.2 Spectral Proper Orthogonal Decomposition

The SPOD methodology applied here is similar to the that applied by Coder [99], which was based on Towne et al. [160]. As opposed to traditional snapshot POD which uses a series of temporal snapshots as the basis for a Singular Value Decomposition (SVD), the SPOD methodology uses a series of fixed width Fourier series windows as the basis for a SVD. Whereas traditional POD is only spatially correlated, the SPOD process allows for the generation of modes that are both spatially and temporally correlated. In this application, the FFT window width was specified as one complete revolution, composed of twenty-four flow field realizations each separated by the

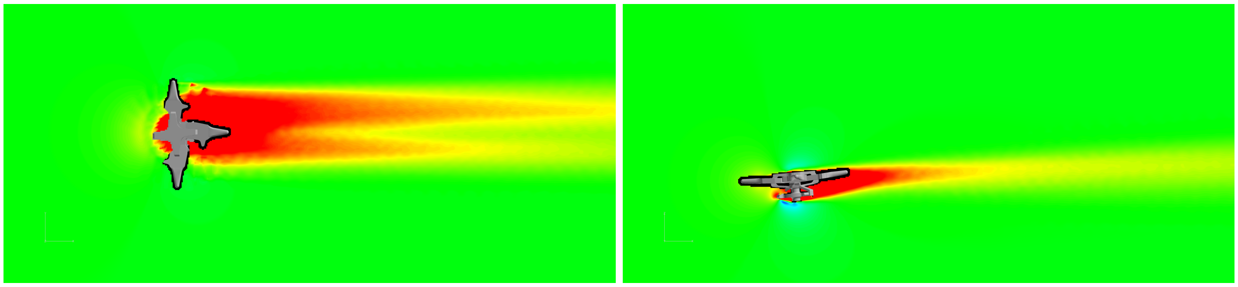

(a) Baseline Hub **(b)** Baseline Hub

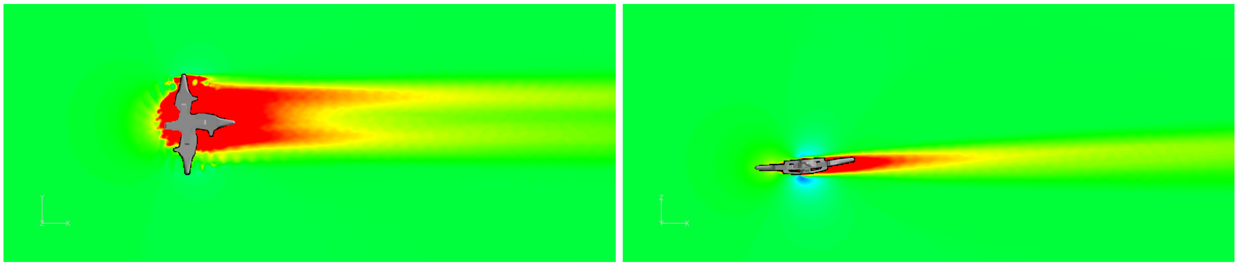

(c) Defeatured Baseline Hub **(d)** Defeatured Baseline Hub

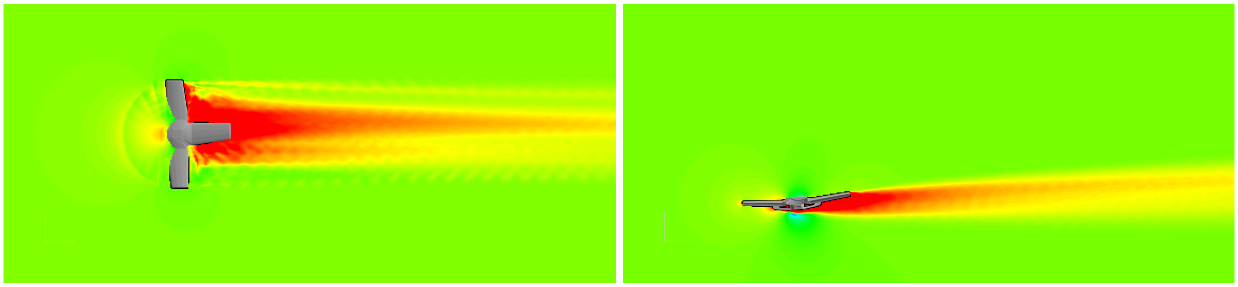

(e) Low Drag Hub **(f)** Low Drag Hub

Fig. 4.14 Spatial Shape of the Highest Energy POD Mode

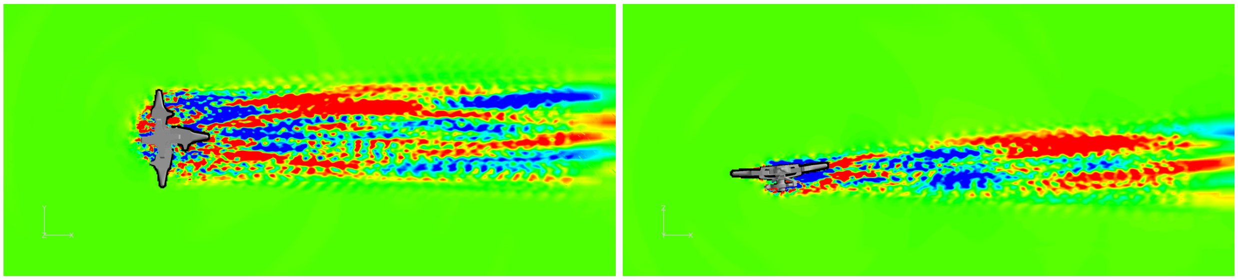

(a) Baseline Hub **(b)** Baseline Hub

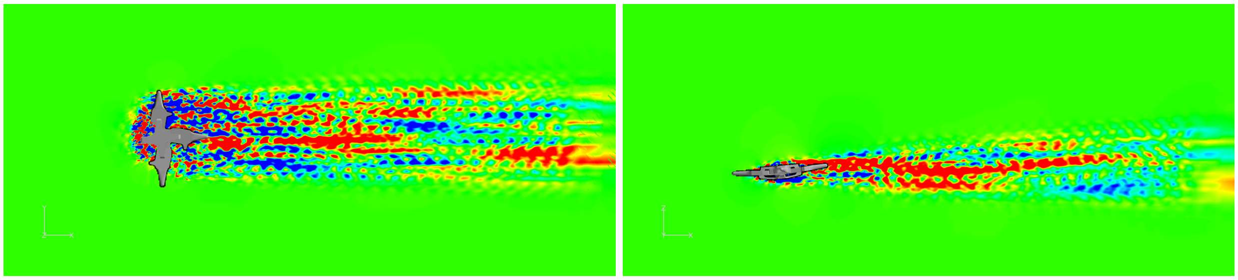

(c) Defeatured Baseline Hub **(d)** Defeatured Baseline Hub

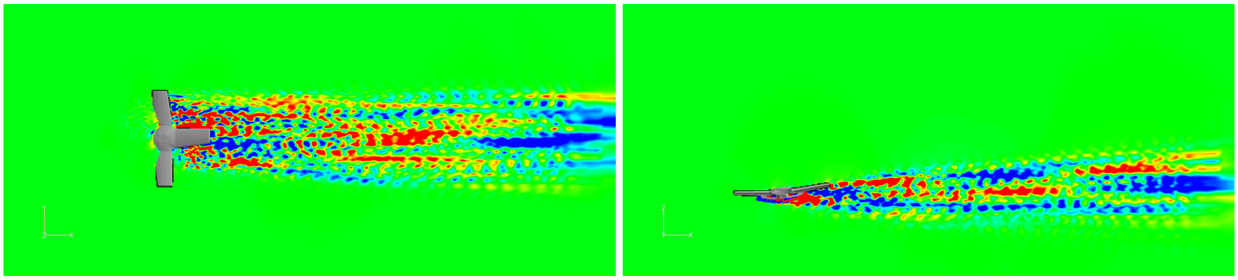

(e) Low Drag Hub **(f)** Low Drag Hub

Fig. 4.15 Spatial Shape of the Highest Energy POD Mode same 15° of hub rotation. A uniform windowing function was used to reduce spectral leakage with an equal weighting, and an overlap of 50%.

As with the previous forms of modal decomposition the modal energy distributions were extracted and plotted in Fig. 4.16. Due to the nature of the SPOD process it produces a set of spatial modes for each frequency. These results are given in the form of energy versus the per revolution frequency with each line representing a specific mode number. Each of the three hubs showed a high energy first mode with significantly higher energy content than the subsequent modes. In all three of the hubs the 2/rev content was the most energetic, despite the lack of 2/rev forcing in the Defeatured Baseline and Low Drag hubs. The energy distribution for the Baseline hub also showed the 2nd most energetic mode possessed relatively more energy when compared to the next modes, especially at the 2/rev and 4/rev frequencies.

The spatial shapes of the highest energy mode at the 2/rev frequency for each hub are shown in Fig. 4.17. The results for the Baseline hub can be seen in both z-plane, Fig. 4.17a, and y-plane view, Fig. 4.17b. The z-plane view of the 2/rev content show an alternating pattern in high and low intensity structures being shed into the wake. In the flow near the hub itself a high intensity structure can be seen forming in the forward quadrant on the advancing side of the hub while another high intensity structure is already being shed into the wake from the retreating side. Based on the symmetry of the blade shanks and scissor arms, it is likely that these high intensity structures are the result of the interaction between the scissor arm and the blade shanks in front of and behind it. The wake visualizations via an isosurface of vorticity magnitude in Fig. 4.10a showed highly turbulent separated flows forming on the advancing blade arm. This flow would be advected downstream just as the following scissor, which also was seen to created highly separated turbulent flow, is advancing into a fully perpendicular position. As the hub continues the blade stud behind the scissor arm must also advance into this system adding its own turbulent content to the flow. This compounding of separated flow is a likely cause for the high intensity structures. The low-intensity structures then are formed as the flow over the second blade arm allowed to move downstream free of interaction with a scissor arm. This further supports the earlier theory that the interactional aerodynamics between the scissor arms and the surrounding components lead to the formation coherent, high strength structures in the flow in the flow.

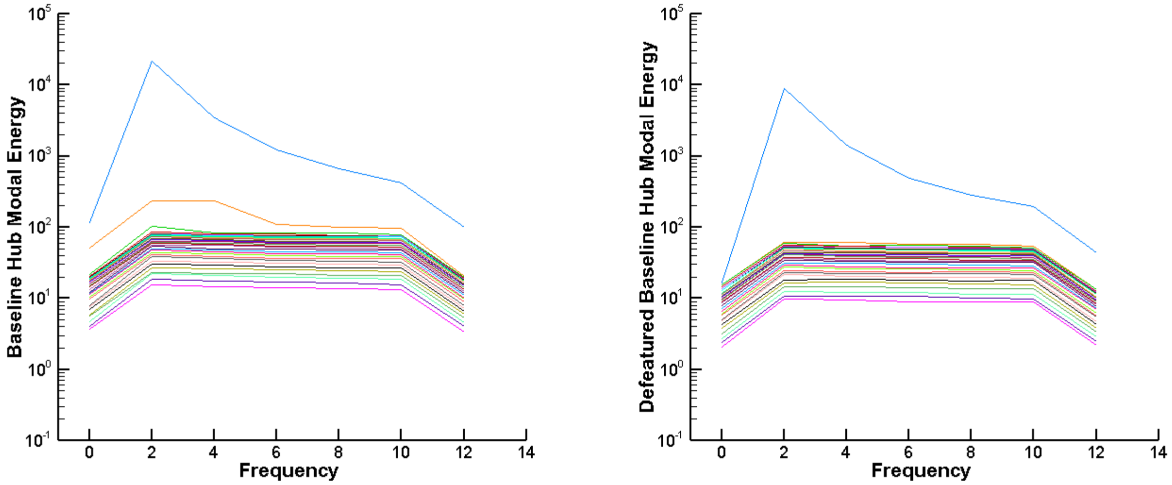

(a) Baseline Hub **(b)** Defeatured Baseline Hub

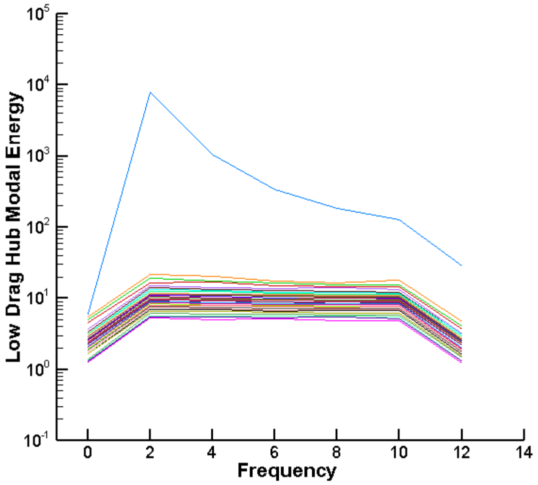

(c) Low Drag Hub

Fig. 4.16 SPOD Percent Modal Energy Distribution

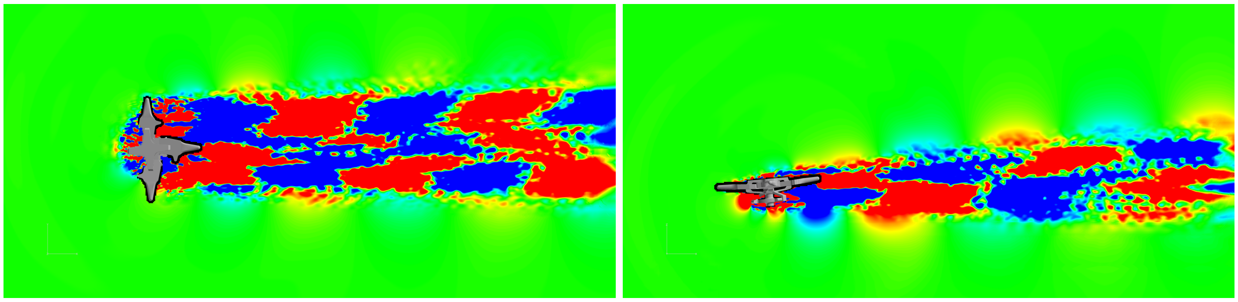

(a) Baseline Hub

(b) Baseline Hub

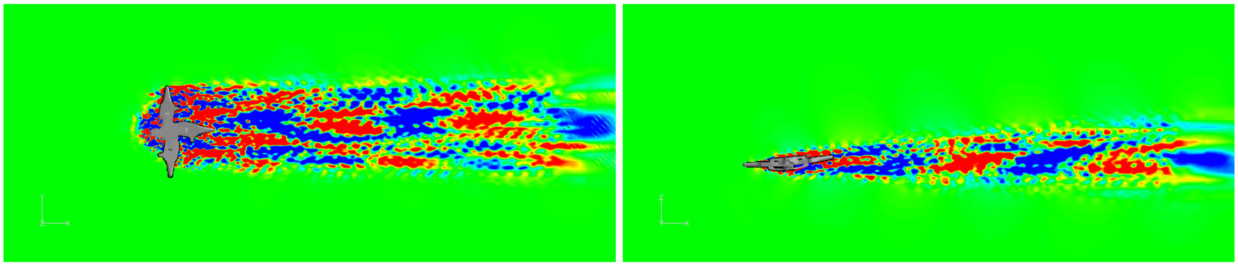

(c) Defeatured Baseline Hub

(d) Defeatured Baseline Hub

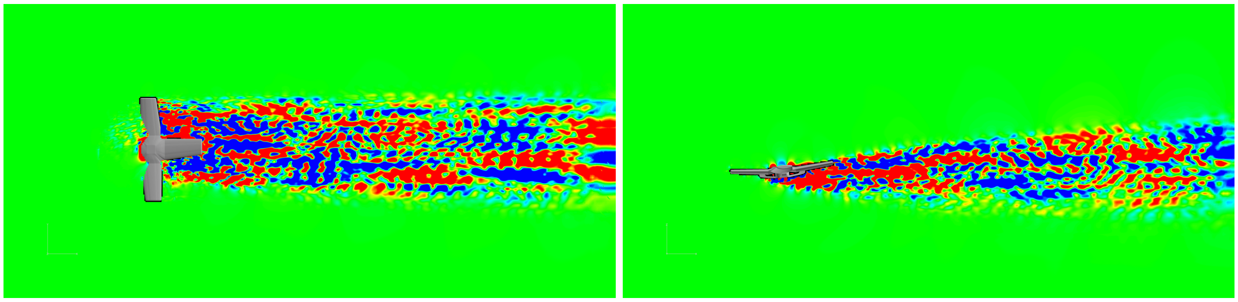

(e) Low Drag Hub

(f) Low Drag Hub

Fig. 4.17 Spatial Shape of the 2/rev content of the 1st SPOD Mode

The y-plane view similarly shows a coherent alternating pattern of high and low intensity structures being shed into the wake. From the y-plane view, an offset exists between the upper and power portions of the wake. As the scissor arms are off set from the blade shanks by approximately 45°, this offset is consistent with the initial flow separation and vortex formations from the blade shank being compounded by interactions with the following scissor arm flow.

However, this coherence is not present in the 2/rev content of the most energetic mode for the other two hubs, shown in Fig. 4.17c, 4.17d-4.17f. While the modal energies of each of the hubs showed the highest energy frequency to be the 2/rev frequency, neither the Defeatured Baseline hub or the Low Drag hub showed comparable levels of coherence in the structure of their wake compared to the Baseline hub at that frequency. While there are streaks of both high and low intensity present in both the z-plane and y-plane views for both hubs they do not show the same strong pattern or coherence as in the Defeatured Baseline.

As all the hubs possessed strong 4/rev geometric forcing based on their symmetries, the most energetic 4/rev mode was also examined, despite its lower modal energy than the 2/rev content. The spatial shapes for the 4/rev content of the highest energy mode for each hub are shown in Fig. 4.18. In the instance of the 4/rev content all of hubs showed similar results in both their y-plane and z-plane. Starting with the Defeatured Baseline hub, shown in Fig 4.18a & 4.18b, while the structures are not of the same size as in the 2/rev content, coherent structures are present. A periodic formation of high and low intensity structures can be seen in the z-plane behind the retreating arm. The wake behind the advancing side of the hub also shows somewhat coherent structures immediately behind the hub. Interestingly, the wake seems to become more coherent one hub diameter downstream of the actual hub. Before this point the structures in the wake behind the advancing and retreating arms have two different patterns. As the high and low intensity structures are advected downstream they shift, eventually aligning with one another forming into more stratified alternating high and lower intensity structures approximately two hub diameters down-stream.

In examining the spatial shape of the highest 4/rev energy mode for the Defeatured Baseline hub, shown in Fig. 4.18c&4.18d for the z-plane and y-plane respectively, Similar behavior can be observed. While the flow in the vicinity of the hub is less coherent in both planes as it moves further downstream the high and low intensity structures resolve into a more coherent pattern approximately three hub diameters downstream.

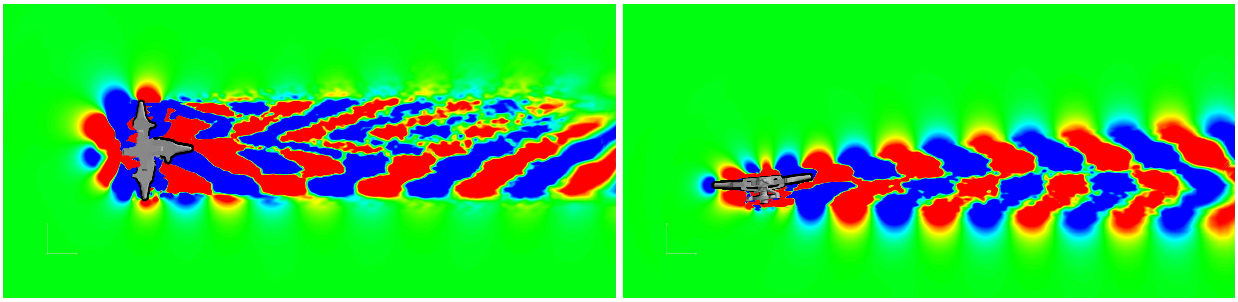

(a) Baseline Hub **(b)** Baseline Hub

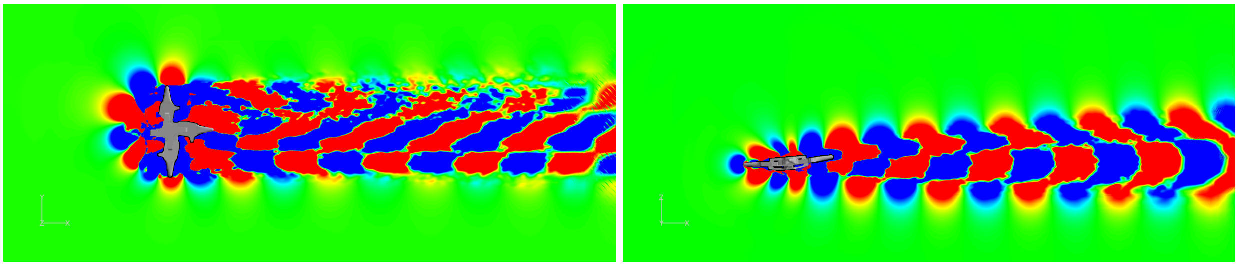

(c) Defeatured Baseline Hub **(d)** Defeatured Baseline Hub

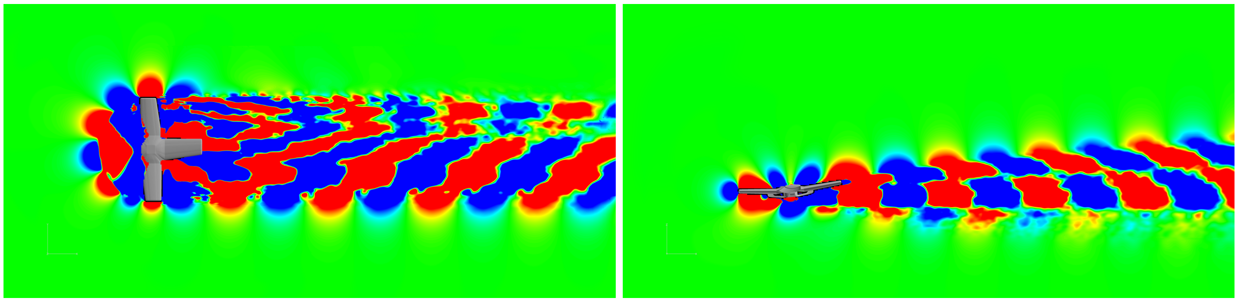

(e) Low Drag Hub **(f)** Low Drag Hub

Fig. 4.18 Spatial Shape of the 4/rev content of the 1st SPOD Mode

The Low Drag hub showed results more similar to the Baseline hub than the Defeatured Baseline hub in regard to the spatial shapes of its highest energy 4/rev mode. The z-plane view of the mode's spatial shape, shown in Fig. 4.18e, the wake of the retreating arm quickly resolves itself into a coherent pattern of higher and lower intensity structures after approximately 1 hub radius of travel. The wake of the advancing arm also forms a fairly coherent pattern of high and lower intensity structures that remain offset from the retreating arm pattern until approximately three hub diameters downstream. The y-plane view, Fig. 4.18f, also shows coherent patterning with a high intensity structure forming on the tip of the aft most blade arm. Over the length of two hub diameters downstream the high and low intensity structures separate across the plane at the tip of the blade stub, but resolve into coherent structures again approximately four hub diameters down stream.

In each of the three hubs, coherent shedding is seen in both the z-plane and y-plane, with the wake actually showing increasing coherence with increased down stream distance. These high and low intensity structures would optimally be capturing the presence of bodies of high and low intensity variation in the streamwise momentum most likely caused by the existence eddies in the wake being shed from the hub and advected downstream.

4.2.3 Space Time POD

As with the previous two forms of modal decomposition, the first step of examining the space time POD results was to examine the distributions of modal energy from each hub. The space-time POD works by treating individual revolutions as entries in the stochastic ensemble, there by the number of modes will be equal the number of revolutions used, i.e. 20 for the Baseline and Defeatured Baseline hubs and 27 for the Low Drag hub.

Shown in Fig. 4.19b are the results for the modal energy distribution of the space time POD modes. For the Baseline hub the first mode can be seen to hold just under 24% of the modal energy. The second mode captured approximately 6% of the modal energy with every subsequent mode and every mode capturing approximately 4%. The modal distribution for the Defeatured Baseline hub and the Low Drag hub are shown in Fig. 4.19b and Fig. 4.19c, respectively. The first mode of both these hubs can be seen capture significantly less modal energy then the Baseline hub, with their first modes capturing approximately 5.5% for the Defeatured Baseline hub and approximately 4.5% for

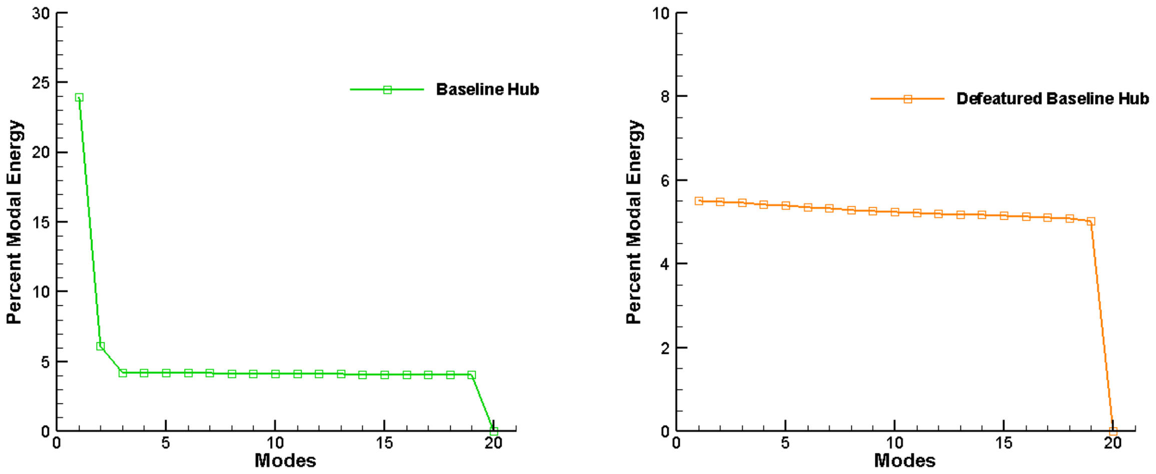

(a) Baseline Hub

(b) Defeatured Baseline Hub

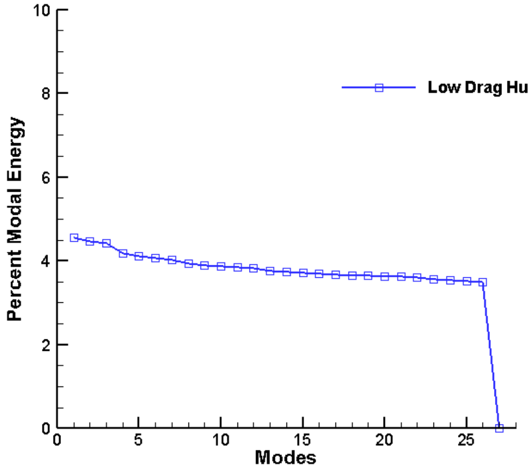

(c) Low Drag Hub

Fig. 4.19 Space-Only Percent Modal Energy Distribution the Low Drag hub. Both of these hub also displayed consistently even modal energy distributions across their subsequent modes decreasing by less than a percent modal energy in both cases. The last mode is an exception to this distribution however, the last mode of mean-subtracted POD is always zero. As before this even energy distribution indicates a lack of coherence in the wake.

The spatial contour of the mean subtracted space time POD modes for each hub are shown in Fig. 4.20 for both z-plane and y-plane views. As before these planes are set at the Z=0 and Y=0 positions respectively. In all the case of all three hubs very little coherence can be seen. The Defeatured Baseline hub, which showed the highest modal energy, exhibits larger patches of high and low energy regions within the wake, but these do not show any sort of coherent patterning or behavior. The Defeatured Baseline and Low Drag Hubs showed high amounts of fluctuations within their wake content with no coherent patterns or even regions of noticeable size. Based on the low firs-mode energies, relatively even distributions of modal energy, and erratic spatial shape of the 1st mode, the space-time POD method does no indicate coherent cycle-to-cycle variations in the results.

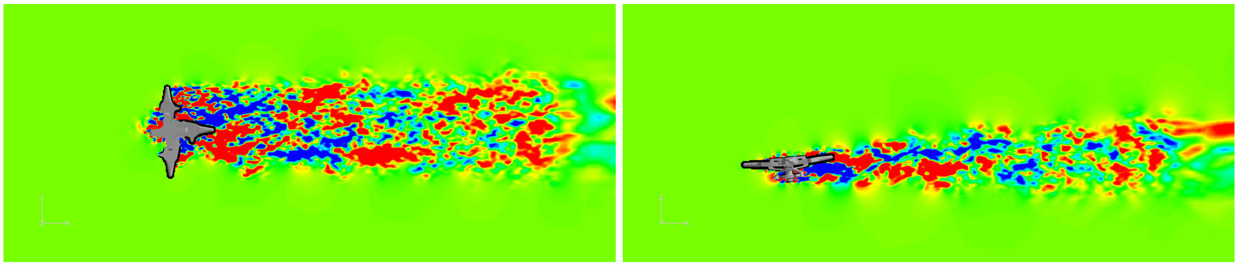

(a) Baseline Hub **(b)** Baseline Hub

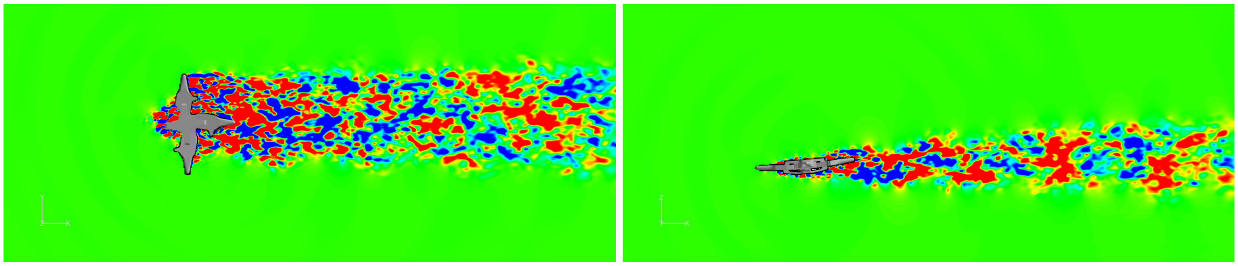

(c) Defeatured Baseline Hub **(d)** Defeatured Baseline Hub

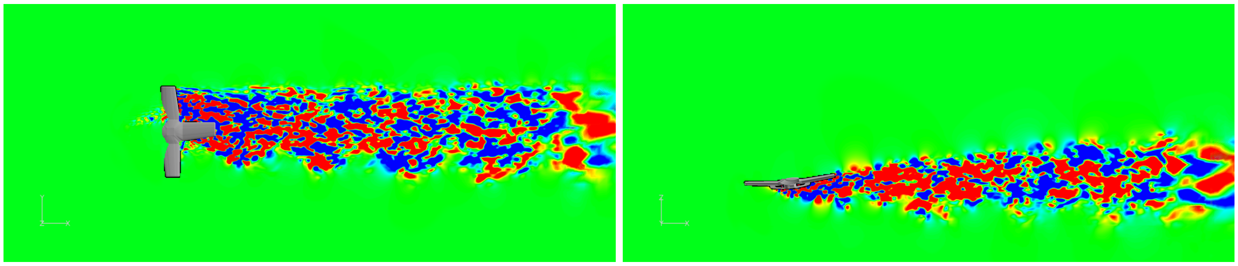

(e) Low Drag Hub **(f)** Low Drag Hub

Fig. 4.20 Spatial Shape of the 2/rev content of the 1st SPOD Mode

Chapter 5: Conclusions

Simulations were conducted for three rotor hub geometries in free air and one inside of a simulated water tunnel. In every case the hubs were simulated an angle of attack of $-5°$ to simulate forward flight. These simulation were conducted with the structured, overset, Reynolds-Averaged Navier-Stokes equations solver OVERFLOW 2.2n, developed by NASA. The flow was modeled using a hybrid RANS/LES methodology. The hub geometries used here were the subject of an extensive serious of experimental investigations carried out at the Pennsylvania State University Applied Research Laboratory in the 48" Garfield Thomas Water Tunnel. This series of experiments created a data base of surface force measurements which were used as validation against the results predicted by CFD. Body-fitted grids systems for two of the hub geometries used in those experiments were provided by PSU-ARL, and were used to derive the geometries used in his work.

The first CFD case simulated the Baseline hub geometry inside a representation of the GTWT experimental installation and served as comparative baseline for the free air hub simulations. This grid system was then modified by removing the tunnel walls and mounting pylon, leaving only hub assembly. This constituted the first isolated hub geometry, dubbed the Baseline hub. The Baseline hub grid system was further modified by removing the swashplate, scissor arms, and rotor mast, leaving only the blade arms and spider plates. This grid system was dubbed the Defeatured Baseline hub and constituted the second free air simulation. The final free air simulation was conducted using a different hub geometry, referred to as the Low Drag hub. This geometry was derived from the Baseline hub, and create in the course of the prior experimental studies at PSU-ARL. The upper spider plate was removed from the Baseline hub and the blade arms were replaced with DBLN airfoils, which were inverted and featured an increased chord length. This hub was also designed to preserve the same frontal area as the Baseline Hub, as frontal area is one of the leading parameters tied to hub drag.

Four revolutions of non-time accurate simulation were used to damp the startup transients for each hub. An additional five revolutions of time accurate simulation were then conducted to allow for statistical convergence before data collection began. Fifteen full revolutions of data were collected for the Full Tunnel case, twenty for the Baseline and Defeatured Baseline Hubs, and twenty-seven revolutions were collected for the Low Drag Hub. In total each of the free air hubs were simulated for at least 29 full revolutions, which is more than the current standard practice for rotor hubs flows.

Surface force predictions were gathered every 2.5° of azimuthal rotation, and full flow field solutions every 15° azimuth rotation. The CFD-predicted flat plate area statistics of the full time series for each hub were used to calculate the ensemble average of each azimuth point where force data was collected. These averages were then compared to the experimental data for the Baseline hub geometry. Local maxima and minima for the hub drag were predicted at approximately the expected azimuthal positions of 0°, 90°, 180°, 270° and 360°, with slight variations in the locations for each hub. The full tunnel simulation showed a notable 2/rev fluctuation in predictions for the local drag maxima, predicting $D/q \approx 64\text{in}^2$ at 90° and 270° rotation and $D/q \approx 58\text{in}^2$ at 180° and the 360° rotation. At the latter two locations the CFD predictions agreed well with the experimental results, while significantly over predicting them at the former azimuthal positions. The free air predictions did not exhibit a strong 2/rev behavior in the drag force, predicting similar values at each local maxima.

Fast Fourier Transforms were used on the predicted surface forces to examine the load harmonics for each of the three free air simulations. All of the hubs were dominated by the 4/rev frequency which was expected given their 4-fold geometric symmetry. In addition, the Defeatured Baseline hub displayed a much larger 2/rev content in both lift and drag than the other two hubs. This 2/rev frequency was found to decrease as the number of revolutions included in the FFT was increased. The magnitude of the 2/rev drag content was seen to decrease slightly as the number of revolutions was increased from 8 to 12, and then to sharply decrease as the number of revolutions was increased to 20. Similar results were seen for the lift harmonics between 12 and 20 revolutions, but an increase in the 2/rev lift content was seen between 8 and 12 revolutions. The 4/rev content converged more quickly, but the higher harmonics were seen to vary inconsistently when comparing the results of the FFT process on 15 and 20 included revolutions. Based on these findings it is believed that the even after a minimum of 29 full revolutions the unsteady harmonics of the flow have not reached convergence.

Several forms of modal decomposition were also applied to both the surface forces and hub wake. The first form of modal decomposition, snapshot proper orthogonal decompositions, works by build a matrix of flow realizations and subject it to a singular value decomposition, which produces a set of data driven modes which represent the most average behaviors of the perturbations in a specific quantity. A mean-subtracted POD was applied to the predicted flat plate area statistics of the three isolated hubs, it revealed no coherent behavior in the perturbations about the mean behavior revealed by the ensemble average. A non-mean-subtracted snapshot POD was also applied to the streamwise momentum of all thee hub wakes as well. This form of POD revealed that the ensemble of the streamwise momentum was fairly steady with no significant perturbations.

The second form of decomposition was applied only to the hub wakes and is called spectral proper orthogonal decomposition (SPOD). Unlike the snapshot POD, SPOD makes use of a FFT and a modal decomposition to produce modes which are both spatially and temporally coherent. The 1st SPOD mode for each of the three hub wakes contained a larger amount of modal energy than higher modes, and all three showed the highest energy content at the 2/rev frequency. The spatial shapes of both 1st and 2nd mode of both the 2/rev and 4/rev content for each hub were shown. The Baseline hub wake showed coherent structures of alternating high and low intensity within the wake at both the 2/rev and 4/rev frequency. The Defeatured Baseline hub and Low Drag hub, however, showed coherent structures only at the 4/rev frequency. In addition the structures in the wake of each hub coalesced into more strongly coherent patterns at approximately 3 hub diameters downstream of the hubs.

Based on the results of the POD, Space-Time POD, and SPOD processes, modal decompositions appear to have inconsistent usefulness in application to rotor hub flows. The results of the snapshot POD indicated that the ensemble average is a steady mean behavior, at least with respect to streamwise momentum. The snapshot POD and mean-subtracted Space time POD results showed low first mode energy and even modal energy distributions. Neither method indicated the presence of any other strongly average behavior or coherent perturbations.

However, the SPOD results showed a much higher energy first mode than the other decompositions, with the highest energy content being captured at the 2/rev frequency. The spatial shapes of the 2/rev content showed coherence in the wake of the Baseline hub but not in the wake of the other two hubs. The 4/rev wake content showed coherence in all hubs cases, with the structures in the wake becoming more coherent as they moved further down stream. In the context of spectral content these wakes do exhibit coherent behaviors. No coherent structures were observed in the surface forces of the hubs so it is unlikely modal decompositions will be of high value in that regard. In addition, it seems that key unsteady harmonics do not reach a converged state in the amount of revolutions typically simulated in common practice, i.e. approximately 15 revolutions of data and fewer for post processing.

References

[1] Lim, J. W., and Dimanlig, A. C., “The effect of fuselage and rotor hub on blade-vortex interaction airloads and rotor wakes,” 2010.

[2] Antoniadis, A., Drikakis, D., Zhong, B., Barakos, G., Steijl, R., Biava, M., Vigevano, L., Brocklehurst, A., Boelens, O., Dietz, M., et al., “Assessment of CFD methods against experimental flow measurements for helicopter flows,” *Aerospace Science and Technology*, Vol. 19, No. 1, 2012, pp. 86–100.

[3] Raghav, V., Shenoy, R., Ortega, F., Komerath, N., and Smith, M., “Exploration of the Physics of Hub Drag,” *50th AIAA Aerospace Sciences Meeting including the New Horizons Forum and Aerospace Exposition*, 2012, p. 1070.

[4] Khier, W., “Computational Investigation of Advanced Hub Fairing Configurations to Reduce Helicopter Drag,” *40th European Rotorcraft Forum*, 2014.

[5] Harris, F. D., *Introduction to Autogryos, Helicopters, and Other V/STOL Aircraft, Volume II: Helicopters*, 1st ed., chapter and pages.

[6] Logan, A., Morger, K., and Sampatacos, E., “Design, Development, and Testing of the No Tail Rotor (NOTAR) Demonstrator,” *67th AHS Annual Forum*, 2011.

[7] Leishman, G. J., *Principles of helicopter aerodynamics with CD extra*, Cambridge university press, 2006.

[8] Fradenburgh, E., and Carlson, R., “The Sikorsky Dynaflex Rotor—an advanced main rotor system for the 1990’s,” *40th Annual Forum of the American Helicopter Society, Arlington, Virginia*, 1984.

[9] Reich, D., Shenoy, R., Smith, M., and Schmitz, S., “A review of 60 years of rotor hub drag and wake physics: 1954–2014,” *Journal of the American Helicopter Society*, Vol. 61, No. 2, 2016, pp. 1–17.

[10] Ormiston, R., “Revitalising advanced rotorcraft research – and the compound helicopter,” *The Aeronautical Journal*, Vol.120, No.1223, 2016.

[11] Shenoy, R., and Smith, M. J., “Deconstructing Hub Drag. Part 2. Computational Development and Anaysis,” Tech. rep., Georgia Inst. Of Technology. Atlanta School Of Aerospace Engineering, 2013.

[12] Schmitz, S., Reich, D., Smith, M. J., and Centolanza, L. R., “1st Rotor Rub Flow Prediction Workshop Experimental Data Campaigns & Computational Analyses,” *American Helicopter Society 73rd Annual Forum and Technology Display, Fort Worth, TX*, 2017.

[13] Sheehy, T. W., “A general review of helicopter rotor hub drag data,” *Journal of the American Helicopter Society*, Vol. 22, No. 2, 1977, pp. 2–10.

[14] Chan, W., Rogers, S., Nash, S., Buning, P., Meakin, R., Boger, D., and Pandya, S., “Chimera Grid Tools User’s Manual, Version 2.0,” *NASA Ames Research Center*, 2007.

[15] Biedron, R. T., Carlson, J. R., Derlaga, J. M., Gnoffo, P. A., Hammond, D. P., Jones, W. T., Kleb, B., Lee-Rausch, E. M., Nielsen, E. J., Park, M. A., et al., “FUN3D Manual: 13.6,” 2019.

[16] Fluent, A., “13.0 Documentation, ANSYS,” *Inc., Canonsburg, Pa, USA*, ????

[17] Fodor, I. K., “A survey of dimension reduction techniques,” Tech. rep., Lawrence Livermore National Lab., CA (US), 2002.

[18] Hall, K. C., Thomas, J. P., and Dowell, E. H., “Reduced-Order Modeling Of Unsteady Small-Disturbance Flows Using A Frequency-Domain Proper Orthogonal Decomposition Technique,” *AIAA 37th Aerospace Sciences Meeting and Exhibit*, January, 1999.

[19] US Department of Transportation, ., faah808321 edition, “FAA Helicopter Flying Handbook,” *URL www. faa. gov*, Vol. 91, ????

[20] Pallet, E. H. J., and Coyle, S., *Automatic Flight Controls*, 4^{th} ed., chapter and pages.

[21] Prouty, R. W., and Curtiss Jr, H., "Helicopter control systems: A history," *Journal of Guidance, Control, and Dynamics*, Vol. 26, No. 1, 2003, pp. 12–18.

[22] Seddon, J. M., and Newman, S., *Basic helicopter aerodynamics*, Vol. 40, John Wiley & Sons, 2011.

[23] Shenoy, R., Ortega, F., Raghav, V., Smith, M., and Komerath, N., "Deconstructing Hub Drag," *29th AIAA Applied Aerodynamics Conference*, 2011, p. 3821.

[24] Prouty, R., *Rotor Wing International Magazine*, 1983, pp. 26–28.

[25] Huber, H., "Will Rotor Hubs Lose Their Bearings: A Survey Of Bearingless Main Rotor Development," *Eighteenth European Rotorcraft Forum*, 1992, France.

[26] Leishman, J. G., and Johnson, B., "Engineering Analysis of the 1907 Cornu Helicopter," *Journal of the American Helicopter Society*, Vol. 54, No. 3, 2009, pp. 34001–34001.

[27] Bousman, W. G., Ormiston, R. A., and Mirick, P. H., "Design considerations for bearingless rotor hubs," Tech. rep., ARMY RESEARCH AND TECHNOLOGY LABS MOFFETT FIELD CA AEROMECHANICS LAB, 1983.

[28] Dixon, P. G., "Design, Development, and Flight Demonstration of the Loads and Stability Characteristics of a Bearingless Main Rotor." Tech. rep., BOEING VERTOL CO., PHILADELPHIA, PA, 1980.

[29] Boulet, J., *History of the helicopter: as told by its pioneers, 1907-1956*, Editions France-Empire, 1984.

[30] Hirschberg, M., "The American Helicopter, An Overview of Helicopter Developments in America 1908-1999," , 2002.

[31] Gibbings, D., "The Evolution Of the British Rotorcraft Industry 1842-2009," *35th European Rotorcraft Forum*, 2009.

[32] Fayette Taylor, C., "Aircraft propulsion; a review of the evolution of aircraft piston engines," *Smithsonian Annals of Flight*, 1971.

[33] Humphrey, T. C., Bose, N., Williams, C., and Snow, M., "Design and fabrication of a collective and cyclic pitch propeller," *ASME 2004 23rd International Conference on Offshore Mechanics and Arctic Engineering, American Society of Mechanical Engineers*, 2004, pp. 653–659.

[34] Faure, T. M., "The quest of vertical flight: the development of helicopter," 2015.

[35] Munson, K., *Helicopters and other rotorcraft since 1907*, Macmillan, 1969.

[36] Leishman, J. G., "Development of the autogiro: A technical perspective," *Journal of Aircraft*, Vol. 41, No. 4, 2004, pp. 765–781.

[37] Raoul, H., "Helicopter and rotating wing aircraft," , July 1937.

[38] Vodegel, H., and Jessurun, K., "A Historical Review of Two Helicopters Designed in the Netherlands," *Twenty First European Rotorcraft Forum*, 1995, Saint-Petersburg, Russia.

[39] Young, A. M., *The Bell Notes: A journey from physics to metaphysics*, Delacorte Press, 1979.

[40] Daughaday, H., and DuWaldt, F., "Helicopter Handling Qualities Investigation Phase II Analysis of Helicopter Stabilization and Control Problems Part C Characteristics and Comparison of Existing Helicopter Stabilizing Devices," Tech. rep., Cornell Aeronautical Lab INC., Buffalo, NY, 1955.

[41] Hirschel, E. H., Prem, H., and Madelung, G., *Aeronautical research in Germany: from Lilienthal until today*, Springer Science & Business Media, 2012.

[42] Brooks, G. W., and Sylvester, M. A., “Description and Investigation of a Dynamic Model of the XH-17 Two-Blade Jet-Driven Helicopter,” *NACA RM L50I21*, 1951.

[43] Cresap, W. L., Myers, A. W., and Viswanathan, S. P., “Design and Development Tests of a Four-Bladed Light Helicopter Rotor System,” *Journal of the American Helicopter Society*, Vol. 24, No. 1, 1979, pp. 20–25.

[44] Huston, R. J., and Tapscott, R. J., “Results of Some Wind Tunnel and Flight Studies with Helicopters at NASA,” *NYASA*, Vol. 107, No. 1, 1963, pp. 57–69.

[45] Hughes, C. W., and Wernicke, R. K., “Flight test of a hingeless flexbeam rotor system,” Tech. rep., Bell Helicopter Textron INC., Fort Worth, TX, 1974.

[46] Weiland, E. F., “Development and test of the BO 105 rigid rotor helicopter,” *Journal of the American Helicopter Society*, Vol. 14, No. 1, 1969, pp. 22–37.

[47] Donham, R., Cardinale, S., and Sachs, I., “Ground and Air Resonance Characteristics of a Soft In-Plane Rigid-Rotor System,” *Journal of the American Helicopter Society*, Vol. 14, No. 4, 1969, pp. 33–41.

[48] Cassier, A., “Development of the triflex rotor head,” *Journal of the American Helicopter Society*, Vol. 26, No. 3, 1981, pp. 25–31.

[49] Cler, A., “High-Speed Dauphin Fuselage Aerodynamics,” *Fifteenth European Rotorcraft Froum*, 198, Amsterdam, Netherlands.

[50] Cler, A., “Mouille, R. and Bietenhader, C.” *Tenth European Rotorcraft Froum*, 1984, The Hague, Netherlands.

[51] Niebanck, C. F., and Goodman, R. K., “Test results from a dynamic model dynaflex rotor,” *Rotorcraft Dynamics*, 1985, p. 57.

[52] von Kármán, T., “Recent European Developments in Helicopters,” 1921.

[53] Harrington, R. D., “Reduction of Helicotper Parasite Drag,” *NACA TN 3234*, 1954.

[54] Jones, J. R., and Lund, P. D., “Full Scale Investigation of Rotor Hub Fairing for a Sikorsky H-5 Rotor Hub,” , ????

[55] Churchill, G. B., and Harrington, R. D., “Parasite-Drag Measurements Of Five Helicopter Rotor Hubs,” *NASA MEMO 1-31-59L*, 1959.

[56] Moser, H. H., “Full Scale Wind Tunnel Investigation of Helicopter Drag,” *Journal of the American Helicopter Society*, Vol. 6, No. 1, 1961, pp. 27–33.

[57] Sweet, G. E., and Jenkins, J. L., “Wind-Tunnel Investigation Of The Drag And Static Stability Characteristics Of FOur Helicopter Fuselage Models,” *NASA TN D-1363*, 1962.

[58] Montana, P. S., “Experimental investigation of three rotor hub fairing shapes,” Tech. rep., David W. Taylor Naval Ship Research And Development Center, Bethesda, MD, 1975.

[59] Sheehy, T. W., and Clark, D. R., “A method for predicting helicopter hub drag,” Tech. rep., United Technologies Corp, Stratford, CT, Sikorsky Aircraft Div., 1976.

[60] Keys, C., and Rosenstein, H., “Summary of Rotor Hub Drag Data,” *NASA CR-152080*, 1978.

[61] Logan, A. H., Prouty, R. W., and Clark, D. R., “Wind tunnel tests of large-and small-scale rotor hubs and pylons,” Tech. rep., Hughes Helicopters Inc., Culver City, CA, 1981.

[62] Felker, F. F., “An experimental investigation of hub drag on the XH-59 A,” *AIAA 3rd Applied Aerodynamics Conference*, 1985.

[63] Roesch, P., and Dequin, A.-M., "Experimental research on helicopter fuselage and rotor hub wake turbulence," *Journal of the American Helicopter Society*, Vol. 30, No. 1, 1985, pp. 43–51.

[64] Young, L. A., Graham, D. R., and Stroub, R. H., "Experimental Investigation of Rotorcraft Hub and Shaft Fairing Drag Reduction," *Journal of Aircraft*, Vol. 24, No. 12, 1987, pp. 861–867.

[65] Graham, D. R., Sung, D. Y., Young, L. A., Louie, A. W., and H., S. R., "Helicopter Hub Fairing And Pylon Interference Drag," *NASA TM 101052*, 1989.

[66] Sung, D. Y., Lance, M. B., Young, L. A., and Stroub, R. H., "An Experimental Envestigation of Helicopter Rotor Hub Fairing Drag Characteristics," *NASA TM 102182*, 1989.

[67] Martin, D. M., Mort, R. W., Squires, P. K., and Young, L. A., "Hub and pylon fairing integration for helicopter drag reduction," *American Helicopter Society's 47th annual Forum*, 1991.

[68] Martin, D. M., Mort, R. W., and Young, L. A., "An Experimental Investigation of Helicopter Rotor Hub Fairing Drag Characteristics," *NASA TM 4540*, 1993.

[69] Gorton, S. A., Meyers, J. F., and Berry, J. D., "2nd Rotor Hub Flow Prediction Workshop Experimental Data Campaigns & Computational Analyses," *American Helicopter Society 52nd Annual Forum Proceedings, Washington, DC*, 1996.

[70] Gorton, S. A., Berry, J. D., Hodges, W. T., and Reis, D. G., "Flow Environment Study Near the Empennage of a 15-Percent Scale Helicopter Model," *NASA TP-2000-210085*, 2000.

[71] Gorton, S. A., Berry, J. D., Hodges, W. T., and Reis, D. G., "Rotor Wake Study Near the Horizontal Tail of a T-Tail Configuration," *Journal of Aircraft*, Vol. 39, No. 4, 2002, pp. 645–653. https://doi.org/10.2514/2.2977.

[72] Berry, J., "Unsteady Velocity Measurements Taken Behind a Model Helicopter Rotor Hub in Forward Flight," *NASA TM 4738*, 1997.

[73] Raghav, V., Shenoy, R., Smith, M., and Komerath, N., "Investigation of drag and wake turbulence of a rotor hub," *Aerospace Science and Technology*, Vol. 28, No. 1, 2013, pp. 164–175.

[74] Reich, D., Elbing, B. R., Berezin, C. R., and Schmitz, S., "Water Tunnel Flow Diagnostics of Wake Structures Downstream of a Model Helicopter Rotor Hub," *Journal of the American Helicopter Society*, Vol. 59, No. 3, 2017, pp. 4013–4041.

[75] Reich, D., Willits, S., and Schmitz, S., "Scaling and configuration effects on helicopter rotor hub interactional aerodynamics," *Journal of Aircraft*, Vol. 54, No. 5, 2017, pp. 1692–1704.

[76] Schmitz, S., Tierney, C., Metkowski, L., Reich, D., Jaffa, N. A., Centolanza, L. R., and Thomas, M. L., "2nd Rotor Hub Flow Prediction Workshop Experimental Data Campaigns & Computational Analyses," *Vertical Flight Society's 75th Annual Forum and Technology Display, Philadelphia, PA*, 2019.

[77] Landgrebe, A. J., Moffitt, R. C., and Clark, D. R., "Aerodynamic Technology for Advanced Rotorcraft-Part I," *Journal of the American Helicopter Society*, Vol. 22, No. 2, 1977, pp. 21–27.

[78] Lorber, P. F., and Egolf, T. A., "An Unsteady Helicopter Rotor-Fuselage Aerodynamic Interaction Analysis," *Journal of the American Helicopter Society*, Vol. 35, No. 3, 1990, pp. 32–42.

[79] Renaud, T., O'Brien, D., Smith, M., and Potsdam, M., "Evaluation of Isolated Fuselage and Rotor-Fuselage Interaction Using Computational Fluid Dynamics," *Journal of the American Helicopter Society*, Vol. 53, No. 1, 2008, pp. 3–17.

[80] Ruffin, S., O'Brien, D., Smith, M., Hariharan, N., Lee, J.-D., and Sankar, L., "Comparison of rotor-airframe interaction utilizing overset and unstructured grid techniques," *42nd AIAA Aerospace Sciences Meeting and Exhibit*, 2004, p. 46.

[81] Smith, M. J., Lim, J. W., van der Wall, B. G., Baeder, J. D., Biedron, R. T., Boyd Jr, D. D., Jayaraman, B., Jung, S. N., and Min, B.-Y., "An assessment of CFD/CSD prediction state-of-the-art using the HART II international workshop data," *American Helicopter Society 68th Annual Forum, Fort Worth, TX*, 2012.

[82] Smith, M. J., Lim, J. W., van der Wall, B. G., Baeder, J. D., Biedron, R. T., Boyd, D. D., Jayaraman, B., Jung, S. N., and Min, B.-Y., "The HART II international workshop: an assessment of the state of the art in CFD/CSD prediction," *CEAS Aeronautical Journal*, Vol. 4, No. 4, 2013, pp. 345–372.

[83] Johnson, W., "Camrad-a Comprehensive Analytical Model of Rotorcraft Aerodynamics and Dynamics," 1994.

[84] Rossow, C.-C., Kroll, N., and Schwamborn, D., "The MEGAFLOW Project—Numerical Flow Simulation for Aircraft," *Progress in Industrial Mathematics at ECMI 2004*, Springer, 2006, pp. 3–33.

[85] Steijl, R., Barakos, G., and Badcock, K., "A framework for CFD analysis of helicopter rotors in hover and forward flight," *International journal for numerical methods in fluids*, Vol. 51, No. 8, 2006, pp. 819–847.

[86] Amato, M., Matrone, A., and Schiano, P., "A practical experience in parallelizing a large CFD code: The ENSOLV flow solver," *International Conference on High-Performance Computing and Networking*, Springer, 1994, pp. 508–513.

[87] Biava, M., Pisoni, A., Saporiti, A., and Vigevano, L., "Efficient rotor aerodynamics predictions with an Euler method," *29th European Rotorcraft Forum*, 2003.

[88] Cambier, L., Gazaix, M., Heib, S., Plot, S., Poinot, M., Veuillot, J., Boussuge, J., and Montagnac, M., "An Overview of the Multi-Purpose elsA Flow Solver." *AerospaceLab*, , No. 2, 2011, pp. 1–15.

[89] Steijl, R., and Barakos, G., "Sliding mesh algorithm for CFD analysis of helicopter rotor–fuselage aerodynamics," *International journal for numerical methods in fluids*, Vol. 58, No. 5, 2008, pp. 527–549.

[90] Shenoy, R., Smith, M. J., and Komerath, N., "Computational Investigation of Hub Drag Deconstruction from Model to Full Scale," *37th European Rotorcraft Forum*, 2011.

[91] Shenoy, R., Holmes, M., Smith, M. J., and Komerath, N. M., "Scaling evaluations on the drag of a hub system," *Journal of the American Helicopter Society*, Vol. 58, No. 3, 2013, pp. 1–13.

[92] Shenoy, R., Smith, M. J., and Park, M. A., "Unstructured overset mesh adaptation with turbulence modeling for unsteady aerodynamic interactions," *Journal of Aircraft*, Vol. 51, No. 1, 2014, pp. 161–174.

[93] Schaeffler, N. W., Allan, B. G., Lienard, C., and Le Pape, A., "Progress Towards Fuselage Drag Reduction via Active Flow Control: A Combined CFD and Experimental Effort," Tech. rep., NASA, NF1676L-1024, 2010.

[94] Norman, T. R., Shinoda, P., Peterson, R. L., and Datta, A., "Full Scale Wind Tunnel Test of The UH-60A Airloads Rotor," *40th European Rotorcraft Forum*, 2014.

[95] Potsdam, M., Datta, A., and Jayaraman, B., "Computational investigation and fundamental understanding of a slowed UH-60A rotor at high advance ratio," *68th AHS Annual Forum*, 2016.

[96] Datta, A., Yeo, H., and Norman, T. R., "Experimental investigation and fundamental understanding of a slowed UH-60A rotor at high advance ratios," *67th AHS Annual Forum*, 2011.

[97] Datta, A., Yeo, H., and Norman, T. R., "Experimental investigation and fundamental understanding of a full-scale slowed rotor at high advance ratios," *Journal of the American Helicopter Society*, Vol. 58, No. 2, 2013, pp. 1–17.

[98] Coder, J., Cross, P., and Smith, M., "Turbulence modeling strategies for rotor hub flows," *Proceedings of the 73rd Annual American Helicopter Society Forum*, 2017.

[99] Coder, J., "Effects of Transition Modeling on the Simulation of Helicopter Rotor Hubs," *Vertical Flight Society's 75th Annual Forum and Technology Display, Philadelphia, PA*, 2019.

[100] Coder, J. G., and Maughmer, M. D., "Computational fluid dynamics compatible transition modeling using an amplification factor transport equation," *AIAA journal*, Vol. 52, No. 11, 2014, pp. 2506–2512.

[101] Coder, J. G., "Enhancement of the amplification factor transport transition modeling framework," *55th AIAA Aerospace Sciences Meeting*, 2017, p. 1709.

[102] Jolliffe, I., "Principle Component Analysis. 1955," , ????

[103] Stewart, G. W., "On the early history of the singular value decomposition," *SIAM review*, Vol. 35, No. 4, 1993, pp. 551–566.

[104] Jackson, J., and Edward, A., "User's guide to principal components. John Willey Sons," *Inc., New York*, 1991, p. 40.

[105] Abdi, H., and Williams, L. J., "Principal component analysis," *Wiley interdisciplinary reviews: computational statistics*, Vol. 2, No. 4, 2010, pp. 433–459.

[106] Wold, S., Esbensen, K., and Geladi, P., "Principal component analysis," *Chemometrics and intelligent laboratory systems*, Vol. 2, No. 1-3, 1987, pp. 37–52.

[107] Pearson, K., "LIII. On lines and planes of closest fit to systems of points in space," *The London, Edinburgh, and Dublin Philosophical Magazine and Journal of Science*, Vol. 2, No. 11, 1901, pp. 559–572.

[108] Lumley, J. L., "The structure of inhomogeneous turbulent flows," *Atmospheric turbulence and radio wave propagation*, 1967.

[109] Lumley, J. L., *Stochastic tools in turbulence*, Academic Press, New York, 1970.

[110] Lumley, J. L., "Coherent structures in turbulence," *Transition and turbulence*, Elsevier, 1981, pp. 215–242.

[111] Aubry, N., Holmes, P., Lumley, J. L., and Stone, E., "The dynamics of coherent structures in the wall region of a turbulent boundary layer," *Journal of Fluid Mechanics*, Vol. 192, 1988, pp. 115–173.

[112] Berkooz, G., Holmes, P., and Lumley, J., "The proper orthogonal decomposition in the analysis of turbulent flows," *Annual review of fluid mechanics*, Vol. 25, No. 1, 1993, pp. 539–575.

[113] Holmes, P. J., Lumley, J. L., Berkooz, G., Mattingly, J. C., and Wittenberg, R. W., "Low-dimensional models of coherent structures in turbulence," *Physics Reports*, Vol. 287, No. 4, 1997, pp. 337–384.

[114] Holmes, P., Lumley, J. L., Berkooz, G., and Rowley, C. W., *Turbulence, coherent structures, dynamical systems and symmetry*, Cambridge university press, 2012.

[115] Taira, K., Brunton, S. L., Dawson, S. T., Rowley, C. W., Colonius, T., McKeon, B. J., Schmidt, O. T., Gordeyev, S., Theofilis, V., and Ukeiley, L. S., "Modal analysis of fluid flows: An overview," *AIAA Journal*, Vol. 55, No. 12, 2017, pp. 4013–4041.

[116] Sirovich, L., "Turbulence and the dynamics of coherent structures. I. Coherent structures," *Quarterly of applied mathematics*, Vol. 45, No. 3, 1987, pp. 561–571.

[117] Sirovich, L., "Turbulence and the dynamics of coherent structures. II. Symmetries and transformations," *Quarterly of Applied mathematics*, Vol. 45, No. 3, 1987, pp. 573–582.

[118] Sirovich, L., "Turbulence and the dynamics of coherent structures. III. Dynamics and scaling," *Quarterly of applied mathematics*, Vol. 45, No. 3, 1987, pp. 583–590.

[119] Picard, C., and Delville, J., "Pressure velocity coupling in a subsonic round jet," *International Journal of Heat and Fluid Flow*, Vol. 21, No. 3, 2000, pp. 359–364.

[120] Willcox, K., and Peraire, J., "Balanced model reduction via the proper orthogonal decomposition," *AIAA journal*, Vol. 40, No. 11, 2002, pp. 2323–2330.

[121] Moore, B., "Principal component analysis in linear systems: Controllability, observability, and model reduction," *IEEE transactions on automatic control*, Vol. 26, No. 1, 1981, pp. 17–32.

[122] Dowell, E. H., and Hall, K. C., "Modeling of fluid-structure interaction," *Annual review of fluid mechanics*, Vol. 33, No. 1, 2001, pp. 445–490.

[123] Lall, S., Marsden, J. E., and Glavaški, S., "Empirical model reduction of controlled nonlinear systems," *IFAC Proceedings Volumes*, Vol. 32, No. 2, 1999, pp. 2598–2603.

[124] Rowley, C. W., "Model reduction for fluids, using balanced proper orthogonal decomposition," *International Journal of Bifurcation and Chaos*, Vol. 15, No. 03, 2005, pp. 997–1013.

[125] Schmid, P., and Sesterhenn, J., "Dynamic mode decomposition of numerical and experimental data," *APS*, Vol. 61, 2008, pp. MR–007.

[126] Schmid, P. J., "Dynamic mode decomposition of numerical and experimental data," *Journal of fluid mechanics*, Vol. 656, 2010, pp. 5–28.

[127] Glauser, M. N., Leib, S. J., and George, W. K., "Coherent structures in the axisymmetric turbulent jet mixing layer," *Turbulent Shear Flows 5*, Springer, 1987, pp. 134–145.

[128] Moin, P., and Moser, R. D., "Characteristic-eddy decomposition of turbulence in a channel," *Journal of Fluid Mechanics*, Vol. 200, 1989, pp. 471–509.

[129] Delville, J., Ukeiley, L., Cordier, L., Bonnet, J.-P., and Glauser, M., "Examination of large-scale structures in a turbulent plane mixing layer. Part 1. Proper orthogonal decomposition," *Journal of Fluid Mechanics*, Vol. 391, 1999, pp. 91–122.

[130] Hall, K. C., Thomas, J. P., and Dowell, E. H., "Proper orthogonal decomposition technique for transonic unsteady aerodynamic flows," *AIAA journal*, Vol. 38, No. 10, 2000, pp. 1853–1862.

[131] Hall, K. C., "Eigenanalysis of unsteady flows about airfoils, cascades, and wings," *AIAA journal*, Vol. 32, No. 12, 1994, pp. 2426–2432.

[132] Hall, K. C., Florea, R., and Lanzkron, P., "A Reduced Order Model of Unsteady Flows in Turbomachinery," *Journal of Turbomachinery*, Vol. 117, No. 3, 1995, pp. 375–383.

[133] Dowell, E. H., "Eigenmode analysis in unsteady aerodynamics-reduced-order models," *AIAA journal*, Vol. 34, No. 8, 1996, pp. 1578–1583.

[134] Florea, R., and Hall, K. C., "Eigenmode analysis of unsteady flows about airfoils," *Journal of Computational Physics*, Vol. 147, No. 2, 1998, pp. 568–593.

[135] Hall, K., Thomas, J., and Dowell, E., "Reduced order modeling of unsteady flows using a frequency domain proper orthogonal decomposition technique," *37th Aerospace Sciences Meeting and Exhibit, Reno, NV*, 1999.

[136] Godounov, S., "A finite difference method for the numerical computation of discontinuous solutions of the equations of fluid dynamics," *Math. Sb*, Vol. 47, 1959, pp. 357–393.

[137] Johansson, P. B., George, W. K., and Woodward, S. H., "Proper orthogonal decomposition of an axisymmetric turbulent wake behind a disk," *Physics of Fluids*, Vol. 14, No. 7, 2002, pp. 2508–2514.

[138] Johansson, P. B., and George, W. K., "The far downstream evolution of the high-Reynolds-number axisymmetric wake behind a disk. Part 2. Slice proper orthogonal decomposition," *journal of Fluid Mechanics*, Vol. 555, 2006, p. 387.

[139] Tutkun, M., Johansson, P. B., and George, W. K., "Three-component vectorial proper orthogonal decomposition of axisymmetric wake behind a disk," *AIAA journal*, Vol. 46, No. 5, 2008, pp. 1118–1134.

[140] Mula, S. M., and Tinney, C. E., "Classical and snapshot forms of the POD technique applied to a helical vortex filament," *32nd AIAA Applied Aerodynamics Conference*, 2014, p. 3257.

[141] Mula, S. M., and Tinney, C. E., "A study of the turbulence within a spiralling vortex filament using proper orthogonal decomposition," *Journal of Fluid Mechanics*, Vol. 769, 2015, pp. 570–589.

[142] Glauser, M. N., and George, W., "Orthogonal decomposition of the axisymmetric jet mixing layer including azimuthal dependence," *Advances in turbulence*, Springer, 1987, pp. 357–366.

[143] Ramasamy, M., Wilson, J. S., McCroskey, W. J., and Martin, P. B., "Characterizing Cycle-to-Cycle Variations in Dynamic Stall Measurements," *Journal of the American Helicopter Society*, Vol. 63, No. 2, 2018, pp. 1–24.

[144] Ramasamy, M., Sanayei, A., Wilson, J. S., MArtin, P. B., Harms, T., Nikouyeen, P., and Naughton, J., "Data-Driven Optimal Basis Clustering To Characterize Cycle-to-Cycle Variations in Dynamic Stall Measurements," *VFS 75th Annual Forum*, 2019.

[145] Sanayei, A., Ramasamy, M., and Martin, P., "Development of Modal Analysis Based Clustering Technique Using Pitching Airfoil Measurements," *AIAA SciTech Forum*, 2019.

[146] Wen, G., and Gross, A., "Modal Decomposition of Dynamic Stall for Helicopter Blade Section," *AIAA Scitech 2019 Forum*, 2019, p. 1657.

[147] Huang, N. E., Shen, Z., Long, S. R., Wu, M. C., Shih, H. H., Zheng, Q., Yen, N., Tung, C. C., and Liu, H. H., "The empirical mode decomposition and the Hilbert spectrum for nonlinear and non-stationary time series analysis," *Proceedings of the Royal Society of London. Series A: mathematical, physical and engineering sciences*, Vol. 454, No. 1971, 1998, pp. 903–995.

[148] Nichols, R. H., and Buning, P. G., "User's Manual for OVERFLOW 2.1," *University of Alabama at Birmingham, Birmingham, AL*, 2008.

[149] Nichols, R., Tramel, R., and Buning, P., "Solver and Turbulence Model Upgrades to OVERFLOW 2 for Unsteady and High-Speed Applications," *AIAA 25th Applied Aerodynamics Conference*, AIAA 2006-2824, San Francisco, CA, 2006.

[150] Klopfer, G., Hung, C., Van der Wijngaart, R., and Onufer, J., "A diagonalized diagonal dominant alternating direction implicit (D3ADI) scheme and subiteration correction," *29th AIAA, Fluid Dynamics Conference*, 1998, p. 2824.

[151] Pulliam, T. H., and Chaussee, D., "A diagonal form of an implicit approximate-factorization algorithm," *Journal of Computational Physics*, Vol. 39, No. 2, 1981, pp. 347–363.

[152] Roe, P., "Approximate Riemann Solvers, Parameter Vectors, and Difference Schemes," *Journal Of Computational Physics*, Vol. 43, No. 2, pp. 357-352, 1981.

[153] Nichols, R. H., Trammel, R. W., and Buning, P. G., "Evaluation of Two High-Order Weighted Essentially Nonoscillatory Schemes," *AIAA Journal*, Vol. 46, No.12, pp.3090-3102, 2008.

[154] Jiang, G., and Shu, C., "Efficient Implementation of Weighted ENO Schemes," *Journal of Computational Physics*, Vol. 126, pp.202-228, 1996.

[155] Spalart, P., and Allmaras, S., "A one-equation turbulence model for aerodynamic flows," *30th aerospace sciences meeting and exhibit*, 1992, p. 439.

[156] Allmaras, S. R., and Johnson, F. T., "Modifications and clarifications for the implementation of the Spalart-Allmaras turbulence model," *Seventh international conference on computational fluid dynamics (ICCFD7)*, 2012, pp. 1–11.

[157] Shur, M. L., Strelets, M. K., Travin, A. K., and Spalart, P. R., "Turbulence modeling in rotating and curved channels: assessing the Spalart-Shur correction," *AIAA journal*, Vol. 38, No. 5, 2000, pp. 784–792.

[158] Meakin, R., "Object X-rays for Cutting Holes in Composite Overset Structured Grids," *15th AIAA computational fluid dynamics conference*, 2012.

[159] Rowley, C. W., and Dawson, S. T., "Model reduction for flow analysis and control," *Annual Review of Fluid Mechanics*, Vol. 49, 2017, pp. 387–417.

[160] Towne, A., Schmidt, O. T., and Colonius, T., "Spectral proper orthogonal decomposition and its relationship to dynamic mode decomposition and resolvent analysis," *Journal of Fluid Mechanics*, Vol. 847, 2018, pp. 821–867.

[161] Chu, B.-T., "On the energy transfer to small disturbances in fluid flow (Part I)," *Acta Mechanica*, Vol. 1, No. 3, 1965, pp. 215–234.

[162] Hill, M., and Louis, M., "Rotating hub drag prediction methodology," *American Helicopter Society Specialist's Conference on Future Vertical Lift Aircraft Design, San Francisco*, 2012.

[163] Potsdam, M., Datta, A., and Jayaraman, B., "Computational investigation and fundamental understanding of a slowed UH-60A rotor at high advance ratios," *Journal of the American Helicopter Society*, Vol. 61, No. 2, 2016, pp. 1–17.

Vita

Tristan Wall was born in February of 1996 in Knoxville, Tennessee to parents David Wall and Joy Sager. He was born and was raised in Lenoir City, Tennessee until graduating high school in 2014. He then moved to Cookeville, Tennessee where he attended Tennessee Technological University. After majoring in Mechanical engineering and minoring in mathematics, Tristan graduated in cursu honorum in 2018. He continued his education at the University of Tennessee in Knoxville, graduating with a Master's of Science degree in December, 2020 under advisor Dr. James Coder. Outside of academia Tristan pursues weightlifting, sailing, and competitive fencing.